ABSTRACT

Title of Thesis: EFFECT OF SLOPED TERRAIN ON IN-GROUND-EFFECT HOVER PERFORMANCE FOR AN ISOLATED ROTOR

Jack Gregory Prewitt
Master of Science, 2023

Thesis Directed by: Dr. John Tritschler
Department of Aerospace Engineering

The present work conducted performance testing using a laboratory-scale isolated rotor operating over a ground plane mounted to a six degree-of-freedom motion platform to simulate in-ground-effect operations over sloped terrain. The rotor utilized a pair of 1:13.24 scale OH-58C blades, and performance measurements were collected using a six-axis load cell to which the rotor was mounted. Seven ground plane angles ranging from 0–18 deg, five collective blade pitches ranging from 0–8 deg, and 15 hub heights ranging from a nondimensional hub height, z/R, of 0.6 to 2.0 were tested. Additionally, the rotor was operated out-of-ground-effect for collective blade pitches ranging from 0–12 deg in increments of 1 deg in order to compare in-ground-effect and out-of-ground-effect hover performance. In-ground-effect hover over sloped terrain was found to have over a 7% reduction in performance as compared to hover over level terrain at low hub heights and large ground plane angles. In-ground-effect hover over sloped terrain was also found to require 2% more power than hover out-of-ground-effect at high hub heights and large ground plane angles. Finally, a semi-empirical model for hover performance

over sloped terrain was developed on the basis of the classic Cheeseman and Bennett ground effect model for level terrain. The coefficients obtained from this model were found to change in a consistent manner as both ground plane angle and blade loading coefficient changed, which suggests that the model could be used for future performance predictions for hover over sloped terrain.

Effect of Sloped Terrain on In-Ground Effect Hover Performance for an Isolated Rotor

by

Jack Gregory Prewitt

Thesis submitted to the Faculty of the Graduate School of the
University of Maryland, College Park in partial fulfillment
of the requirements for the degree of
Master of Science
2023

Advisory Committee:
Dr. John Tritschler, Chair/Advisor
Associate Professor Joseph Milluzzo, Advisor
Associate Professor Anubhav Datta
Assistant Professor Umberto Saetti

To my parents.

Acknowledgments

Countless pieces came together to make this thesis happen. First and foremost, I'd like to thank Dr. John Tritschler for giving me the opportunity to work under him for this unique research project. I first met Dr. Tritschler at the Southern Maryland Higher Education Center as an undergraduate student in his ENME-361 Vibrations I and ENAE-471 Aircraft Flight Testing courses. After I was accepted into the Aerospace Engineering M.S. program, we discussed the possibility of working together on the hover over slopes project. At the time I knew little about the world of research, but I found myself agreeing because of my prior rotorcraft experience at NAVAIR and because the idea of conducting and analyzing lab experiments sounded interesting and exciting. Dr. Tritschler has been instrumental in my aerospace education, and has helped me balance my NAVAIR flight test engineer job with this degree program. I'm sincerely grateful for his invaluable support. Dr. Joseph Milluzzo has also given me tremendous support in his role as a second advisor, and I am thankful for his help in the rotor lab, for reading over my drafts, for attending countless meeting with Dr. Tritschler and I, and for helping me overcome some of the major technical hurdles found in this research.

I would like to thank Associate Professor Anubhav Datta and Assistant Professor Umberto Saetti for taking the time out of their busy schedules to sit as members of my committee. I took ENAE-633/636 Helicopter Dynamics I/II with Dr. Datta and ENAE-635 Helicopter Stability and Control with Dr. Saetti; thank you for creating an enjoyable yet challenging class atmosphere, as they forced me into becoming a better engineer, critical thinker, and problem solver.

Thank you to Dan Robertson and Steve Galindo from the United States Naval Academy who helped in setting up the rotor lab and troubleshooting technical issues with me. I always looked forward to driving up to the Yard to work with you two and listening to the different projects that the Midshipmen were working on. Thank you also to Midshipmen Dylan Black and Cole Shenk, who helped in collecting large amounts of data for me when I couldn't make it up to the Yard and provided that extra support when it came to classes and conference papers.

I would like to thank my bosses Stephen Bruso and Liam Cosgrove from NAVAIR for not firing me for the amount of leave that I burnt up to complete this program. They granted me extensive amounts of time to conduct research at the Naval Academy, attend weekly meetings with Dr. Tritschler and Dr. Milluzzo, drive up to University of Maryland for classes, and travel for conferences. I am very grateful to both of you for allowing me to pursue such a time intensive goal.

I would like to thank the contract monitor Dr. David Gonzalez from the Office of for Naval Research Naval Air Warfare and Weapons Development (Code 35), who supported this work as part of the Sea-Based Aviation National Naval Responsibility.

Finally, thank you to my parents and my girlfriend Charlotte for all of their love and support, whether by letting me spend the night for quicker drives to campus, listening to me vent about struggles with research or classes, or just helping me take my mind off the math and going to do something fun. There were times where I thought that this thesis would not be possible due to seemingly insurmountable funding, time, and logistical concerns, and you all gave me the guidance and support I needed to push through. I love you.

Table of Contents

List of Tables

List of Figures

Nomenclature

Symbols

A	Rotor Disk Area (ft^2), $A = \pi R^2$
A_blades	Rotor Blades Area (ft^2), $A_\text{blades} = N_\text{b} c R$
A_disk	Rotor Disk Area (ft^2), $A_\text{disk} = \pi R^2$
c	Blade Chord (ft)
C_{d_0}	Blade Profile Drag Coefficient
C_{l_α}	Section Lift-Curve Slope
C_P	Rotor Power Coefficient, $C_P = P/\rho A(\Omega R)^3$
C_{P_i}	Rotor Induced Power Coefficient
C_{P_0}	Rotor Profile Power Coefficient
C_P/σ	Blade Power Coefficient
C_Q	Rotor Torque Coefficient, $C_Q = Q/\rho AR(\Omega R)^2$
C_T	Rotor Thrust Coefficient, $C_T = T/\rho A(\Omega R)^2$
C_T/σ	Blade Loading Coefficient
F_X	X-Axis Hub Force (lbf)
F_Y	Y-Axis Hub Force (lbf)
F_Z	Z-Axis Hub Force (lbf)
h_w	Wall Height
k_G	Ground Effect Factor
M_tip	Tip Mach Number
M_X	X-Axis Hub Moment (ft-lbf)
M_Y	Y-Axis Hub Moment (ft-lbf)
M_Z	Z-Axis Hub Moment (ft-lbf)
$\dot{m}$	Mass Flow Rate (slugs-s^{-1}), $\dot{m} = \rho A v_i$
N_b	Number of Blades
P	Rotor Power Required (ft-lbf-s^{-1})
P_IGE	Rotor Power Required In Ground Effect (ft-lbf-s^{-1})
P_∞	Rotor Power Required Out of Ground Effect (ft-lbf-s^{-1})
P_ideal	Ideal Rotor Power Required (ft-lbf-s^{-1})
R	Rotor Radius (ft)
Re_tip	Tip Reynolds Number
T_OGE	Rotor Power Required Out of Ground Effect (lbf)
T	Rotor Thrust (lbf)
T_IGE	Rotor Thrust In Ground Effect (lbf)
T_∞	Rotor Thrust Out of Ground Effect (lbf)
V	Aircraft Speed (ft-s^{-1})

V_i	Weighted Aircraft Speed (ft-s^{-1}), $V_i = V\sqrt{\sigma}$
V_T	Weighted Hover Induced Velocity (ft-s^{-1}), $V_T = \sqrt{T/2\rho A}\sqrt{\sigma}$
V_{tip}	Rotor Tip Speed (ft-s^{-1})
V_∞	Magnitude of Free Stream Velocity (ft)
v_i	Rotor Induced Velocity (ft-s^{-1}), $v_i = \sqrt{T/2\rho A}$
w	Far Wake Velocity (ft-s^{-1}), $w = 2v_i$
w_{w}	Wall Width (ft)
z	Rotor Hub Height (ft)
z_{tip}	Rotor Tip Height (ft)
z/R	Nondimensional Rotor Hub Height
α	Blade Section Angle of Attack (deg)
θ	Blade Pitch Angle (deg)
θ_{g}	Ground Plane Angle (deg)
θ_0	Collective Blade Pitch Angle (deg)
κ	Induced Power Factor
λ_i	Rotor Induced Inflow Ratio, $\lambda_i = \sqrt{C_T/2}$
μ	Rotor Advance Ratio, $\mu = V_\infty \cos\alpha / V_{\text{tip}}$
ρ	Air Density (slugs-ft^{-3})
σ	Rotor Solidity, $\sigma = N_b cR/\pi R^2$
ϕ	Inflow Angle of Attack (deg), $\phi = \tan^{-1}(U_P/U_T)$
Ω	Rotor Rotational Speed (s^{-1})

Abbreviations

6-DoF	Six Degree-of-Freedom
AGL	Above Ground Level
BX8	Model BX8-AS BlueDAQ Series Data Acquisition System
ESC	Electronic Speed Control
FM	Figure of Merit
GARTEUR	Group for Aeronautical Research and Technology in Europe
HIGE	Hover In Ground Effect
HOGE	Hover Out of Ground Effect
IGE	In Ground Effect
NACA	National Advisory Committee for Aeronautics
OGE	Out of Ground Effect
OH-58C	Bell OH-58C Kiowa
PIV	Particle Image Velocimetry
TTP	Techniques, Tactics, and Procedures
USNA	United States Naval Academy
USNTPS	United States Naval Test Pilot School

Chapter 1: Introduction

1.1 Hover In Ground Effect

Rotorcraft are key assets to miltaries, medical and rescue organizations, and law enforcement, who utilize them to execute vertical takeoff, vertical landing, and hovering maneuvers which cannot be performed by traditional fixed-wing aircraft. In order to maintain a safe and stable hover during all phases of flight, aircrew must consider aircraft performance, or the power required to generate a given thrust and the power available, for all planned flight conditions. An attempt to hover in a flight condition where the rotorcraft has an insufficient power margin can result in accidents, leading to potential loss of aircraft or life. Therefore, aircrew conduct performance planning and apply power margins for all planned flight conditions to ensure safety of flight.

In general, helicopters operating in close proximity to the ground have been found to require measurably less power to hover than those hovering at larger heights above the ground [1–7]. Because of this power requirement difference, two flight regions are typically considered by aircrew when calculating rotorcraft hover performance: hover in-ground-effect (HIGE), where rotorcraft performance is influenced by the presence of the ground; and hover out-of-ground-effect (HOGE), where a rotorcraft is hovering at a relatively large distance away from the ground, free from any ground-rotor interactions. The height at which a helicopter is considered to be in ground effect varies between models and is typically expressed in terms of rotor radii; rotorcraft hovering at heights up to approximately two rotor radii above ground are considered to be in ground effect (IGE), while hover at greater heights are considered out of ground effect (OGE) [1, 6, 8–10]. Hover in ground effect is characterized by an alteration or constraint of the flow into the rotor or the development of the rotor wake [1]. When compared to HOGE operations, HIGE results in an increase in rotor efficiency, which is typically thought of as either an increase in thrust for a given power, or a decrease in power for a given thrust [1, 9]. This performance benefit is primarily induced in nature because of the reduction in induced velocity [1], which leads to lower induced power requirements and ultimately lower total power requirements.

Depending on the expected above ground level (AGL) hover height of the rotorcraft, aircrew will use either HIGE or HOGE charts for hover performance predictions [9, 11]. While charts for HIGE are based on the performance over a flat, infinite ground plane under calm conditions and no obstacles, rotorcraft operation often does not involve operation in these ideal conditions [12]. To account for these non–ideal IGE conditions, operational communities have developed tactics, techniques, and procedures (TTPs) to account for the performance effects associated with them. For example, one such TTP is the assumption that if terrain layout or wind conditions are unverifiable, HOGE charts can provide aircrew with the expected worst-case hover performance. Aircrew will also apply various self-imposed power margins to ensure that sufficient available power exists for unique situations, such as requiring the aircraft to be below a certain gross weight during shipboard landings or confined area operations. While these publications and procedures have helped increase safety, they are still often based on experiential data as opposed to detailed controlled experimental studies.

Chapter 1 is organized as follows. Section 1.2 presents a literature survey on classical

HIGE models. Section 1.3 explores the nature of ground effect in operationally relevant flight conditions. Section 1.4 focuses on hover over sloped terrain, a specific type of operation flight condition, and how recent research in this domain motivated the present investigation. Section 1.5 presents the objectives of the current work. Finally, Section 1.6 gives an overview on how the thesis is organized.

1.2 Classical Hover In-Ground-Effect Models

As stated in Section 1.1, hover in-ground-effect is characterized by an alteration of the rotor wake typically resulting from close proximity to the ground or other solid surface [1]. A physical representation of HIGE is shown by Prouty [10] in Figure 1.1, which depicts typical regions of upflow, outflow, recirculating flow, and a combined root vortex often associated with rotorcraft operating close to the ground. The upflow region labeled in the center of Figure 1.1 exists near the inboard stations of the rotor; this upflow reduces the velocity of the air induced through the rotor and therefore provides an increase in the overall rotor thrust [10].

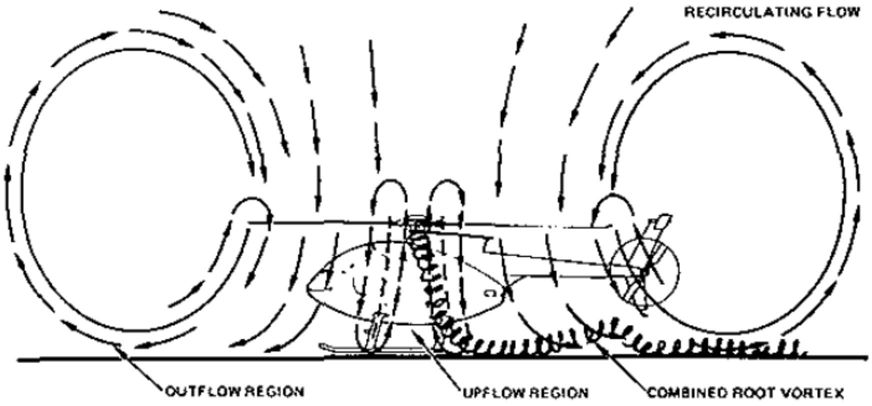

Figure 1.1: The behavior of the wake from a helicopter hovering in ground effect [10].

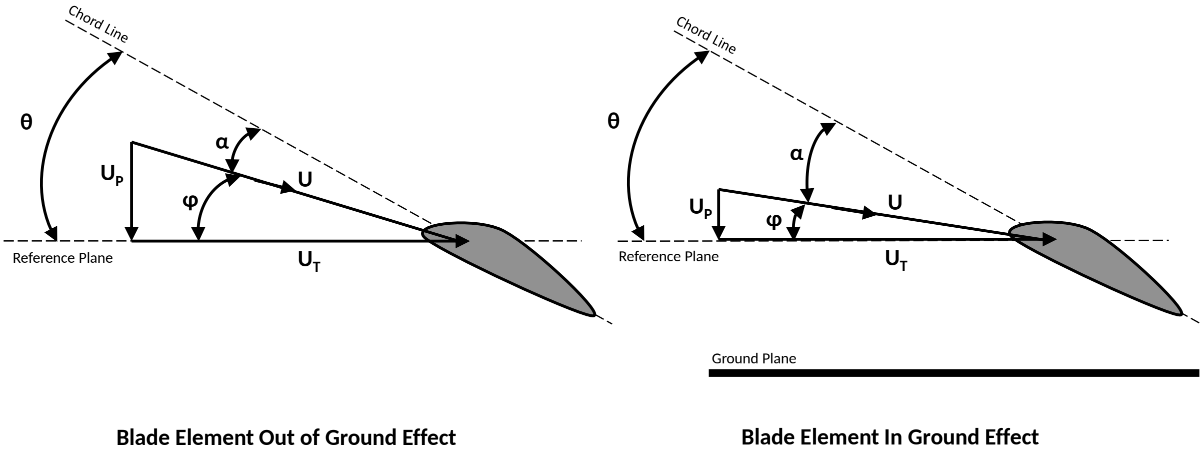

Blade Element Out of Ground Effect

Blade Element In Ground Effect

Figure 1.2: Comparison blade elements in and out of ground effect.

Figure 1.2 presents a graphical comparison between blade elements in and out of ground effect, where α is the blade angle of attack, ϕ is the inflow angle, θ is the blade pitch, U_P is the induced velocity, and U_T is the blade tangential velocity. For HIGE operations, the magnitude of the induced velocity U_P is seen to be lower than for HOGE operations, resulting in an increase in α and a decrease in ϕ for helicopters entering ground effect at a constant θ. In general, this increase in α increases the lifting capacity of each blade which manifests as an increase in thrust produced by the rotor.

The first studies on the performance of rotors hovering in ground effect were conducted by Betz [5] and Küssner [7] in 1937, who developed functions for rotor thrust as a function of the distance from the ground. Betz analytically represented HIGE conditions using the method of images where both the rotor and a mirrored image of the rotor were modeled as three-dimensional sinks from potential flow theory, and used this model to create a performance model. Knight and

Hefner [8, 13] extended Betz's approximate mathematical analysis and provided model verification using three different rotors operating in proximity to a large ground plane, and found that ground effect benefits were negligible for distances greater than two rotor radii above the surface.

Cheeseman and Bennett [2] expanded on the work by Knight and Hefner and developed a new analytical model to approximate ground effect in hovering flight over a parallel ground plane. Instead of modeling the rotor and its mirror image as sinks, Cheeseman and Bennett developed a model which replaced the rotor and its mirror image three-dimensional sources. The model predicted the ratio between IGE and OGE thrust at a constant power to be

$$\left[\frac{T_{\text{IGE}}}{T_{\text{OGE}}}\right]_{P=\text{const}} = \frac{1}{1-(R/4z)^2} \tag{1.1}$$

where T_{IGE} is the thrust produced in-ground-effect, T_{OGE} is the thrust produced out-of-ground-effect, R is the rotor radius, and z is the height of the rotor hub above the ground. It is important to note that thrust ratios must be calculated for a constant power; inaccurate thrust ratios will result if the two IGE and OGE thrusts were captured at different powers. Similarly, the ratio between IGE and OGE power, also known as a power ratio is given as the inverse of the thrust ratio such that

$$\left[\frac{P_{\text{IGE}}}{P_{\text{OGE}}}\right]_{T=\text{const}} = \frac{1-(R/4z)^2}{1} \tag{1.2}$$

where P_{IGE} is the power required in ground effect and P_{OGE} is the power required out of ground effect. In a similar manner to the thrust ratio being calculated at a constant power, the power ratio must be calculated at a constant thrust. One can convert between thrust and power ratios through a ground factor k_G, given as

$$k_G = \frac{T_{\text{OGE}}}{T_{\text{IGE}}} = \frac{P_{\text{IGE}}}{P_{\text{OGE}}} \tag{1.3}$$

allowing for data to be presented in either form [1].

Hayden [1, 3] used flight test results to develop an empirical ground effect model based on the assumption that only the induced power is influenced by the ground, such that

$$\frac{P_{\text{IGE}}}{P_{\text{OGE}}} = \frac{1}{A + B(2R/z)^2} \tag{1.4}$$

where A and B are empirical constants of A = 0.9926 and B = 0.0379, respectively. In practice, Hayden's model is found to slightly over-predict the ground effect benefit [1].

Figure 1.3 shows data collected from Lewis [14] against the analytical Cheeseman and empirical Hayden models in dashed and solid black lines, respectively . The vertical axes correspond to thrust (Figure 1.3a) and power ratio (Figure 1.3b), where thrust ratio values above 1.0 and power ratio values below 1.0 represent performance benefits as compared to HOGE. The horizontal axes represent normalized hub height z/R, which is calculated as the rotor height above the ground, z, in terms of the rotor radius, R. A monotonic reduction in thrust ratio (or increase in power ratio) is seen as z/R increases, which is characteristic behavior of an isolated rotor hovering IGE above a flat, infinite ground plane.

The effect of blade loading coefficient on ground effect benefit was also investigated in past literature [2, 4, 15]. Blade loading coefficient, C_T/σ is a form of thrust coefficient in which the reference area is the area of the rotor blades (A_{blades}) rather than the area of the rotor disk (A_{disk}),

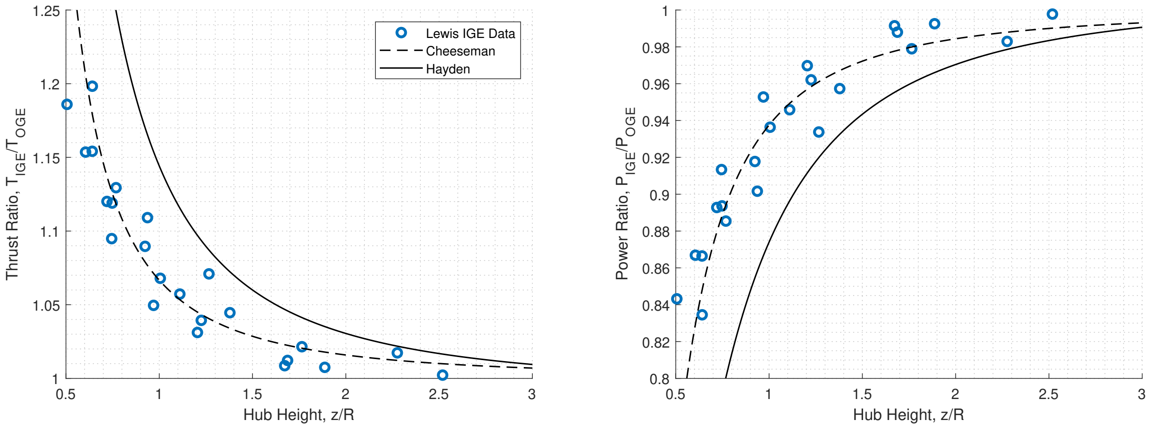

(a) Thrust Ratio. (b) Power Ratio.

Figure 1.3: Representative thrust and power ratio plots with Cheeseman and Hayden models overlaid. Data from [14].

such that

$$\frac{C_T}{\sigma} = \frac{T}{\rho A_{\text{disk}}(\Omega R)^2 \sigma} = \frac{T}{\rho A_{\text{blades}}(\Omega R)^2} \tag{1.5}$$

which allows for rotors of different sizes, planform areas, and blade number to be compared and typically ranges in value from 0 to 0.15 [1]. The effect of C_T/σ on HIGE performance was first examined by Zbrozek [4] who found that an increase in C_T/σ resulted in a reduction in ground effect benefit across all tested rotor hub heights. Cheeseman and Bennett [2] noted similar findings to Zbrozek's as well as investigated the combined effect of forward flight speed V_i/V_T (given as the ratio of aircraft speed V_i and hover induced velocity V_T) and C_T/σ on ground effect benefit. An analytical model was developed for the influence of C_T/σ on ground effect benefit, given as

$$\left[\frac{T}{T_\infty}\right]_{P=\text{const}} = \frac{1}{1 - \frac{\sigma C_{l_\alpha} \lambda_i}{4 C_T} \frac{(R/4z)^2}{1+(\mu/\lambda_i)^2}} \tag{1.6}$$

where C_{l_α} is the lift-curve slope of the rotor blade airfoil, μ is the rotor advance ratio, and λ_i is

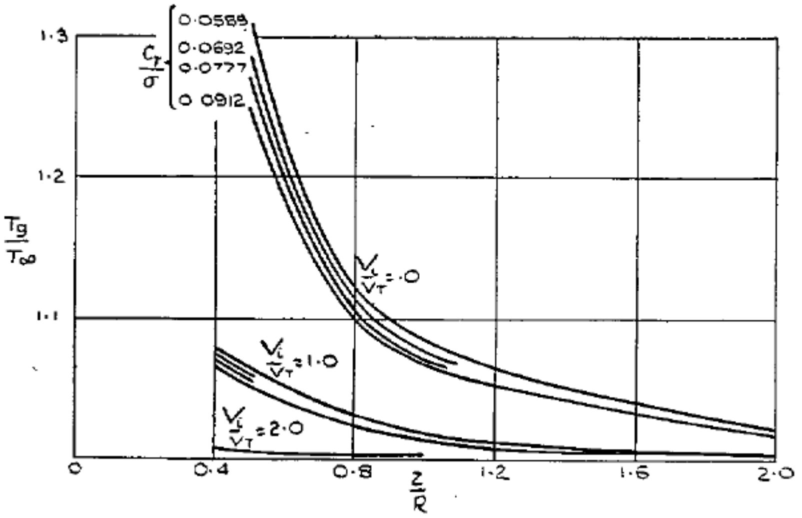

Figure 1.4: Thrust ratio as a function of z/R and C_T/σ for various speeds [2].

the rotor induced inflow ratio [1,2].

The theoretical results from Equation 1.6 are seen in Figure 1.4, which shows three sets of curves, each set corresponding to a different forward flight speed and each individual curve representing a different C_T/σ, with thrust ratio on the vertical axis and normalized hub height on the horizontal. The bottom and middle curves are associated with forward flight performance. The top set of curves, corresponding to $V_i/V_T = 0$ or hovering flight, show a reduction in thrust ratio as C_T/σ is increased for all tested hub heights. As z/R increases, the percent difference between the highest and lowest C_T/σ curves diminishes, with a 3% difference for $z/R = 0.6$ and only 1% for $z/R = 1.6$, suggesting that thrust conditions impact ground benefit as the hub height above the ground is reduced.

Lastly, Fradenburgh [6] experimentally investigated the effect that both hub height and ground plane angle had on ground effect benefit. Figure 1.5 shows thrust ratio as a function of ground plane angle at different hub heights for both a helicopter and an annular jet. The helicopter data set shows a reduction in thrust ratio as the ground angle is increased, particularly

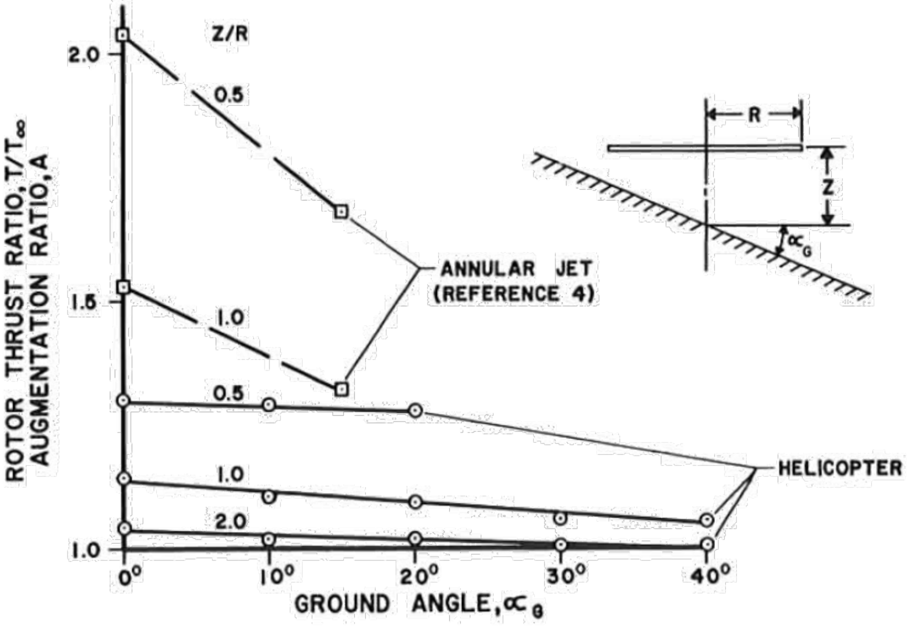

Figure 1.5: Thrust ratio as a function of ground plane angle for multiple z/R [6].

for z/R of 1.0 and 2.0. However, the thrust ratio was not seen to drop below a value of 1.0, indicating thrust generated remained above HOGE thrust values. Additionally, the effect of blade loading coefficient for hover over sloped terrain was not examined in this study, so to improve the understanding of operation above sloped terrain there is a need to better understand the effect of operational thrust on rotor performance. Fradenburgh's work marks the ”transition” between classical ground effect research and modern operationally-oriented research with his focus on the influence of environmental factors on HIGE performance, rather than the influence of rotor height or thrust on performance.

1.3 Hover in Operationally Relevant Conditions

Efforts have recently been undertaken to better understand the influence that operationally relevant conditions such as obstacles [16–22], confined areas [23], walls [24–26], and sloped ter-

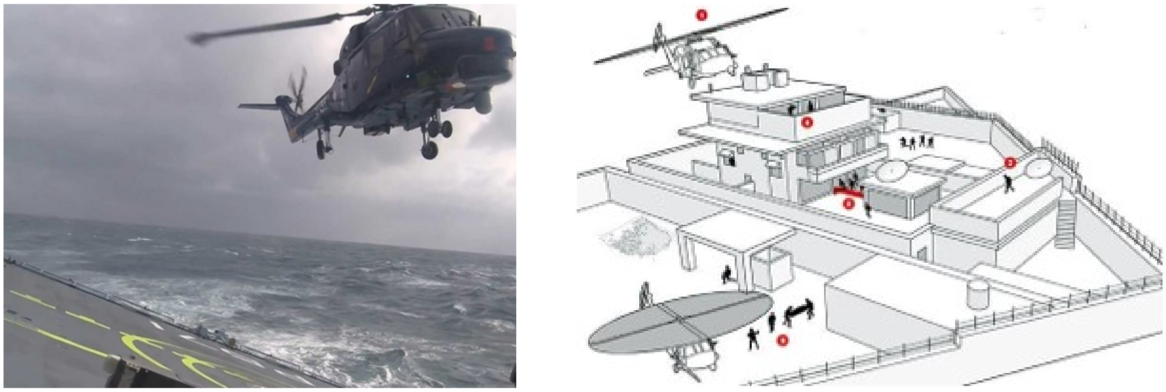

(a) Hover over a sloped ship deck [30]. (b) Hover near walls and within confined areas [31].

(c) Hover over a sloped mountainside [32].

Figure 1.6: Helicopters operating in operationally relevant conditions.

rain [6, 12, 27–29], have on helicopter hover performance. Figure 1.6 shows helicopters hovering in operational conditions such as over sloped terrain in Figures 1.6a and 1.6c or within confined areas in 1.6b. Hover in these operational conditions had been found to yield significantly different performance and flow field results than when operating over a flat infinite ground plane, and these findings will be reviewed in the present section.

1.3.1 Hover Near Walls

Konuş and Savaş [24], conducted a series of water tank experiments to collect particle image velocimetry (PIV) flow visualizations and performance measurements for a rotor operating in close proximity to walls and corners. Figure 1.7 shows the collected performance measurements for the work along with a representative image of the rotor flow field near a wall, taken using

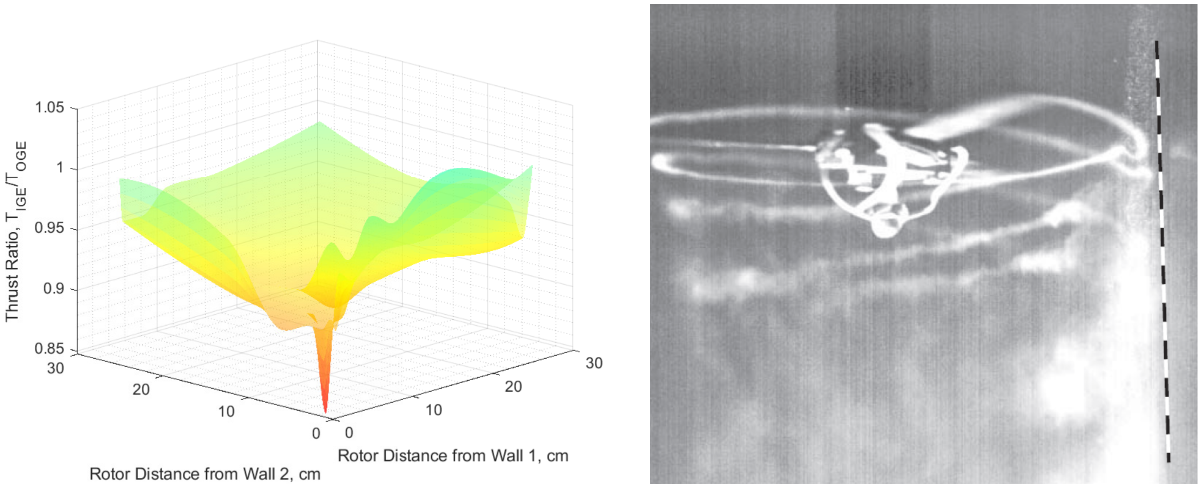

(a) Thrust ratio surface as a function of rotor-wall distance.

(b) PIV image of rotor flow. Wall denoted with dashed black-white line.

Figure 1.7: Performance and flow field results for a rotor operating near walls [24].

PIV. Figure 1.7a shows thrust ratio (post-processed using spline interpolation to smooth edges) as a function of rotor distance between two sets of walls, where a reduction in thrust ratio is seen as the rotor moves closer to one or both sets of walls, with the largest drop in performance seen when operating in a tight corner. The presence of the walls have prevented the rotor wake from fully developing as seen to the right of Figure 1.7b, and this flow constraint was speculated to lead to the drop in performance.

Garofano et al. [25] expanded on the research on hover near walls by numerically investigating wall and corner effect with tilted propellers. Figure 1.8 shows performance and flow field results for a rotor operating in wall effect for distances from 1.3–3.8 d/R (nondimensional rotor-wall distance) for propeller tilt angles of 20, 30, and 40 deg. Maximum performance penalties of 1% as compared to out-of-wall-effect conditions were seen at $d/R = 1.3$, and all rotor distances showed relative insensitivity to tilt angle.

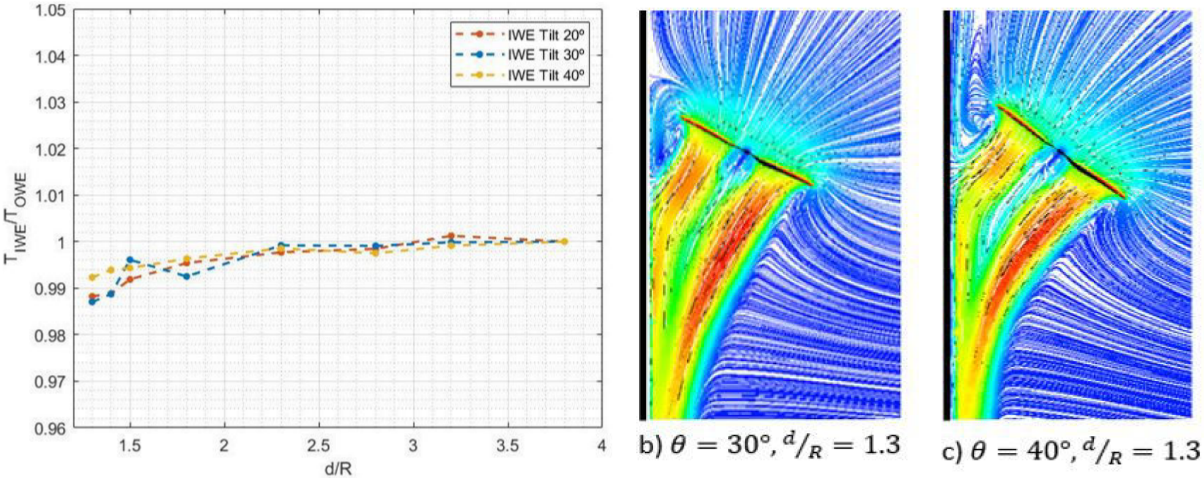

(a) In-wall-effect thrust ratio results. (b) Velocity contours for $d/R = 1.3$.

Figure 1.8: Velocity contours and performance results for tilted rotor-wall interactions [25].

1.3.2 Hover Near Obstacles

Similar to the hover near walls work, the GARTEUR action group [18–21] conducted numerical and experimental investigations on the forces experienced by obstacles when immersed in rotor wakes. For experimental work, Gibertini et al. [18, 20] utilized a motorized helicopter model which operated over a building model with pressure taps. Figure 1.9b shows the experimental setup includiong the helicopter model, camera, and building model. Figure 1.9a shows two sets of thrust ratio data; Test 1 consisted of a hub height sweep over a flat, infinite ground plane, while Test 4 consisted of a hub height sweep to the side of the obstacles. Test 4 resulted in thrust ratios less than 1.0 at approximately the same height as the obstacle. This performance penalty persisted up to a z/R of 3.0, whereupon the thrust ratio returned to a value of 1.0.

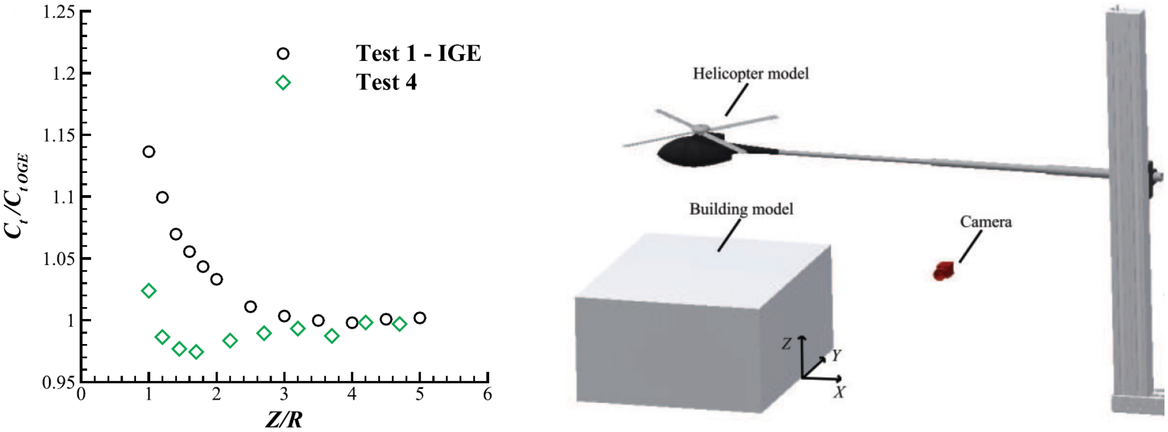

(a) Thrust ratios for Tests 1 and 4.

(b) Hover near obstacles experimental setup.

Figure 1.9: Experimental setup and thrust ratios corresponding to two tests [19].

1.3.3 Hover in Confined Areas

Finally, research on confined area operations [23, 33] was conducted to understand the effects that two or more sets of walls had on performance. Iboshi et al. [23] conducted laboratory-scale testing of an isolated rotor operating within an indoor confined area setup as seen in Figure 1.10b, which shows the rotor between a set of walls of width w_w and of height h_w. The results in Figure 1.10a show the lab results in power ratio form with six trends, each representing a different w_w for an h_w of one rotor radii. Iboshi found that as w_w was reduced to three rotor radii or lower, a spike in power ratio up to 1.10 was seen at a hub height of 1.0 z/R, corresponding to a 10% performance penalty when compared to HOGE operations (considered the worst case hover performance scenario.)

Iboshi et al. 's findings were verified by Black et al. [33], who conducted both flight testing of an OH-58C operating within a three-walled structure forming a confined space. Several wall heights, rotor speeds, and hover locations within the confined area were tested. Figure 1.11 shows the OH-58C operating in the center of the $h_\mathrm{w} = 2.04R$ confined area along with the

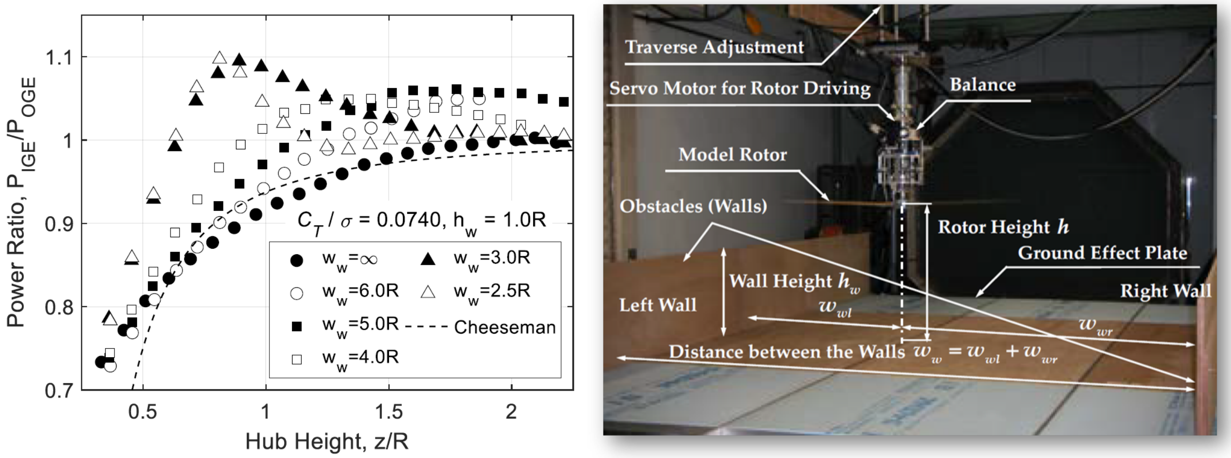

(a) Power ratio lab test results.

(b) Confined area lab setup.

Figure 1.10: Confined area laboratory setup and results [23].

corresponding power ratio results. Figure 1.11a shows results for $C_T/\sigma = 0.066$, this time with z/R on the vertical axis and power ratio on the horizontal to better represent the physical flight test setup, with the red dashed line corresponding to the wall height of the confined area. The largest power ratio value of 1.13 was seen at $z/R = 2.04$, which aligns with the top of the confined area. Similar penalties were also seen to occur near the top of the confined area, regardless of its height.

1.4 Hover over Sloped Terrain

All of the preceding research observed performance penalties for operational conditions. These operational findings motivated additional studies on hover over sloped terrain [12, 26, 27, 34, 35], another operationally relevant condition, to see if similar performance penalties would occur for certain ground angles. Hovering over sloped terrain is often seen during hover operations over moving ships or over unprepared terrain, as seen in Figure 1.6. Milluzzo et al. [27] therefore conducted performance and flow field measurements of a lab-scale rotor oper-

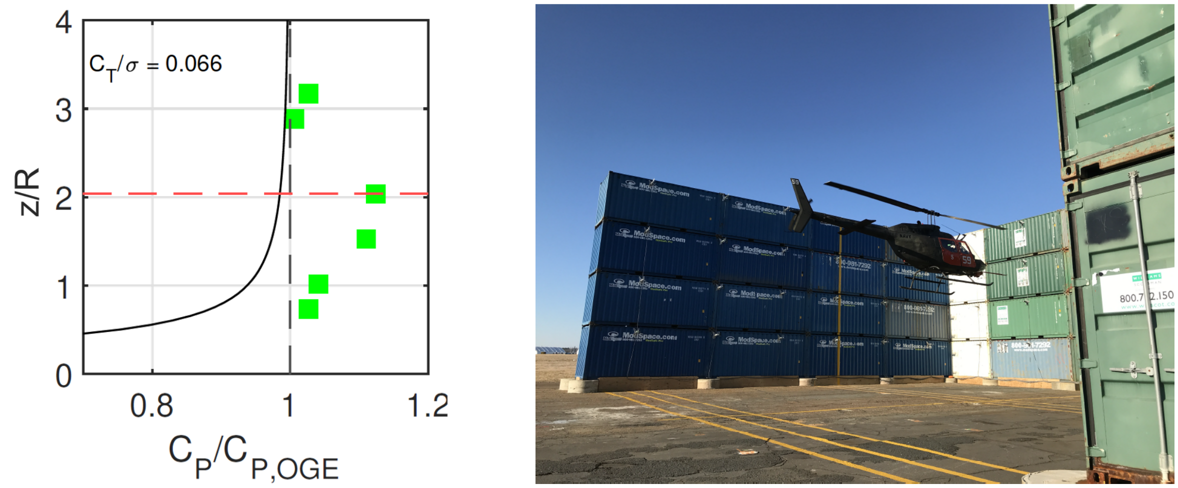

(a) Power ratio flight test results.

(b) Confined area flight test setup.

Figure 1.11: Confined area flight test setup and results [33].

ating at a height of one rotor radius over an adjustable ground plane for six ground angles ranging from 0–30 deg. Figure 1.12 shows a plot of blade power coefficient (C_P/σ) versus blade loading coefficient (C_T/σ) for various ground plane angles (θ_g) and a corresponding velocity contour for the case of $\theta_\mathrm{g} = 30$ deg and $z/R = 1.0$. Similar to the results seen by Fradenburgh [6], Milluzzo et al. observed a reduction in thrust as ground plane angle increased, while the power appeared constant across the range of tested ground angles. Rotor performance was found to be relatively insensitive to ground plane angle at lower C_T/σ, while higher C_T/σ resulted in a thrust degradation of approximately 10% between the lowest and highest ground angles tested.

Milluzzo et al. also included flow field investigations in order to provide insight into the underlying fluid mechanics. They observed formation of two wall-jet features on the uphill side, one convecting outward and one convecting inward towards the rotor, which increased in thickness with greater ground plane angles. The formation of the inward wall-jet resulted in the large recirculation regions near the hub to become tighter and more coherent near the root of each blade, and at the highest ground plane angles these rotational structure merged causing an in-

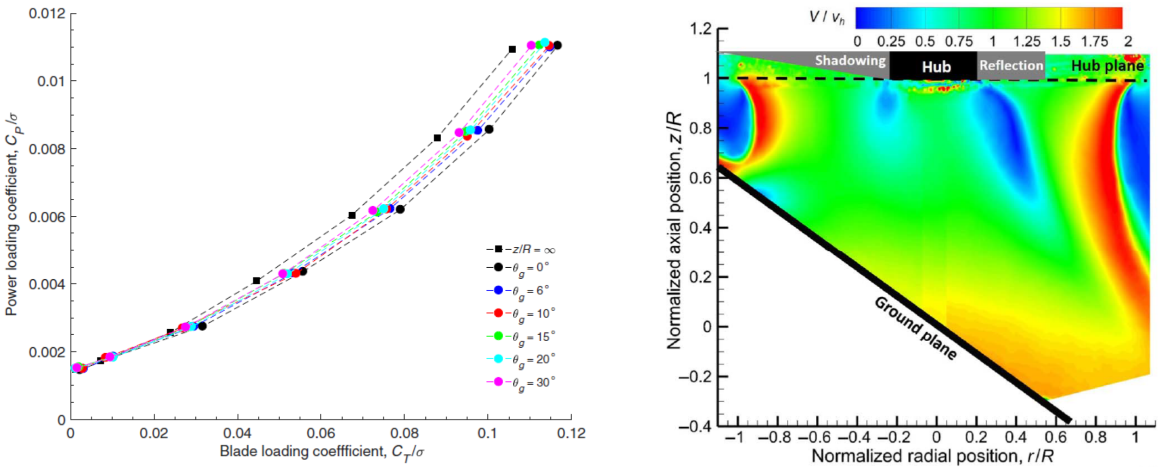

(a) Hover over slopes lab test results.

(b) Velocity contour for $\theta_{\mathrm{g}} = 30$ deg.

Figure 1.12: Hover over slopes performance results and representative velocity contour [27].

crease in inflow on the uphill side and a decrease in inflow near the inboard portion of the blade. However, these results were for a single hub height and single slice through the flow (i.e., aligned with the direction of the incline).

Tritschler et al. [12, 29] followed by comparing hover over sloped terrain performance data from both laboratory and flight testing. They found that non-intuitive and operationally significant performance effects occurred while hovering over angled ground planes for flight test. Figures 1.13a and 1.13b show a comparison of results for both flight and lab test in the form of power ratio surfaces as a function of hub height and blade loading coefficient. Each surface represents a different ground plane angle, with red corresponding to 0 deg, green to 6 deg, and blue to 12 deg. The laboratory results again shows good agreement with Fradenburgh, as power ratio increases as ground plane angle increases. However, the flight test results show that power requirements exceed OGE power requirements for cases of low blade loading coefficient and z/R of 1.5, which was not seen in prior sloped terrain work [6, 27]. Notice that this region of performance penalty is for hub heights above 1.0 and C_T/σ below 0.09, with the largest penalties

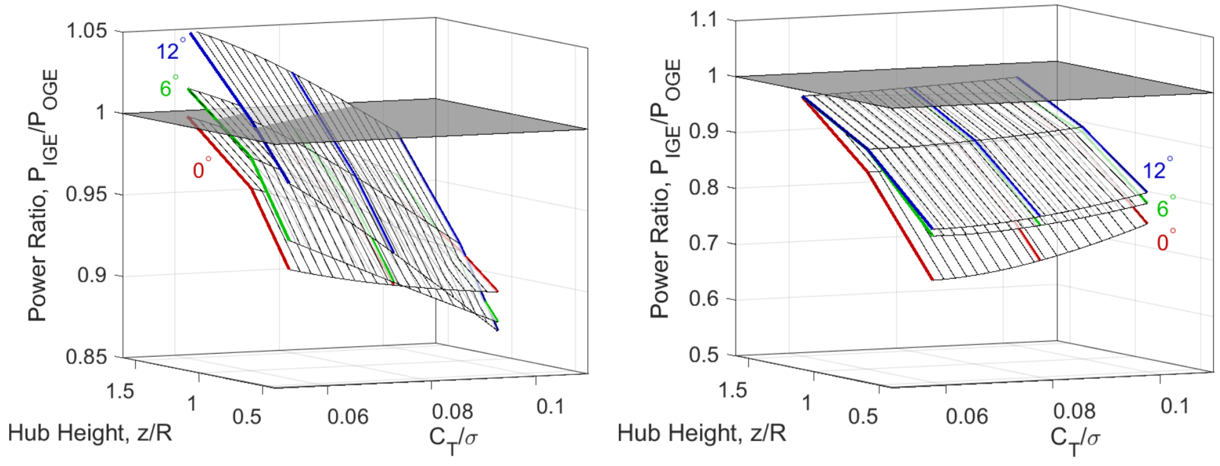

(a) Hover over sloped terrain flight test results.

(b) Hover over sloped terrain lab test results.

Figure 1.13: Hover over sloped terrain lab and flight test results [12].

at the highest z/R and lowest C_T/σ values.

One key limitation of the study by Tritschler et al. [12] was that is was conducted for only three different hub heights. In contrast, the work by Iboshi [23] on performance within confined areas was done for 22 different hub heights, thus providing a finer resolution of data. This in-depth data collection allowed for the visualization of non-monotonic trends for the $w_\mathrm{w} = 2.5R$ and $w_\mathrm{w} = 3.0R$ cases; if instead Iboshi used the same hub height resolution as Tritschler et al., there would have been the possibility of missing the non-monotonic spike seen at a z/R of $\sim$0.8. A comparison between a two-dimensional representation of hover over sloped terrain data [12] and hover in confined areas [23] data can be seen in Figure 1.14 to see the difference in hub height resolution between the two. If three hub heights are arbitrarily picked for the $w_\mathrm{w} = 2.5R$ case as seen in Figure 1.14b, a monotonic trend is created between the three points, rather than the non-monotonic trend seen with the finer resolution. This suggests that similar non-monotonic trends may be seen when hovering over sloped terrain, but were missed because of the low hub height resolution in Tritschler et al.

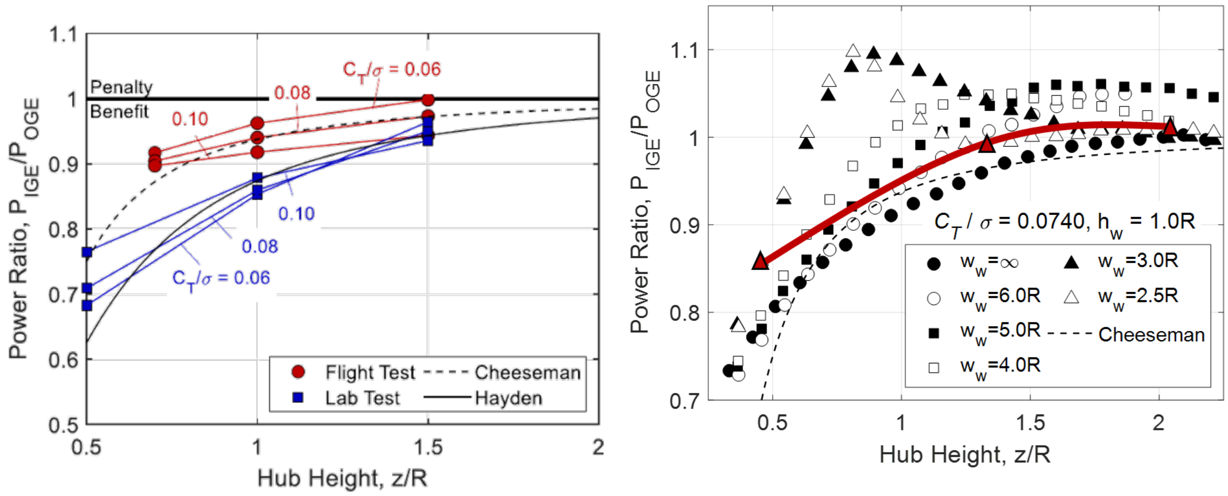

(a) Power ratio trends from [12]

(b) Power ratio trends from [23] with coarser sampling.

Figure 1.14: Comparison of data collection resolutions between [12] and [23].

1.5 Objectives of the Current Work

The goal of the present thesis is to develop a more complete understanding of HIGE over sloped terrain through a wider range of hub heights, blade loading coefficients, and ground plane angles, as well as a finer resolution of hub height data. The present work was conducted using isolated rotor operating over a ground plane mounted to a six degree-of-freedom (6-DoF) motion platform for fifteen different hub heights, five different blade loading coefficients, and seven different ground plane angles. The specific objectives of the current work were as follows:

1. To analyze in-ground-effect hover performance exhibited by an isolated rotor for both sloped and level terrain at a finer hub height resolution and wider range of test points than found in previous efforts in order to capture possible non-monotonic effects or performance penalties.

2. To understand the differences in performance seen between the laboratory and flight test

data collected by Tritschler et al. and Milluzzo et al. [12, 27], and to see if similar performance degradations above hover out-of-ground-effect are observed in laboratory testing.

3. To develop a semi-empirical model based on collected data for hover over sloped terrain performance predictions.

1.6 Organization of the Thesis

The present chapter has discussed the problem of hover in ground effect, with particular focus on the effects that blade loading coefficient and ground plane angle have on performance. A survey of theoretical hover performance models, HIGE performance models, effect of blade loading on HIGE performance, and effect of ground plane angle on HIGE performance has been conducted. The findings of previous research on hover over sloped terrain has been discussed. The recent findings by Tritschler et al. , and Milluzzo et al. , and Iboshi et al. [12,23,27] on HIGE performance over operationally relevant conditions have particularly motivated the present study on how the combination of ground plane angle and blade loading coefficient affect rotor hover performance.

Chapter 2 presents a comprehensive description of the methods used to perform the experiment, including the equipment, the laboratory setup, the experimental techniques that were used to characterize rotor hover performance over sloped terrain, and the uncertainties in the data.

Chapter 3 presents performance results for level and sloped terrain cases, which are shown in the form of three-dimensional power ratio plots, along with a discussion of the sloped terrain results compared to level terrain and HOGE performance. The development of a preliminary sloped terrain model is also discussed, as well as the challenges faced with the research effort.

Chapter 4 presents the final conclusions as well as a recommendation for future work.

Chapter 2: Methodology

2.1 Introduction

In order to better understand the effect of sloped terrain on hover in-ground-effect performance, an experiment was conduced at the United States Naval Academy (USNA) involving an isolated rotor operating over a six-axis ground plane for a range of collective blade pitch angles (θ_0), ground plane angles (θ_g), and rotor hub heights (z). Rotor thrust produced and torque required data were collected for each combination of θ_0, θ_g, and z. The rotor blades used in the experiment were a 1:13.24 scale of a OH-58C rotor blade to align with future OH-58C flight testing plans and were designed with the same solidity, airfoil section, and planform geometry. This chapter will begin by providing a description of the equipment, techniques, and processes used during the test, followed by a description of the experimental procedure and the uncertainties in the collected measurements.

2.2 Rotor System

A rotor system with a two-bladed teetering hub configuration was used in the present study, as seen mounted on a horizontal beam above an angled ground plane in Figure 2.1. The two aluminum rotor blades were designed with rectangular, untwisted geometry of radius 16.0 inches

Table 2.1: Rotor system operating parameters.

Parameter	Value
Number of Blades, N_b	2
Blade Radius, R	406 mm (16.0 in)
Mean Chord, c	24.9 mm (.980 in)
Thickness to Chord Ratio, t/c	12%
Rotational Frequency, Ω	50.0 Hz (3000 RPM)
Tip Speed, V_tip	128 ms^{-1} (419 ft s^{-1})
Tip Mach Number, M_tip	0.372
Tip Reynolds Number, Re_tip	218,000

(406 mm) and chord of 0.980 inches (24.9 mm), with NACA 0012 airfoil sections from root to tip. The rotor was powered by a KDE Direct KDE8218XF-120 brushless electric motor which had a motor velocity constant of 120 RPM/V, a maximum continuous current of 110 A, and maximum continuous power of 5,695 W. The rotor blade and operational characteristics are shown in Table 2.1. The motor was operated at a rotational frequency of 50.0 Hz (3,000 RPM), corresponding to a blade tip speed (V_tip) of 419 ft/s (128 m/s), a tip Reynolds number (Re_tip) of 218,000, and a tip Mach number (M_tip) of 0.372. Rotor speed was controlled through RCbenchmark which allowed the user to manually control the output value of the electronic speed controller (ESC) connected to the motor.

The various components of the teetering rotor hub are shown an the exploded view diagram in Figure 2.2. The blade pitch was changed through manual adjustment of the collective swashplate, which could be set to a desired blade pitch by spacers whose thickness corresponded to specific blade pitch angles. The spacers, shown in Figure 2.3, were accurate within 0.1 deg of the desired blade pitch angle and would be placed between the collective swashplate and the rotor hub to set the distance required to achieve the desired blade pitch.

The rotor hub, motor, and load cell were mounted to the bottom of a large horizontal steel

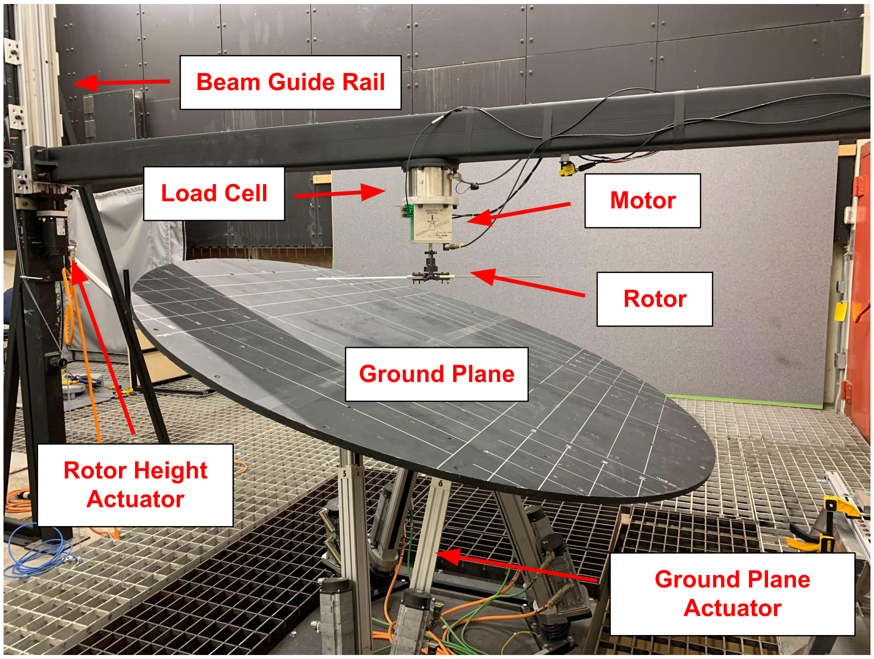

Figure 2.1: Rotor system with the ground plane below set at an angle.

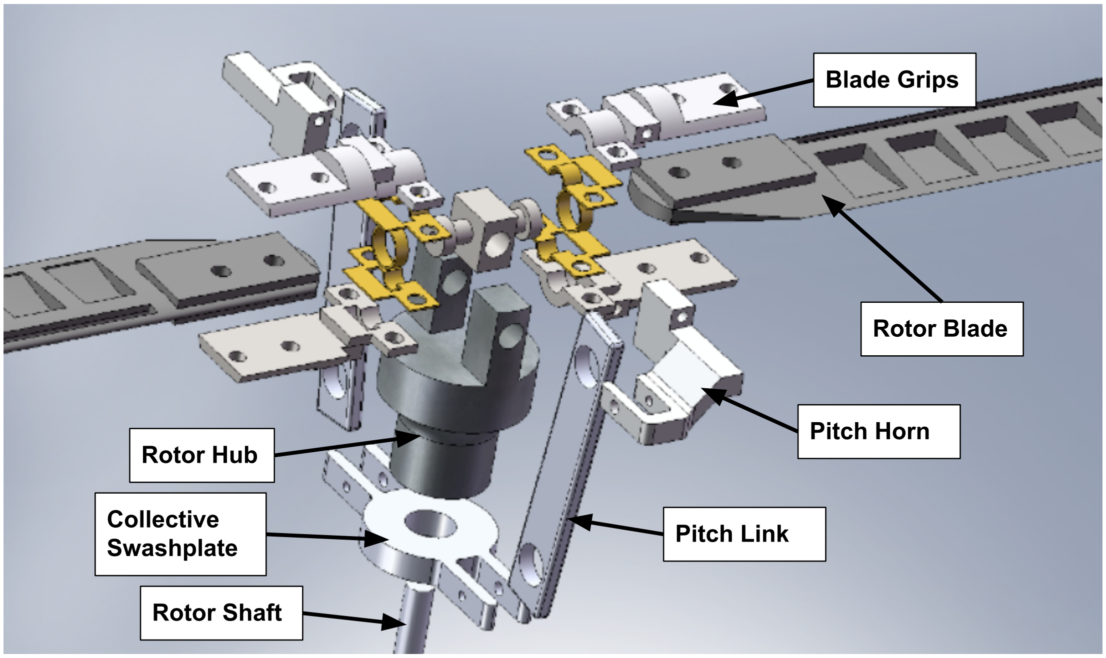

Figure 2.2: Exploded view diagram of the rotor hub used during the experiment.

Figure 2.3: Measurement spacers used when adjusting blade pitch.

beam of length 141.75 in and of square cross section 6 in by 6 in as shown in Figure 2.1. Servomotors mounted to the ends of the horizontal beam were used to adjust the height of the rotor with respect to the ground plane, which allowed for a maximum vertical displacement of 37.0 in with a precision of 0.01 in. Additionally, the rotor was 81 in (approximately 5 rotor radii) from the closest wall. Iboshi et al.'s [23] work on rotors in confined areas saw performance penalties up to a rotor-wall distance of $2.5R$; the rotor-wall distance in the present work was $5R$, so the influence of the wall on the current measurements was assumed to be negligible. Finally, prior to the start of testing, the rotor was balanced to limit the system vibrations to less than 0.1 inches-per-second (ips).

2.3 Ground Plane

The ground plane shown in Figure 2.1 was used to simulate IGE conditions for the isolated rotor. The ground plane was designed with a smooth finish and radius of 3.28 ft (2.45 rotor radii) for an area of 33.8 ft^2, and was mounted on a Symétrie Notus Hexapod positioning system. The Hexapod was powered by six actuators allowing for six degree-of-freedom (6-DoF) movement, and had a linear Z-axis travel range of ±200 mm and angular X and Y-axis travel range of ±25 deg. The ground plane and Hexapod were set to a fixed vertical height relative to the rotor's rotational axis during HIGE testing, as shown in Figure 2.1, while the rotor system servomotors were used to adjust the height of the horizontal beam which supported the rotor.

The initial starting hub height of the rotor z was set based on the minimum safe tip clearance (z_{tip}) for the largest selected ground plane angle examined. Figure 2.4 shows a rotor operating over an angled ground plane where the mean rotor height can be defined as

$$z = z_{\text{tip}} + R \tan \theta_g \tag{2.1}$$

where z is the mean rotor height and θ_{g} is the ground plane angle.

For a minimum safe tip clearance of 4 in (0.25 z/R) and a maximum θ_{g} of 18 deg, the hub height z was determined to be 9.20 in, corresponding to a nondimensional hub height (z/R) of 0.575. For the current measurements the lowest hub height z was rounded up to be 0.6R or 9.60 in because of the OH-58C's minimum possible hub height of 0.6R. This hub height z was used for all HIGE testing for all ground plane angles and collective blade pitches. A maximum hub height of two rotor radii was selected because the influence with the ground would be expected to be minimum [1]. However, to ensure HOGE conditions, additional measurements were taken with the ground plane removed. The HOGE test points consisted of removing the ground plane, lowering the motion platform, and raising the rotor for a hub height z of 54.7 in or 3.42R. With the The Hexapod mounting plate was a 1.875 ft × 1.875 ft square surface, corresponding to a surface area of 3.516 ft^2.

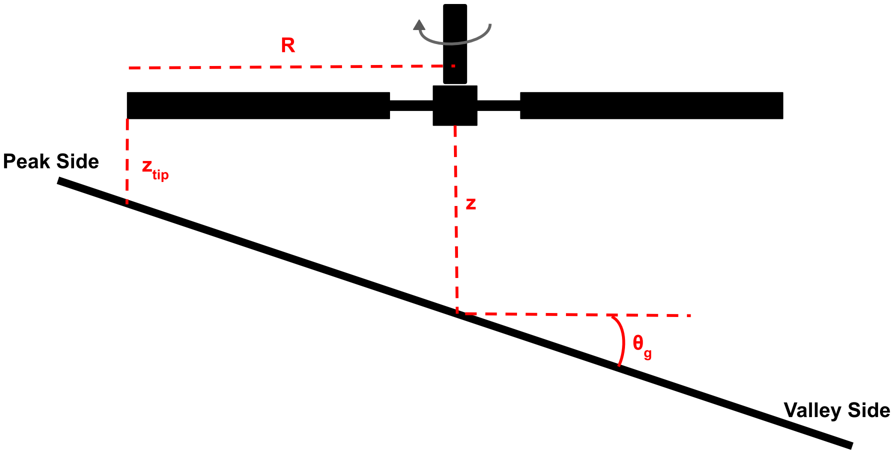

Figure 2.4: Ground plane clearance calculations.

2.4 Performance Measurements

Rotor hub loads were captured through the use of an Interface 6A154C 6-axis load cell. Three forces F_X, F_Y, and F_Z and three moments M_X, M_Y, and M_Z were collected, with F_Z corresponding to the rotor thrust and M_Z to torque about the rotor shaft; F_X, F_Y, M_X, and M_Y, were not utilized for the present work.

The load cell collected hub loads at a rate of 1,000 Hz. Connection between the load cell and a data collection computer were done through a BlueDAQ Series Data Acquisition System Model BX8-AS 8-channel amplifier (BX8) which converted the analog output voltage from the load cell into a digital signal. The BX8 was sensitive to output voltage changes from the load cell, allowing it to read small output signals with limited amplification or signal conditioning and reduced the potential of electrical interference and noise. The load cell was calibrated by taring all six axes with the rotor in a non-rotating state, and was performed after each hub height sweep.

Data recording was manually activated upon the rotor reaching steady-state at the desired test point. For the present work, the rotor was considered to be steady-state ten seconds after rotor and ground plane position adjustments. The BlueDAQ software was programmed to collect 30,000 data points for each test point, which for a data acquisition rate of 1,000 Hz corresponded to a total collection time of 30 seconds per point. For HOGE operations, BlueDAQ was programmed to collect 90,000 data points to examine the sensitivity of the F_z and M_z averages to sample size.

2.5 Overview of Experiment

As previously discussed in Chapter 1, the goal of the current work was to improve the understanding of the effect sloped terrain has on HIGE performance. The present investigation sought to collect performance data at the various collective blade pitch angles (θ_0), ground plane angles (θ_g), and rotor hub heights (z) shown in Table 2.2. The selected z/R and θ_0 conditions corresponded to hub heights and blade loading coefficients typically seen by the OH-58C which range from $0.6 \leq z/R \leq 2.0$ and $0.045 \leq C_T/\sigma \leq 0.11$.

Figure 2.5 illustrates a typical data collection timeline that was used during testing for each θ_0 condition. Prior to the start of each sweep, the blades were manually adjusted to the desired collective pitch. Testing began at a ground plane angle of 0 deg and a rotor non-dimensional hub height z/R of 0.6. Each test point was run for 30 seconds after steady-state conditions were achieved; once the test point was complete, the hub height was increased by $0.1R$ and the process was repeated until reaching the maximum hub height of $2.0R$. After completion of the final test point in the upsweep, the rotor was lowered to examine any hysteresis in the measurements. Hysteresis data were collected by lowering the rotor from the maximum to minimum hub height

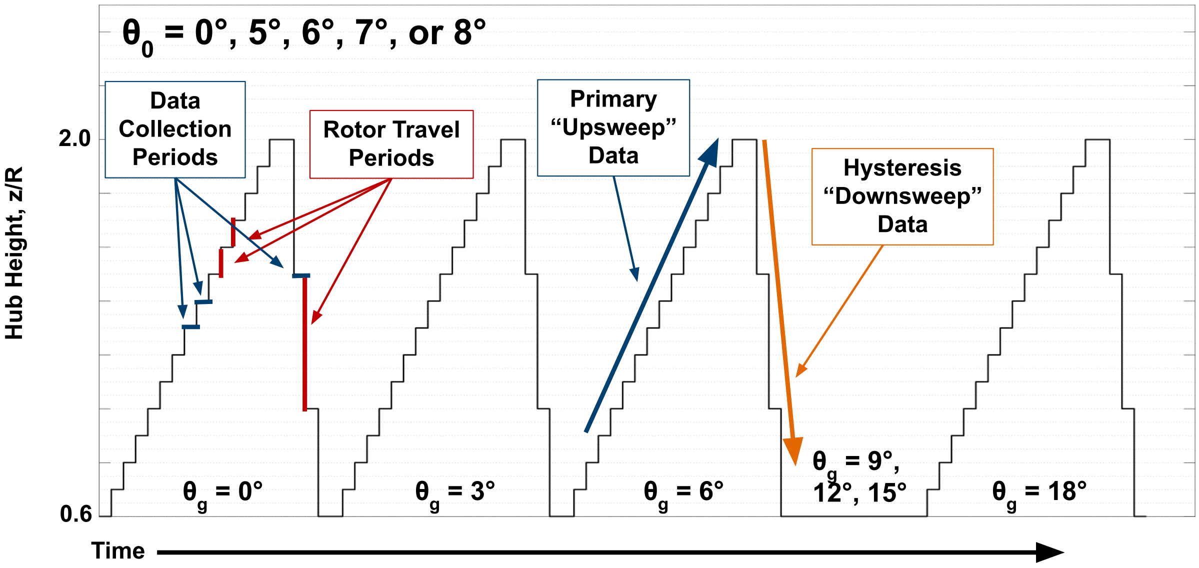

Figure 2.5: Standardized data collection method for each collective blade pitch.

Table 2.2: Summary of test conditions.

	Interval	Units
z/R	$0.6:0.1:2.0$, OGE	
θ_g	$0:3:18$	deg
θ_0	$0, 6, 7, 8, 10$	deg

in -0.5 z/R increments, whereupon the rotor was stopped and the load cell was tared. Once the primary and hysteresis data were collected, the ground plane angle was increased to the next desired testing condition and the data collection was repeated. Upon collecting data for all ground plane angles for a single blade pitch, the blades would be manually adjusted to the next pitch setting and the cycle was repeated until all the test points were completed. Out-of-ground-effect data were collected at the end of testing by collecting performance measurements for each collective blade pitch in 1 deg increments from 0–12 deg.

2.6 Uncertainties in the Performance Measurements

Sources of uncertainty during testing included load cell measurements, motor controls, rotor position equipment, and measured air properties. The load cell was rated for hysteresis, non-linearity, creep, and non-repeatability error. Hysteresis, non-linearity, and creep were rated to be $\pm 0.1\%$ of the full scale output load cell axis value, corresponding to an accuracy of ± 0.1124 lbf for thrust (4.825×10^{-5} for C_T) and ± 0.01475 ft-lbf for torque (4.749×10^{-6} for C_P). Additionally, the accuracy of non-repeatability was rated as $\pm 0.5\%$ of the rated output of the load cell axis value, corresponding to an accuracy of ± 0.5620 lbf for thrust (2.413×10^{-4} for C_T) and ± 0.07375 ft-lbf for torque (2.375×10^{-5} for C_P).

Uncertainty also existed in the control of the motor speed, as the operator had to manually adjust the ESC value in order to keep the motor at a constant 3000 RPM. The motor angular velocity was maintained at 3000 ± 10 RPM. When combined with the load cell uncertainty, the final measurement uncertainties were $C_T = \pm 4.858 \times 10^{-5}$ and $C_P = \pm 4.781e^{-6}$ for hysteresis, non-linearity, and creep, or $C_T = \pm 2.429 \times 10^{-4}$ and $C_P = \pm 2.391 \times 10^{-5}$ for non-repeatability.

Temperature, pressure, and humidity were monitored through a Davis 6152 Weather Station. The weather station was accurate to ± 0.03 inHg for barometric pressure, ± 0.5°F for temperature, and $\pm 2\%$ for humidity, leading to an overall air density uncertainty of $\pm 5 \times 10^{-6}$ slugs-ft^{-3}. The ground plane angle was controlled by a Symetrie 6-axis Notus Hexapod, which had an accuracy in translation of 0.1 mm and 0.02 mm for repeatability and resolution respectively, as well as in rotation of 0.01 deg and 0.002 deg for repeatability and resolution, respectively.

The effect that hysteresis and non-repeatability had on C_T and C_P values is shown in Figure 2.6, which shows a typical power polar plot with uncertainty bands based on the uncertainty

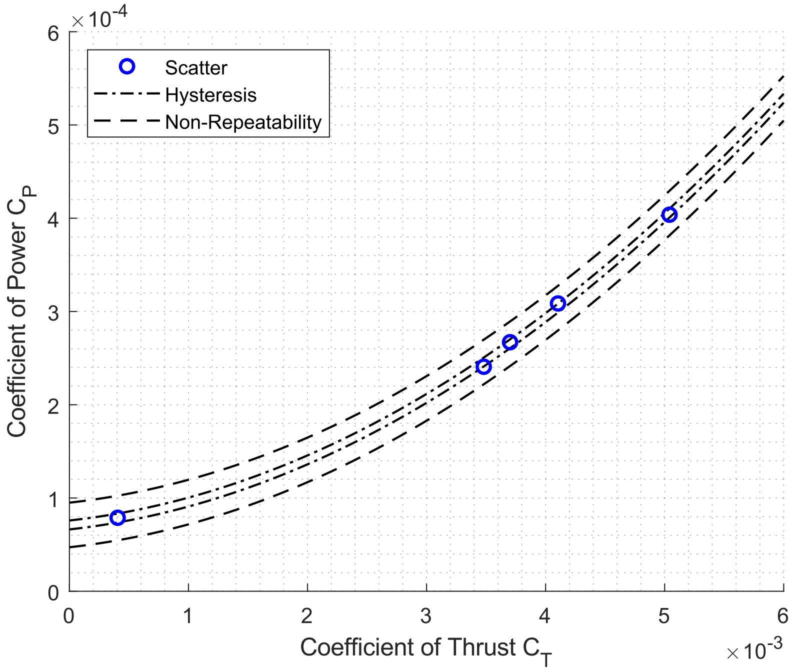

Figure 2.6: Uncertainty bands for a representative power polar plot.

values.

2.7 Summary

The present chapter has discussed the experimental setup, the measurement techniques, and the data formulation techniques to collect and present measurement data for an isolated rotor operating IGE over sloped terrain. Seven different ground plane angles and five different blade pitches were examined for fifteen different hub heights in order to examine the performance changes ground plane angle had on isolated rotor HIGE performance. The estimation of various sources of measurement uncertainties was also discussed.

Chapter 3: Results and Discussion

3.1 Introduction

As discussed in Chapter 1, blade loading coefficient, ground plane angle, and rotor hub height have all been observed to influence the ground effect benefit experienced by a rotor. The present work has tested the combination of fifteen different hub heights, five different blade pitches, and seven different ground plane angles in order to improve the understanding of the effect sloped terrain has on HIGE performance. Rotor thrust and torque data were collected for each test point; power polars and power ratios, i.e., IGE power divided by OGE power, were generated which were used to investigate HIGE performance for the various θ_g. Discussion of the combined effects that θ_g and θ_0 have on HIGE performance compared to level terrain is also presented. A semi-empirical model which includes the effects of both θ_g and θ_0 will also be presented, and its potential for performance predictions discussed. Additionally, the challenges faced during data collection and data processing will be presented.

Chapter 3 is organized as follows. Section 3.2 explains the process used to convert the raw data into power polars and power ratios. Section 3.3 and 3.4 examine the effects that θ_g and θ_0 have on rotor hover performance. Section 3.5 presents the development of a semi-empirical model used for hover over sloped terrain performance predictions. Finally, Section 3.6 discusses the challenges encountered with the present work.

3.2 Data Processing and Plot Generation

3.2.1 Data Processing

As stated in Chapter 2, rotor hub load data were collected using a six-axis load cell, which measured longitudinal (F_X and M_X), lateral (F_Y and M_Y), and vertical (F_Z and M_Z) forces and moments produced by the rotor. The HIGE test points were run for 30 seconds at a rate of 1,000Hz, resulting in 30,000 data points per axis for each test point, while the HOGE test points were run for 90 seconds or 90,000 test data points. Figure 3.1 gives an example of the raw thrust F_Z and torque M_Z rotor data collected for a single test point corresponding to $\theta_0 = 7$ deg, $\theta_\text{g} = 0$ deg, and $z/R = 2.0$, with the orange trend representing M_Z and the blue trend F_Z. These time histories were averaged to obtain mean values for the thrust and torque. These mean values were subsequently non-dimensionalized into coefficient of thrust C_T and coefficient of power C_P using the Buckingham Π dimensional analysis method [1, 36], where the thrust coefficient is given by

$$C_T = \frac{T}{\rho A(\Omega R)^2} \tag{3.1}$$

$$C_P = \frac{P}{\rho A(\Omega R)^3} \tag{3.2}$$

such that Equation 3.2 can be re-expressed as

$$C_P = C_Q = \frac{Q}{\rho AR(\Omega R)^2} \tag{3.3}$$

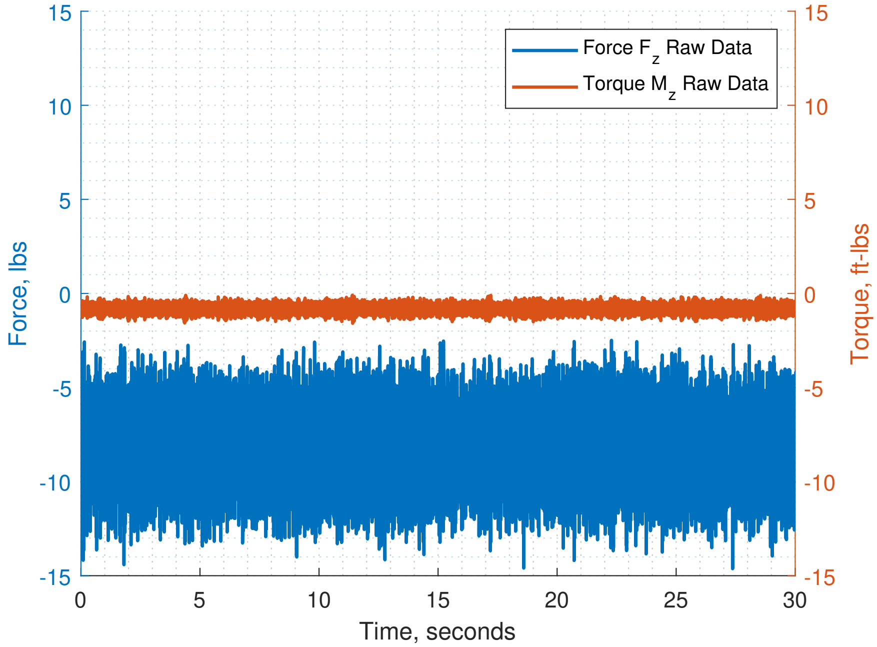

Figure 3.1: Force F_Z and torque M_Z for $\theta_{\mathrm{g}} = 0$ deg, $\theta_0 = 7$ deg, and z/R = 2.0.

where C_T is the nondimensional thrust, T is the rotor thrust, ρ is the air density, A is the rotor disk area, Ω is the angular velocity of the rotor, C_P is the coefficient of power, P is the rotor power required, C_Q is the coefficient of torque, and Q is the rotor torque.

3.2.2 Power Polar Generation

The C_P and C_T values were used to generate power polars. A representative power polar for both HIGE and HOGE data is shown in Figure 3.2, where five blade pitches of 0, 5, 6, 7, and 8 deg were taken for the HIGE and HOGE data sets, with the HIGE data being taken at a z/R of 0.6 and θ_{g} = 0 deg. All power polars used in the present work are included in Appendix A. As expected from prior work [2, 12, 27], an improvement for IGE rotor performance relative to OGE for constant blade pitch and rotor speed was seen, which manifested in the form of an increase in thrust and a slight reduction in power.

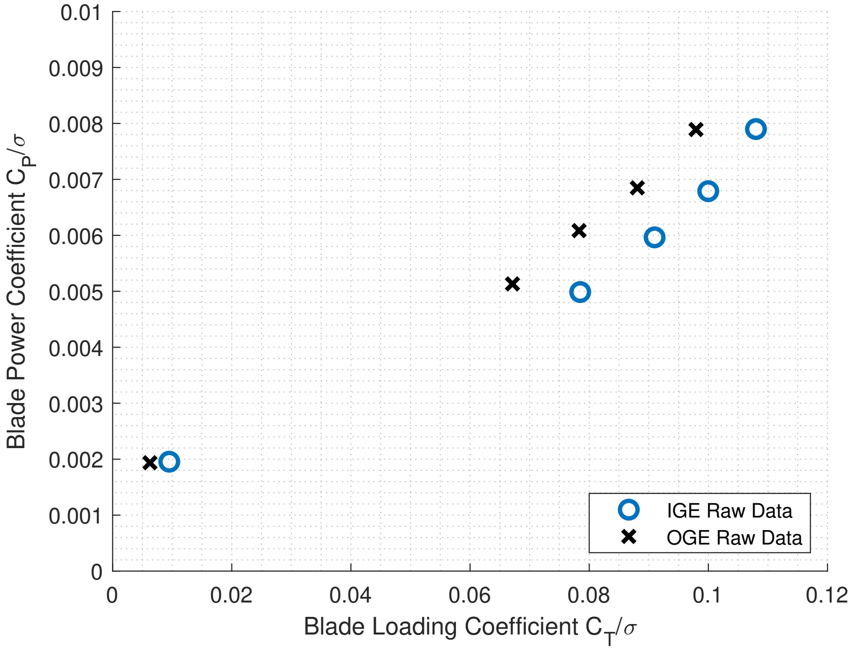

Figure 3.2: Power polars of HOGE data and HIGE data at $z/R = 0.6$ and θ_g = 0 deg.

The present experiment held blade pitch and rotor speed constant, which resulted in thrust and power variations as hub height was changed. However, the power ratio must be calculated on the basis of constant thrust; if power ratios are developed using data points rather than trendlines, there is a possibility of inaccurate power ratio calculations because of non-constant thrust which may lead to under or over predictions of power ratios. Therefore, trendlines were fit to the power polar raw data in order to determine the rotor power required at any thrust within the range of test points. Two curve-fitting models were considered. The first model used a modified momentum theory model given as

$$C_P = \frac{\kappa C_T^{3/2}}{\sqrt{2}} + \frac{\sigma C_{d_0}}{8} + \left(\frac{2C_{d_1}}{3C_{l_\alpha}}\right) C_T + \left(\frac{4C_{d_2}}{\sigma C_{l_\alpha}^2}\right) C_T^2 \tag{3.4}$$

where κ is the induced power factor, C_{d_0} is the constant drag coefficient term equal to 0.009681 ,

C_{d_1} is the linear drag coefficient term equal to 0.005988, C_{l_α} is the lift-curve slope equal to 5.999, and C_{d_2} is the quadratic drag coefficient term equal to 0.4541. Figures 3.3a and 3.3b show the lift curve and drag polar for the NACA 0012 airfoil that comprised each rotor blade, with measured airfoil characteristics taken from [37]. The values of C_{d_0}, C_{d_1}, and C_{d_2} curvefit variables were found through a quadratic fit to the airfoil drag polar, which took the form of

$$C_d = C_{d0} + C_{d1}\alpha + C_{d2}\alpha^2 \tag{3.5}$$

where C_d is the drag coefficient. The lift-curve slope (C_{l_α}) was found through a linear fit of the C_L versus α curve. It is conventional to create curve fits to power polar data in which the airfoil data are determined independently, and the trend of power data is determined through a least squares fit of κ.

The second model utilized a common model in the flight test community which used a second-order fit of total power coefficient with respect to $C_T^{3/2}$, given as

$$C_P = H_0 + H_1 C_T^{3/2} + H_2 (C_T^{3/2})^2 \tag{3.6}$$

where H_0, H_1, and H_2 represent empirical coefficients which were determined by performing a least-squares fit to each power polar data set [12].

Figure 3.4 shows a comparison between the models for a data sample taken for $\theta_\text{g} = 0$ deg and a z/R of 2.0 in order to understand how a lower C_T/σ would affect the fit. with Figure 3.4a omitting $\theta_0 = 0$ deg in the curvefit and Figure 3.4b including $\theta_0 = 0$ deg. The effect of the 0 deg case was tested in order to understand how a lower C_T/σ pitch setting would affect the fit in the

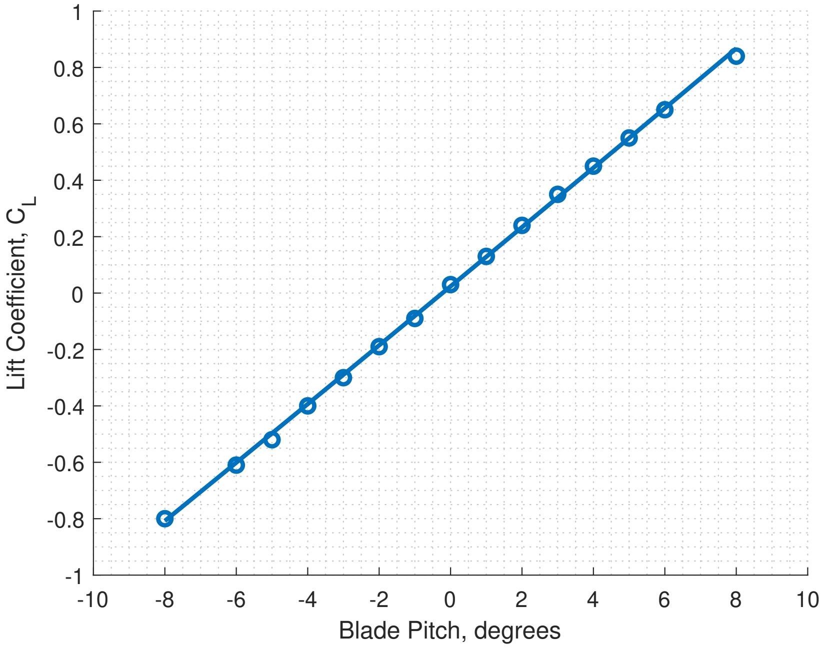

(a) Lift Coefficient.

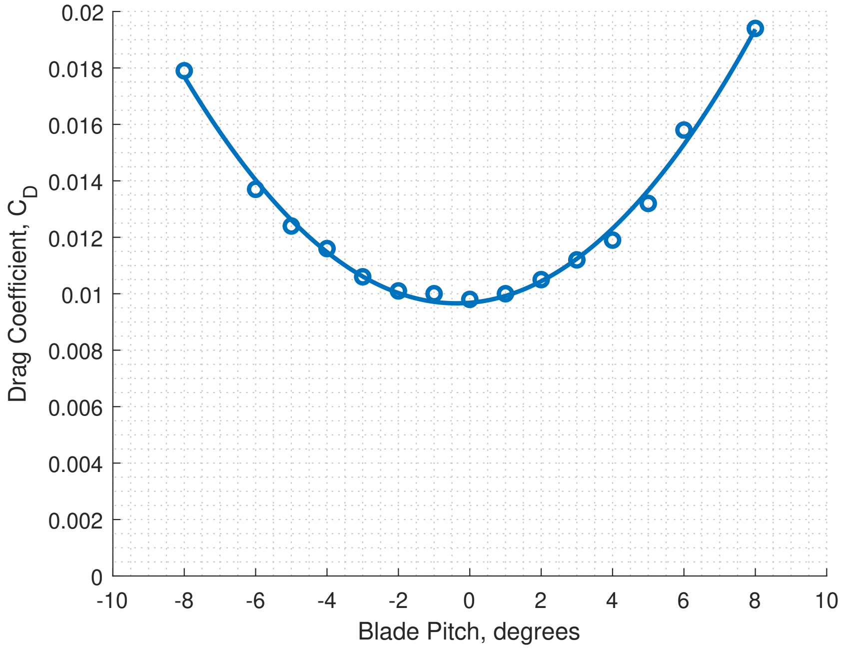

(b) Drag Coefficient.

Figure 3.3: C_L and C_D versus α for an NACA 0012 airfoil. Data from [37].

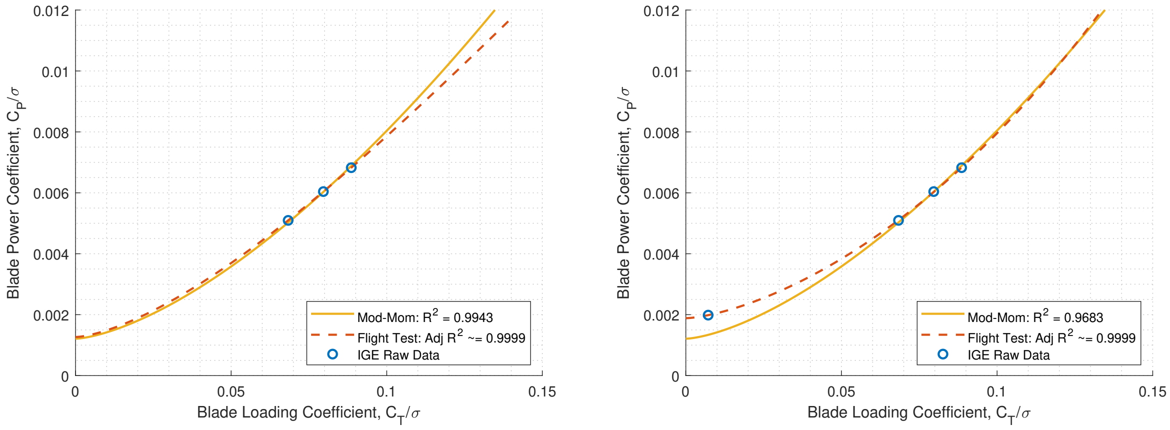

(a) $\theta_0 = 0$ deg not included.

(b) $\theta_0 = 0$ deg included.

Figure 3.4: Comparison of curvefit models for $\theta_g = 0$ deg and $z/R = 2.0$.

region of interest, i.e., $0.065 \leq C_T/\sigma \leq 0.095$.

Figure 3.4a shows both models qualitatively fitting the data well, with only minor divergence seen between the two at C_T/σ values above 0.10, the modified momentum fit returning an R^2 value of 0.9943, while the flight test model returning an R^2 of 0.9999. Figure 3.4b shows the modified momentum model under-predicting the power required at lower C_T/σ because of the C_{d_0} profile power term included in Equation 3.4. However, the flight test model was found to be more sensitive to the fit and could converge to nonphysical conditions, as shown in Figure 3.5 in both traditional and linearized power polar form. Both models still fit the data in the target range of C_T/σ = 0.065–0.095 well, as the modified momentum fit returning an R^2 value of 0.9683 (lower because of the newly added 0 deg point), and the flight test model returning an R^2 of 0.9999. Because of the flight test model having the potential to converge to non-physical conditions for certain data sets, the modified momentum theory model was selected for the current work, with the $\theta_0 = 0$ deg data set omitted from the fit due to the low impact the data has on the model.

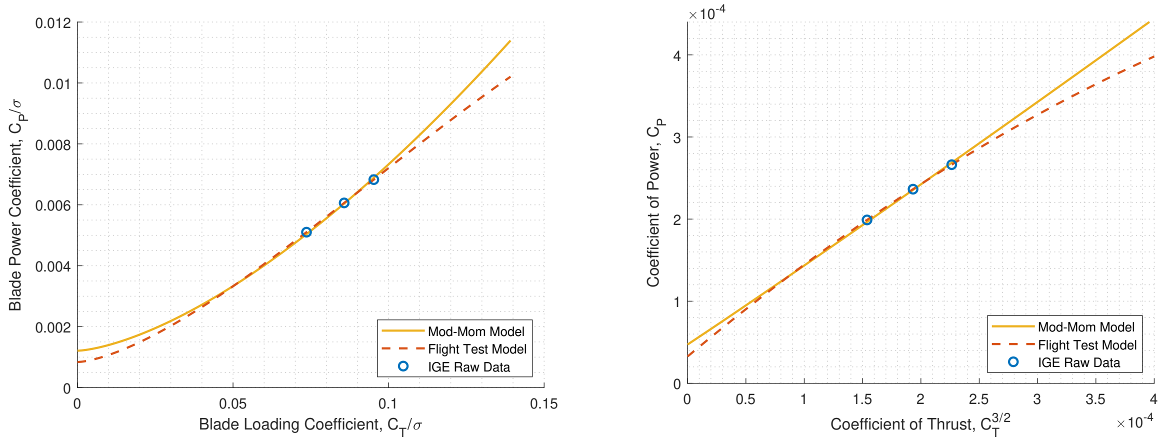

(a) Flight test model inversion shown traditionally. (b) Flight test model inversion shown linearized.

Figure 3.5: Sensitivity of flight test and modified-momentum models to provided data.

Certain collective blade pitches in the IGE and OGE data sets were also required to be omitted from the fit because of lower rotor efficiencies seen at higher C_T/σ. The rotor figure of merit (FM) was used to identify regions of relatively low rotor efficiency. Figure of merit is given by

$$FM = \frac{P_{ideal}}{P_{meas}} = \frac{C_{T_{meas}}^{3/2}/\sqrt{2}}{C_{P_{meas}}} \tag{3.7}$$

where P_{ideal} is the ideal power from momentum theory, P_{meas} is the measured power, $C_{T_{meas}}$ is the measured coefficient of thrust, and $C_{P_{meas}}$ is the measured coefficient of power [1]. Figure 3.6 shows FM as a function of C_T/σ for all HOGE data collected, where each θ_0 is labeled to its corresponding group of data markers. As expected, FM increases with increasing C_T/σ and reaches a maximum of 0.53 at a $\theta_0 = 9$ deg. As blade pitch is further increased, thrust continues to increase but the power increases at a higher rate because of drag, resulting in a reduction in FM. By $\theta_0 = 12$ deg the FM has decreased by 30% from the maximum.

Reduction in rotor efficiency was also seen for HIGE at the highest blade pitches. Figure 3.7 shows FM as a function of C_T/σ for z/R values of 0.6, 1.3, and 2.0, with each colored line and marker representing data for different ground plane angles. For the level ground plane angle case at a z/R of 0.6 as seen in Figures 3.7a and 3.7b, FM is seen to reach a global maximum of 0.65 for $\theta_0 = 7$ deg (23% higher than the HOGE maximum at the same C_T/σ, and decreases to 0.63 for the 8 deg case. Reductions are seen for all θ_g cases at a z/R of 0.6 except 18 deg, which appears to level off at a FM of 0.61 for θ_0 of 7 deg and 8 deg. Drops in FM for $\theta_\mathrm{g} = 0$ deg and 9 deg are also seen for higher rotor hub heights in Figures 3.7c, 3.7d, 3.7e, and 3.7f ,but are not seen for other ground plane angles. Therefore, because of the reduction in FM seen at low hub heights for all θ_g and at higher hub heights for θ_g of 0 and 9 deg, the decision was made to omit the $\theta_0 = 8$ deg data from the curvefit.

The inclusion of $\theta_0 = 5$, 6, and 7 deg for the curvefit also created a better local fit as opposed to a global fit. The present work was interested in the thrust region of $C_T/\sigma = 0.065$–0.095, as this region aligned with the operating regime of the OH-58C. If the 0 and 8 deg blade pitch points were included, a better global fit would have been generated, but at the expense of a worse local fit in the region of interest. Therefore, the present work utilized $\theta_0 = 5$, 6, and 7 deg for HIGE data and $\theta_0 = 4$, 5, 6, 7, and 8 deg for HOGE data, with the 4 and 8 deg HOGE blade pitches being added to provide an accurate power ratio calculation across all hub heights tested.

3.2.3 Power Ratio Determination

A common way to examine the effect of the ground is by using the power ratio, defined as the ratio of the HIGE and HOGE power terms at a constant thrust, and given by

$$\left(\frac{P}{P_\infty}\right)_{(T=\mathrm{const})} = \left(\frac{C_P}{C_{P_\infty}}\right)_{(C_T=\mathrm{const})} \tag{3.8}$$

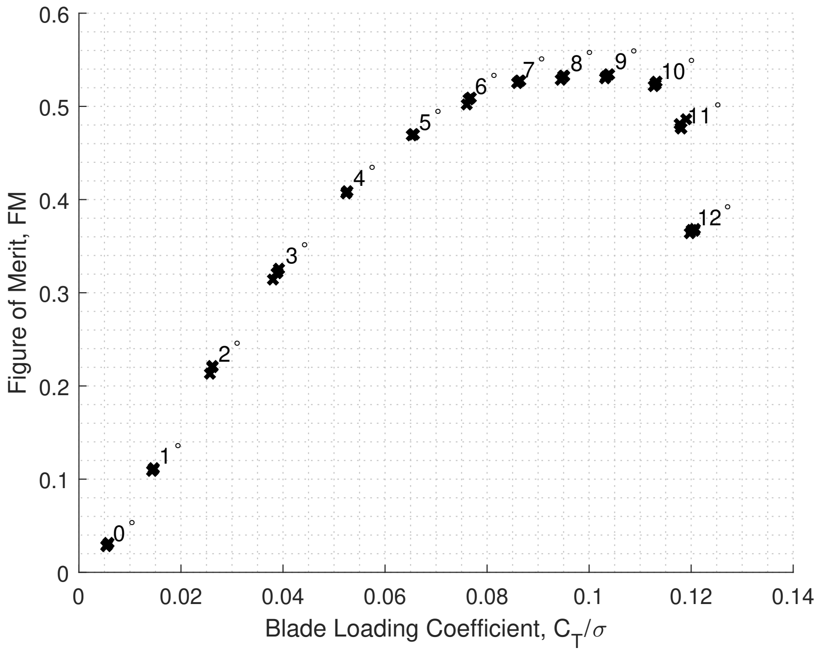

Figure 3.6: Figure of Merit versus C_T/σ for HOGE data set.

The present results have displayed all ground effect plots in the form of power ratios rather than thrust ratios for consistency and relevance to the operational community, as aircrew are often more concerned with their power available than thrust production. Also, because data were recorded for constant blade pitches (i.e., resulting in varied thrust and power, power ratios were computed from the power polar trendlines at specified thrust values. A schematic depicting power ratio development through the use of power polar trendlines at a constant thrust can be seen in Figure 3.8, which depicts a set of HOGE data with the upper black curve, a set of HIGE data with the lower orange curve, and two blue lines with markers depicting a power ratio at a constant thrust and a thrust ratio at a constant power. Notice that individual data points for matched blade pitch values result in variations in power and thrust such that interpolations provide the only appropriate basis for comparative analyses.

Power ratio can be defined using either the total power or induced power, with the latter

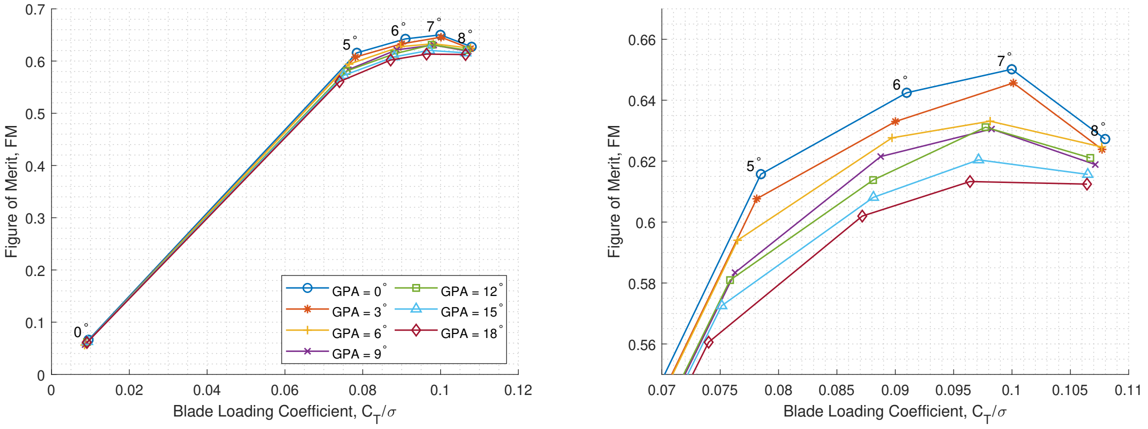

(a) $z/R = 0.6$

(b) $z/R = 0.6$ (Detail)

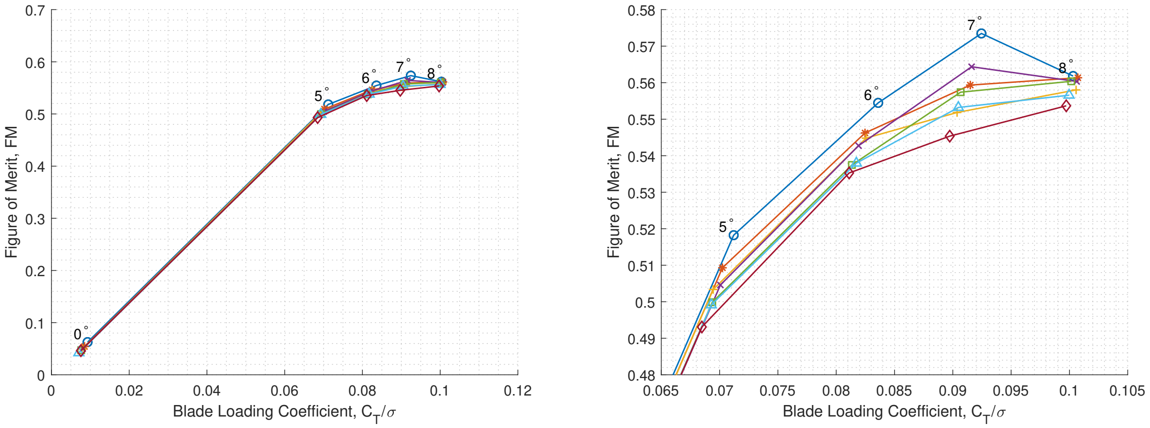

(c) $z/R = 1.3$

(d) $z/R = 1.3$ (Detail)

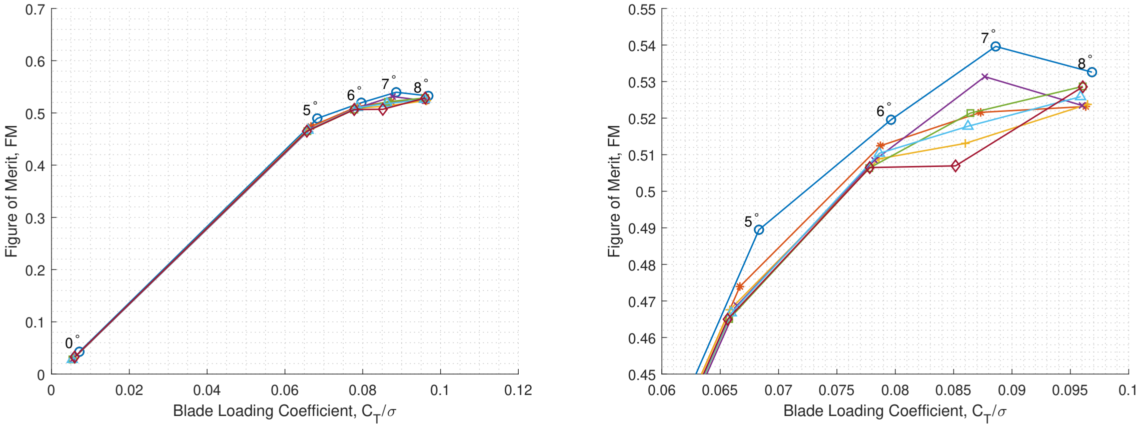

(e) $z/R = 2.0$

(f) $z/R = 2.0$ (Detail)

Figure 3.7: FM versus C_T/σ for three different hub heights.

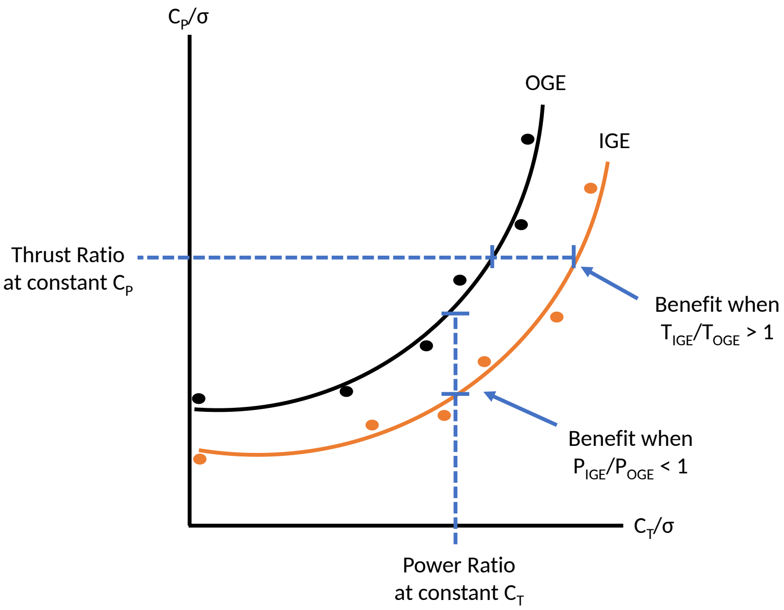

Figure 3.8: Schematic showing the use of trendlines for thrust and power ratio calculations.

subtracting the profile power terms from both the IGE and OGE power polars. Total power ratio plots were ultimately chosen over induced power ratios, as induced power ratios assume constant C_{d_0} values across the entire range of collective blade pitches which was not deemed suitable for the present analysis.

3.3 Effect of Ground Plane Angle on Hover Performance

Surface and contour plots of C_P/σ as a function of both z/R and C_T/σ are shown in Figures 3.9a–3.9g with each sub-figure representing a different ground plane angle. Each three-dimensional surface and two-dimensional contour plot is color coded, with blue colors indicating greater performance benefits and red colors indicating lesser performance benefits or possibly performance penalties above HOGE. The grey surface at a power ratio equal to 1.0 represents where HIGE power is equal to the HOGE power and separates regions of performance benefits

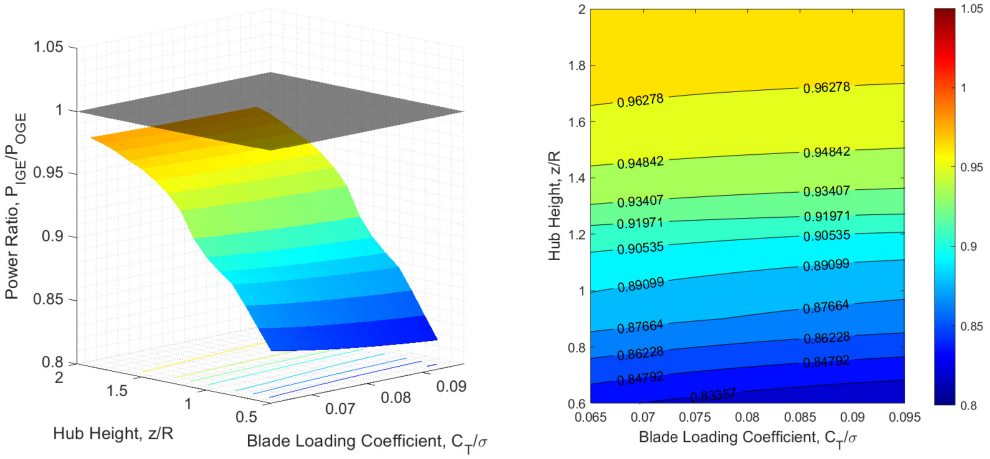

(a) $\theta_\mathrm{g} = 0$ deg.

Figure 3.9: Power ratio surface and contour plots for various θ_g.

(i.e., below the gray plane) and regions of performance penalties (i.e., above the gray plane). During HIGE operations, it is expected that the power required would be less than during HOGE for a constant thrust.

Figures 3.9a–3.9g show the power ratios for all ground plane angles. In general, the power ratios increase as θ_g is increased, which indicates a performance penalty is associated with larger ground plane angles as also noted by [6, 12, 27]. Also noticeable is the relative insensitivity that the power ratios have to changes in C_T/σ. Power ratios corresponding to lower ground plane angles, such as Figures 3.9a or 3.9b, even show a reduction in power ratio (a performance benefit) as C_T/σ is increased; these results will be discussed in greater detail in Section 3.4.

Power ratio minimum and maximum values are seen to differ with θ_g. Figure 3.9a shows the surface plot for $\theta_\mathrm{g} = 0$ deg, where the lowest power ratio value of 0.819 is seen at a z/R of 0.6 (a 22% benefit relative to HOGE), while the highest of 0.977 is seen at z/R of 2.0 (a 2% benefit relative to HOGE). These minimum and maximum values change for different values of θ_g; For example, The $\theta_\mathrm{g} = 6$ deg case shown in Figure 3.9c exhibits a minimum power ratio value

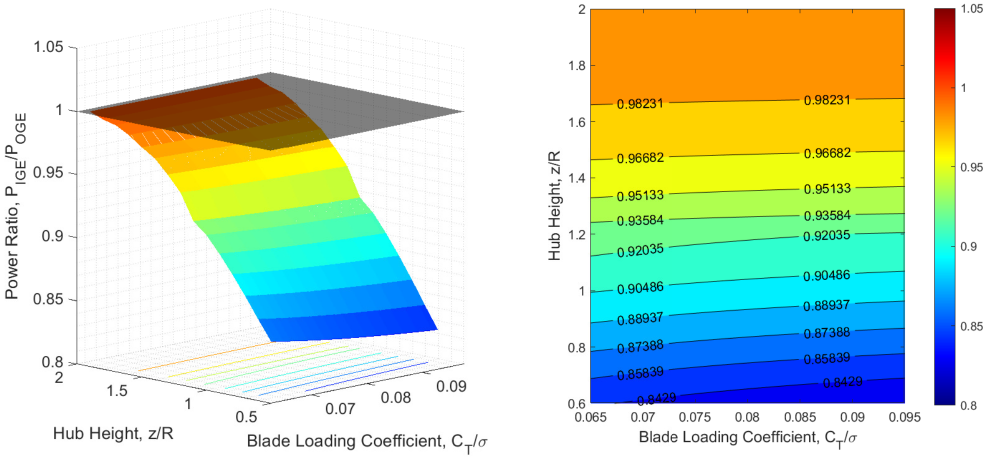

(b) $\theta_g = 3$ deg.

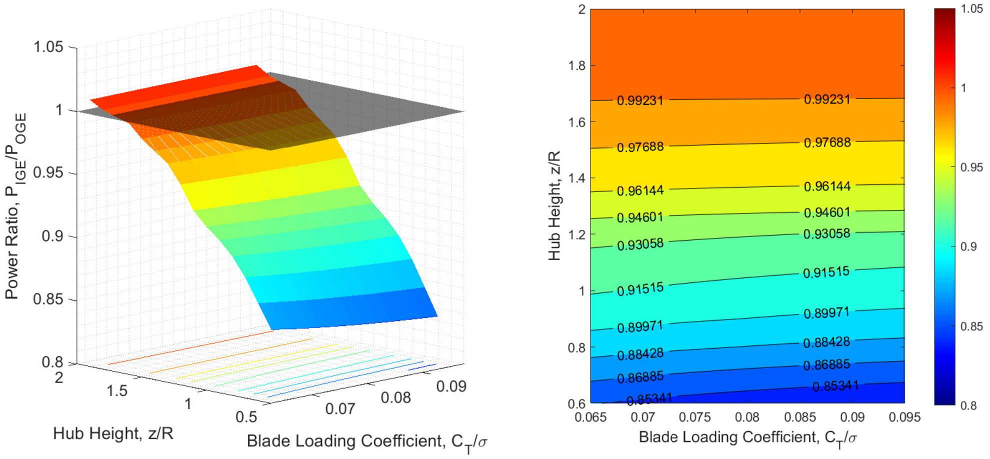

(c) $\theta_g = 6$ deg.

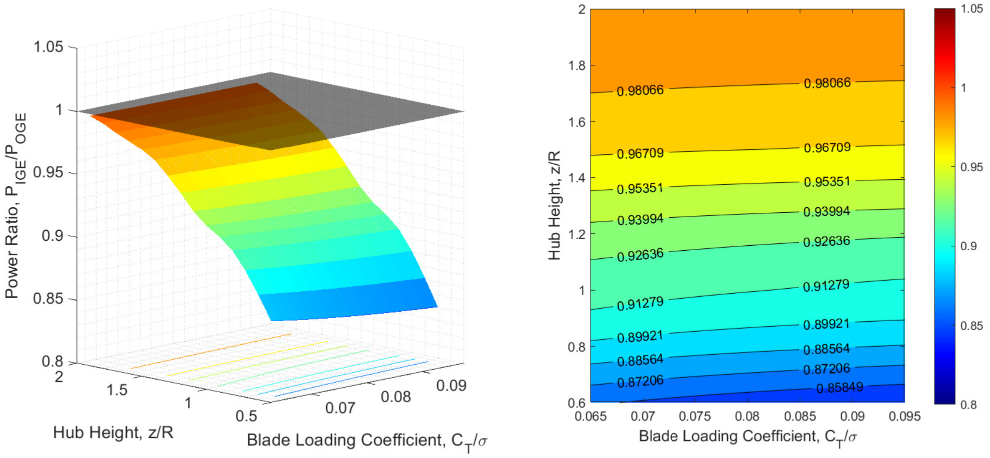

(d) $\theta_g = 9$ deg.

Figure 3.9: Power ratio surface and contour plots for various θ_g.

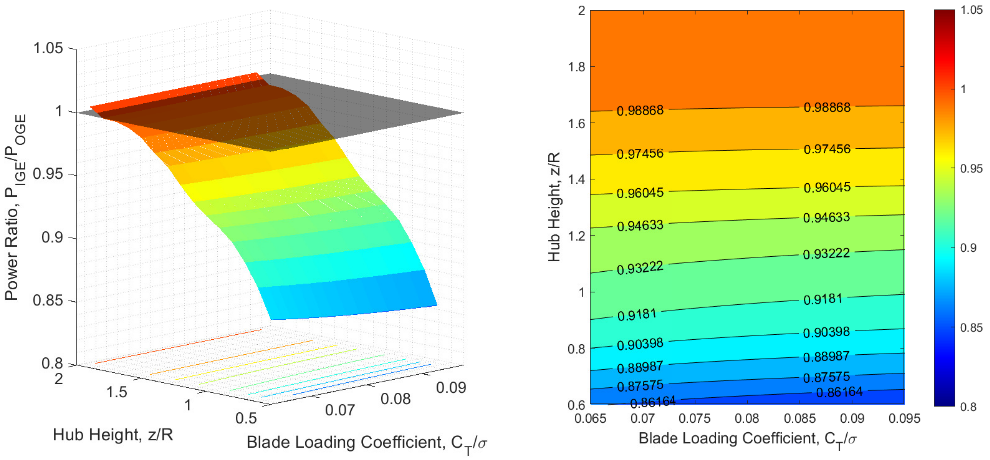

(e) $\theta_g = 12$ deg.

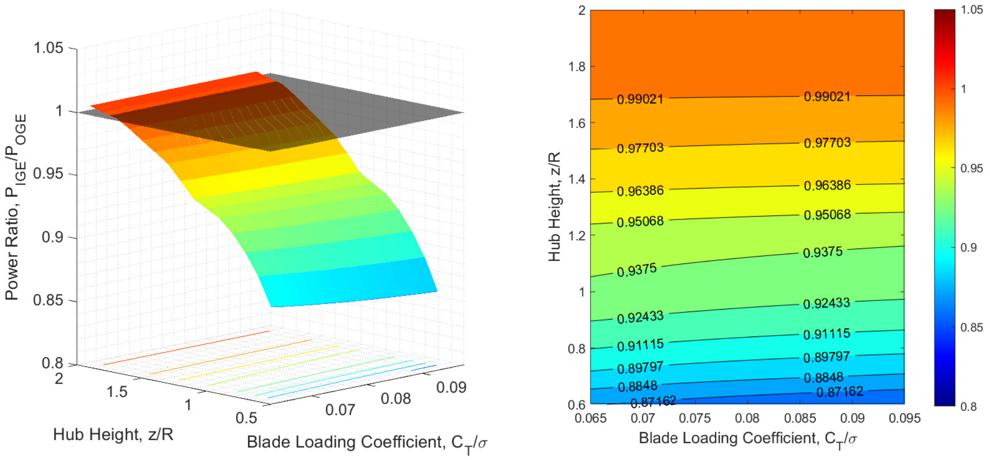

(f) $\theta_g = 15$ deg.

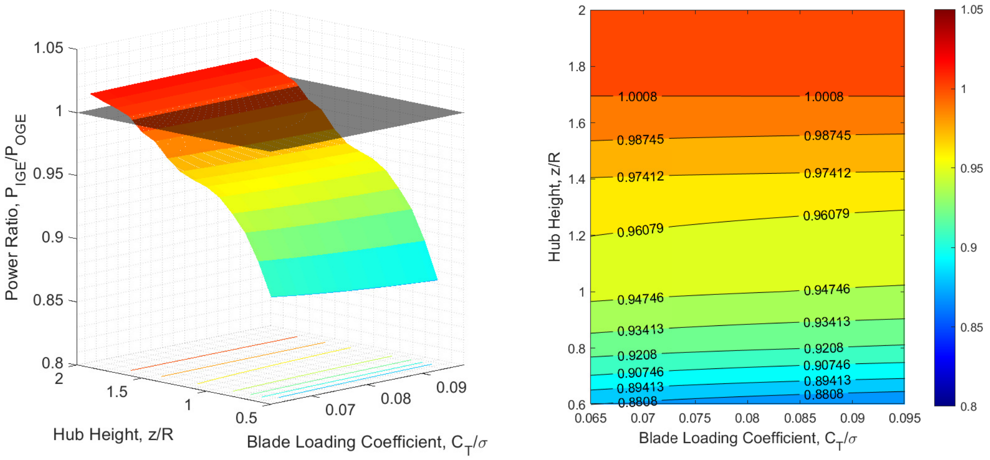

(g) $\theta_g = 18$ deg.

Figure 3.9: Power ratio surface and contour plots for various θ_g.

of 0.838 (a 26$\%$ benefit relative to HOGE) at a z/R of 0.6 a maximum power ratio value of 1.01 (a 1$\%$ performance penalty relative to HOGE) at a z/R of 2.0. Similar performance penalties of 1.0% and 1.5% are seen in Figures 3.9f and 3.9g for $\theta_{\mathrm{g}} = 15$ and 18 deg respectively at a z/R of 2.0. While performance penalties are seen at $z/R = 2.0$, further testing is still needed at hub heights between $z/R = 2.0$ and OGE to determine the height at which hover over sloped terrain ceases to have performance penalties.

The surface plots shown in Figure 3.9 can also be represented in two-dimensional form as shown in Figure 3.10, which shows power ratio as a function of z/R for various thrust conditions. Each colored trend represents a different ground plane angle with the models proposed by Cheeseman and Hayden models overlaid for reference. Each θ_{g} trend shows a generally monotonic increase in power ratio as z/R increases. However, a "jump" in the data is seen for all ground plane angles at z/R near 1.3, which exhibits a decrease in slope followed by an immediate increase in slope as one moves from lower to higher z/R values. The cause of this jump is not known and further discussion of this phenomenon will be noted in Section 3.6.

Figure 3.10a shows an increase in power ratio as θ_{g} is increased from 0–18 deg. This trend of increased power ratio with increasing θ_{g} is additionally seen in Figures 3.10b, 3.10c, and 3.10d, which suggests that for C_T/σ in the range of 0.065–0.095, an increase in ground plane angle is associated with performance degradation. The result that an increase in power ratio is seen for an increase in ground plane angle was also documented in past work from Fradenburgh, Tritschler et al., and Milluzzo et al. [6, 12, 27].

Inclined power ratios can also be calculated by taking the ratio of the inclined ground power

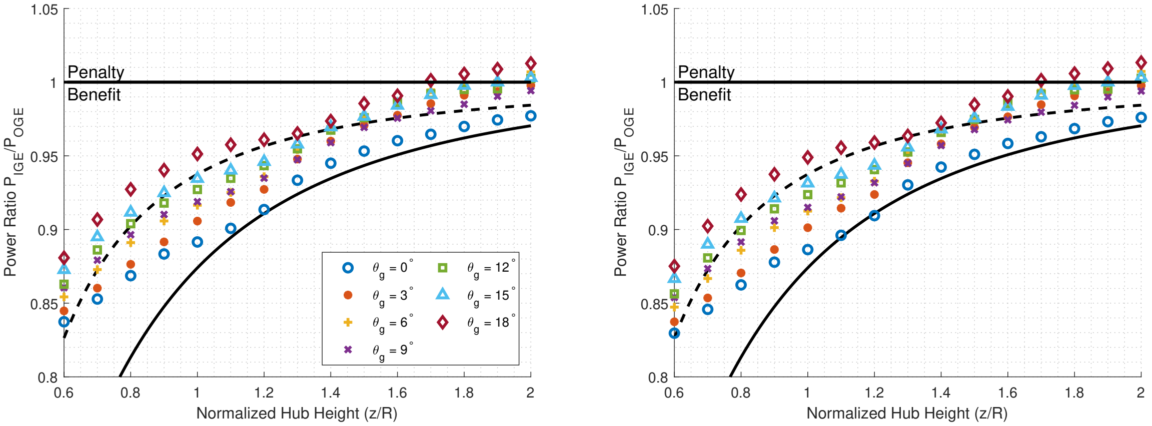

(a) Power ratio versus z/R for $C_T/\sigma = 0.065$.

(b) Power ratio versus z/R for $C_T/\sigma = 0.075$.

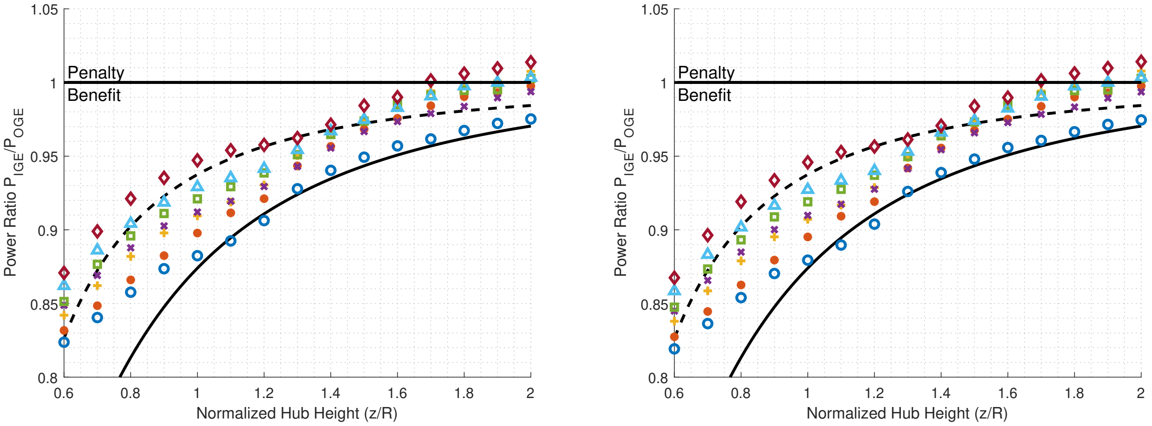

(c) Power ratio versus z/R for $C_T/\sigma = 0.085$.

(d) Power ratio versus z/R for $C_T/\sigma = 0.095$.

Figure 3.10: Power ratio plots of all θ_{g} trends at various C_T/σ values.

by the level ground power, such that

$$\left(\frac{P_{\text{inclined}}}{P_{\text{level}}}\right)_{(T=\text{const})} = \left(\frac{C_{P_{\text{inclined}}}}{C_{P_{\text{level}}}}\right)_{(C_T=\text{const})}. \tag{3.9}$$

where P_{inclined} is the inclined power required, P_{level} is the level power required, $C_{P_{\text{inclined}}}$ is the nondimensional inclined power required, and $C_{P_{\text{level}}}$ is the nondimensional level power required. Figure 3.11 shows the inclined power ratio between level ground and all inclined ground cases as a function of hub height. We again note that a large jump is seen in the inclined power ratio curves at z/R of 1.2–1.4, which suggests the possibility of non-intuitive performance changes at this particular hub height. Further discussion of this observation will be given in Section 3.6. Figures 3.11a–3.11d show that the shape of the sloped terrain trends do not change as C_T/σ is changed, which was previously observed with the power ratio surfaces having similar shapes regardless of θ_{g} as shown in Figure 3.9. The inclined power ratio does slightly change with variation in C_T/σ, with the greatest inclined power ratio values corresponding to a $C_T/\sigma = 0.095$; see Figure 3.11d. The largest performance penalty of 7.5% relative to HIGE above level terrain was observed for the highest ground inclination angle of 18 deg at $z/R = 0.8$.

The hub height that the maximum power ratio occurs at is found to be dependent on ground plane angle. For ground plane angles of 9–18 deg, maximum inclined power ratios are seen at low hub heights around $z/R = 0.8$; see Figure 3.11d. However, lower ground plane angles of 3 and 6 deg exhibit maximum power ratios at a z/R of 2.0. This result suggests that lower ground plane angles show their greatest penalties over level terrain at higher z/R, a result which is non-intuitive. An example is seen in Figure 3.11d; at a z/R of 2.0, the $\theta_{\text{g}} = 6$ deg trend has a greater power ratio value than all other angles except $\theta_{\text{g}} = 18$ deg, but at a z/R of 0.6 the $\theta_{\text{g}} = 6$

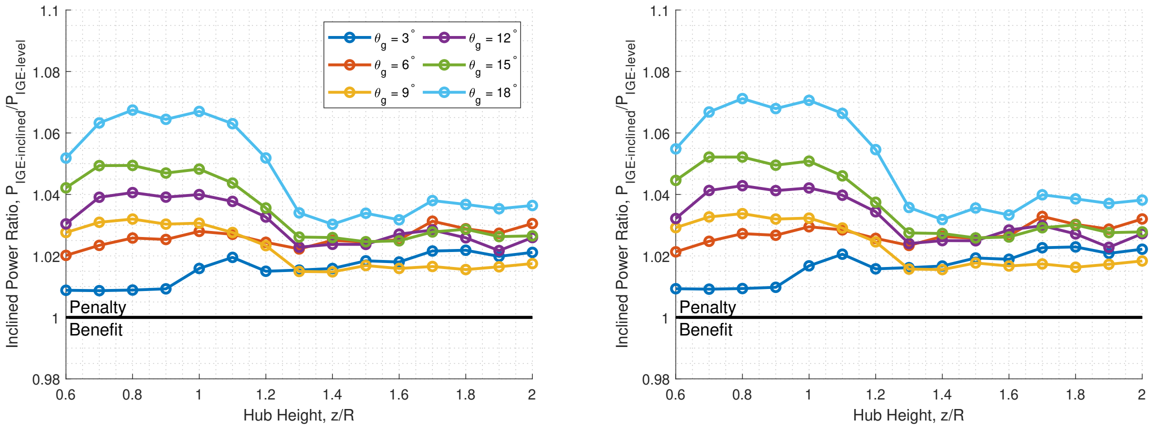

(a) $C_T/\sigma = 0.065$ (b) $C_T/\sigma = 0.075$

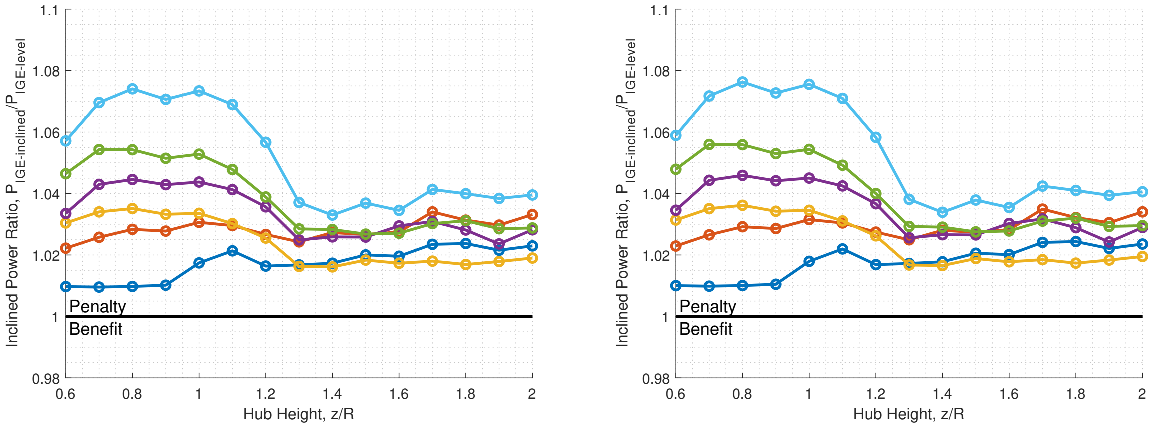

(c) $C_T/\sigma = 0.085$ (d) $C_T/\sigma = 0.095$

Figure 3.11: Power ratio comparison between sloped and level ground planes.

deg trend exhibits the second lowest power ratio. Also, power ratio appears more sensitive to changes in θ_g at lower versus higher z/R. Hub heights from $z/R = 0.6$–1.0 see anywhere from a 1% to 7% performance penalty over level terrain, while $z/R = 1.4$–2.0 only incur performance penalties from 2% to 4%.

Rotor Figure of Merit (FM) can also be compared between ground plane angles. Figure 3.7 showed FM as a function of C_T/σ for various ground plane angles at z/R of 0.6, 1.3, and 2.0. Figure 3.7b showed the FM curves for all ground plane angles at a z/R of 0.6; all θ_g with the exception of 18 deg are seen to experience reductions in FM when the collective pitch was increased from 7 and 8 deg, which suggests a reduction in rotor efficiency at the highest collective blade pitches. This drop in FM is not the case for higher hub heights. Figures 3.7d and 3.7f show a reduction in FM between θ_0 of 7 to 8 deg only for θ_g of 0 and 9 deg. The fact that the level ground case experiences a reduction in FM for all hub heights while the majority of sloped terrain cases do not suggests that sloped terrain may delay the reduction in rotor efficiency for a rotor coming into ground effect at a constant blade pitch corresponding to high C_T/σ.

Finally, ground plane angle was also found to have a slight effect on profile power. Figure 3.12 shows a collection of 0 deg collective blade pitch data for all ground plane angles in terms of C_P/σ versus z/R, where the black dashed line represents the mean profile power required in HOGE. Figures 3.12a through 3.12e appear to have a sharp increase in power from z/R of 0.6 to 1.0, followed by a slight reduction in power. In contrast, ground plane angles of 15 and 18 deg appear to consistently decrease in power over the entire range of hub heights and approach the HOGE profile power value. The maximum power values also appear to differ, with θ_g from 0–12 deg reaching a maximum C_P/σ of 2.00×10^{-3}, while θ_g of 15 and 18 deg only reaching a maximum C_P/σ of 1.97×10^{-3}. Although these changes in profile power are slight, they suggest that profile power is reduced for rotors operating over sloped terrain versus level terrain at z/R of 1.0 and above.

The real-world implications of the penalties seen at higher θ_g values in the present section are that helicopters will require more power to hover when operating in-ground-effect over sloped terrain than over level terrain, with penalties of 7% over the level terrain case for the highest θ_g tested. Additionally, the present work is consistent with the flight-test findings of Tritschler et al. [12] shown in Figure 1.13a, which saw that flight-test HIGE operations over sloped terrain resulted in performance penalties up to 5% above HOGE for a θ_g of 12 deg; the present work

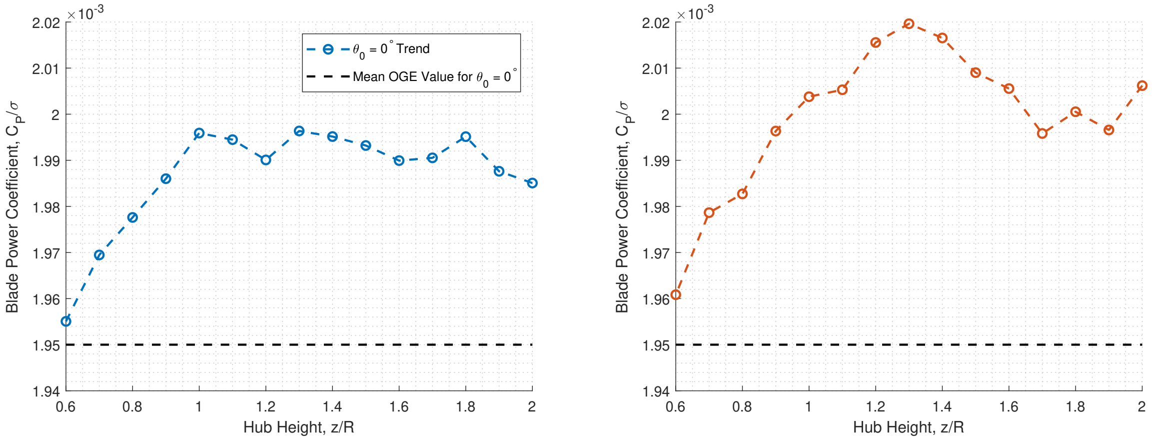

(a) $\theta_{\text{g}} = 0$ deg (b) $\theta_{\text{g}} = 3$ deg

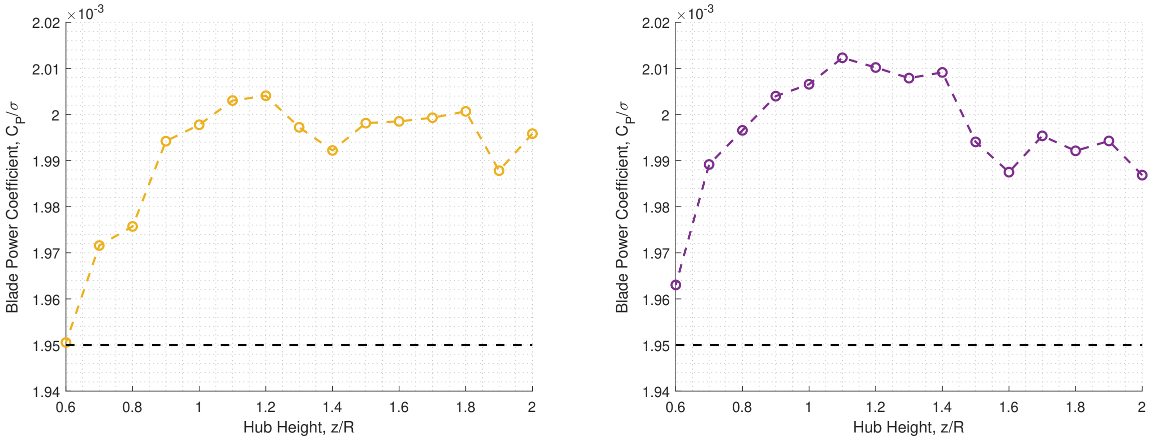

(c) $\theta_{\text{g}} = 6$ deg (d) $\theta_{\text{g}} = 9$ deg

Figure 3.12: C_P/σ as a function of z/R for all $\theta_0 = 0$ deg data.

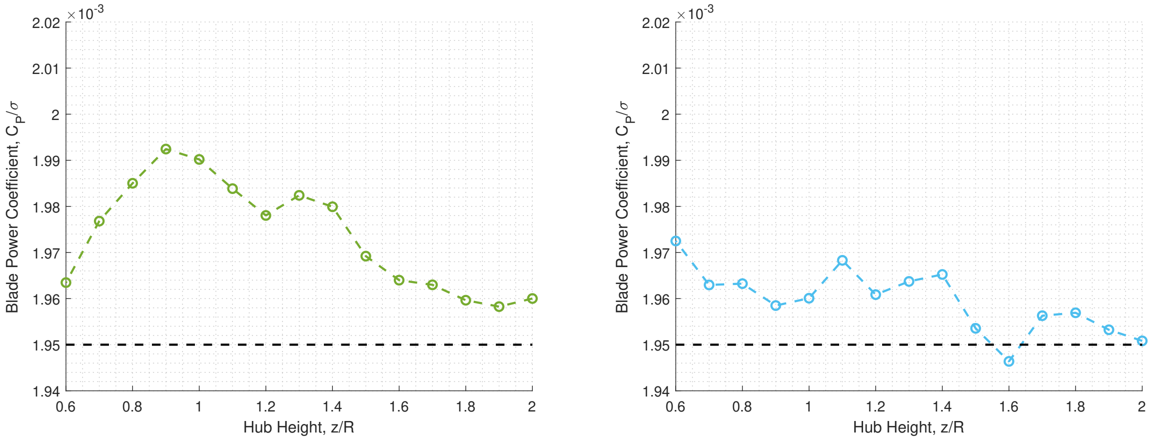

(e) $\theta_\mathrm{g} = 12$ deg (f) $\theta_\mathrm{g} = 15$ deg

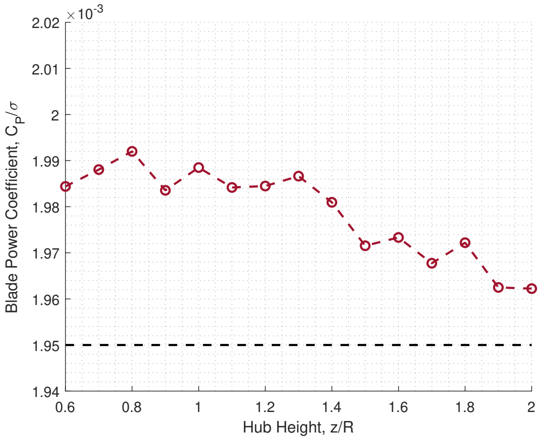

(g) $\theta_\mathrm{g} = 18$ deg

Figure 3.12: C_P/σ as a function of z/R for all $\theta_0 = 0$ deg data.

also saw performance penalties 1.5% above HOGE for a θ_{g} of 18 deg. The lab results shown in Figure 1.13b do not show the power ratio exceeding a value of 1.0; however, their experiment only tested to a maximum z/R of 1.5 whereas the present only observed performance penalties above HOGE for z/R of 1.7 and above.

3.4 Effect of Blade Loading Coefficient on Hover Performance

The effect of blade loading coefficient C_T/σ on power ratio was also investigated in the present work. Figure 3.13 shows power ratio as a function of C_T/σ, with each subfigure representing a different z/R. Each colored marker represents results from different ground plane angles, and the black horizontal line at a power ratio of 1.0 separates regions of performance benefit and penalty.

Figure 3.13a, which corresponds to a z/R of 0.6, shows a reduction in power ratio for $\theta_{\mathrm{g}} = 0$ deg as z/R is increased from 0.6 to 2.0; with a power ratio of 0.8374 at a z/R of 0.6 and a power ratio of 0.8192 at a z/R of 2.0, corresponding to a performance benefit of 2.2%. Similar reductions in power ratio are also seen for all other θ_{g} at this hub height, although for a smaller performance benefit. This finding does not align with previous research done by Zbrozek and Cheeseman [2, 4],who found that for a level ground plane, an increase in C_T/σ results in a reduction in ground effect benefit (increase in power ratio value), regardless of rotor hub height. Similar performance benefits for the level terrain case can be seen for the remaining hub heights shown in Figures 3.13b, 3.13c, and 3.13d, albeit to a lesser extent as hub height is increased, such that the performance benefit for level terrain at a z/R of 2.0 is only 0.3% between the lowest and highest C_T/σ. Certain ground angles such as $\theta_{\mathrm{g}} = 18$ deg also show complete insensitivity to

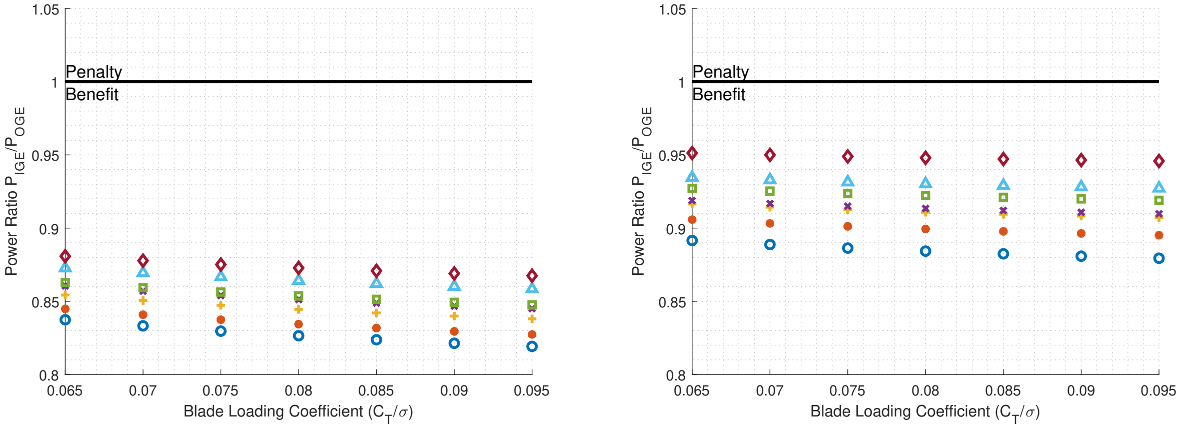

(a) $z/R = 0.6$.

(b) $z/R = 1.0$.

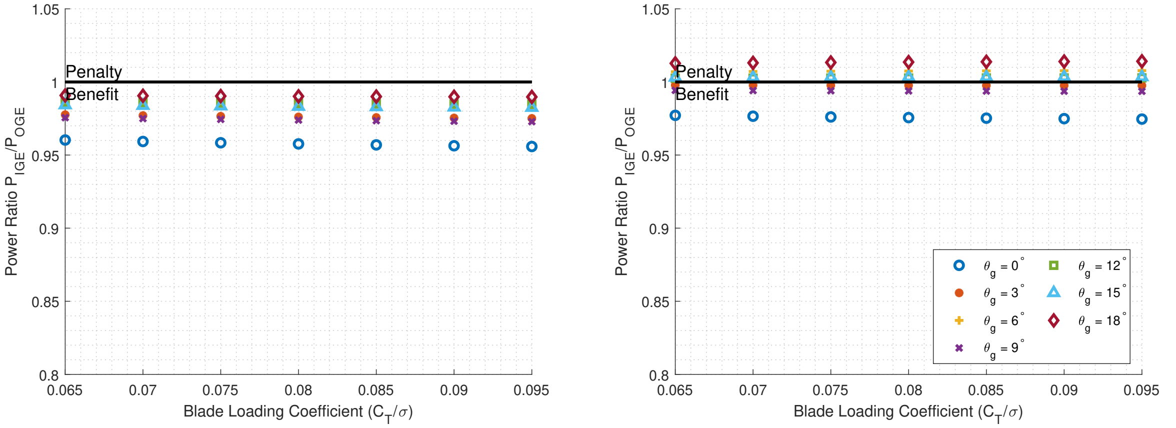

(c) $z/R = 1.6$.

(d) $z/R = 2.0$.

Figure 3.13: Power ratio as a function of C_T/σ for various z/R.

changes in C_T/σ at higher hub heights, such as seen in Figure 3.13b. Additionally, all sloped terrain cases show a general insensitivity to changes in C_T/σ in Figure 3.13d. This finding that C_T/σ sensitivity is reduced at higher z/R has been previously noted by Cheeseman for the case of level terrain [2], but the finding that level terrain exhibits a performance benefit as C_T/σ is increased is inconsistent with results given by Tritschler et al. and Milluzzo et al [12, 27].

The sensitivity of power ratio to changes in C_T/σ can be better seen in Figure 3.14, which shows power ratio as a function of z/R for multiple C_T/σ, with each subfigure corresponding to a different θ_{g}. For all θ_{g}, the sensitivity of power ratio to C_T/σ is highest at a z/R of 0.6. Figure 3.14a, which corresponds to θ_{g} of 0 deg, shows a difference of 0.020 between the lowest and highest power ratios at a z/R of 0.6; at a z/R of 2.0, a power ratio difference of only 0.0029 is seen. Similar behavior can be seen with the sloped terrain. The sensitivity to C_T/σ appears to decrease as ground plane angle is increased. Figure 3.14g, which corresponds to θ_{g} of 18 deg, only shows a power ratio difference of 0.013 at a z/R of 0.6 and of 0.0014 at a z/R of 2.0.

The present work has found power ratio to be relatively insensitive to C_T/σ even at the lowest hub height of $z/R = 0.6$, with the maximum difference in power ratio between the lowest and highest thrust setting to be only 0.02. Previous research by Cheeseman [2] found the power ratio difference at a z/R of 0.6 to be approximately 0.05, as shown in Figure 1.4. Additionally, multiple sources have found power ratio to decrease as C_T/σ is increased [2, 4, 12]. Future research is needed to further investigate the model used to generate power polar curvefits, as the chosen model and included data sets will determine the resulting power ratios.

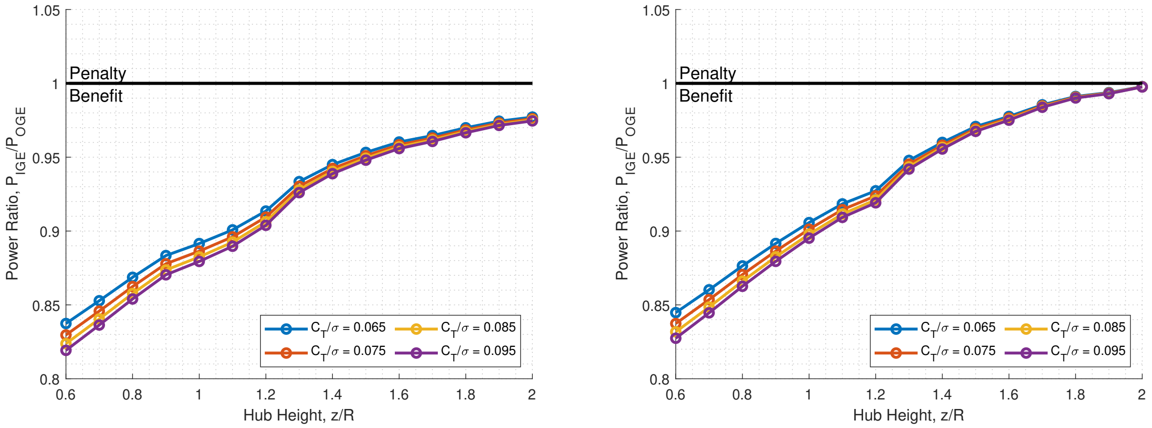

(a) $\theta_{\text{g}} = 0$ deg (b) $\theta_{\text{g}} = 3$ deg

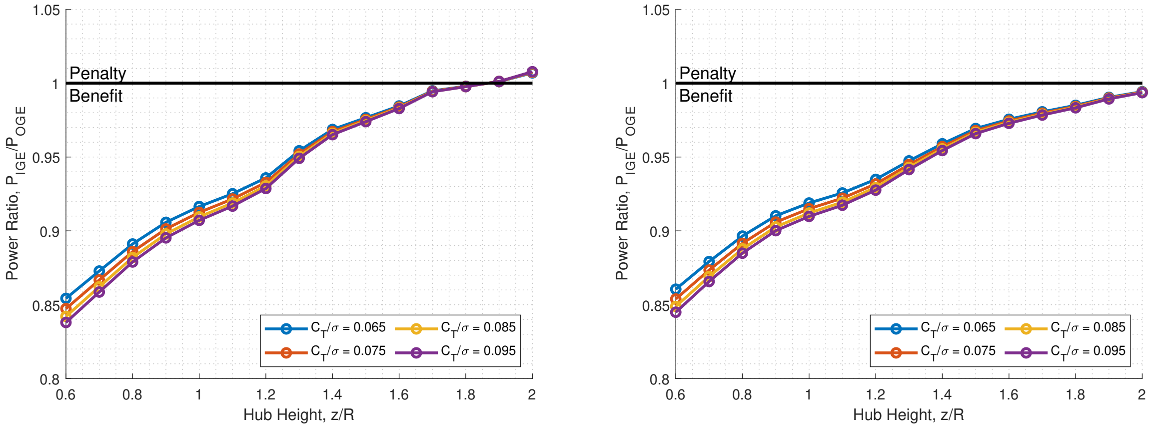

(c) $\theta_{\text{g}} = 6$ deg (d) $\theta_{\text{g}} = 9$ deg

Figure 3.14: Power ratios of all C_T/σ at various θ_{g}.

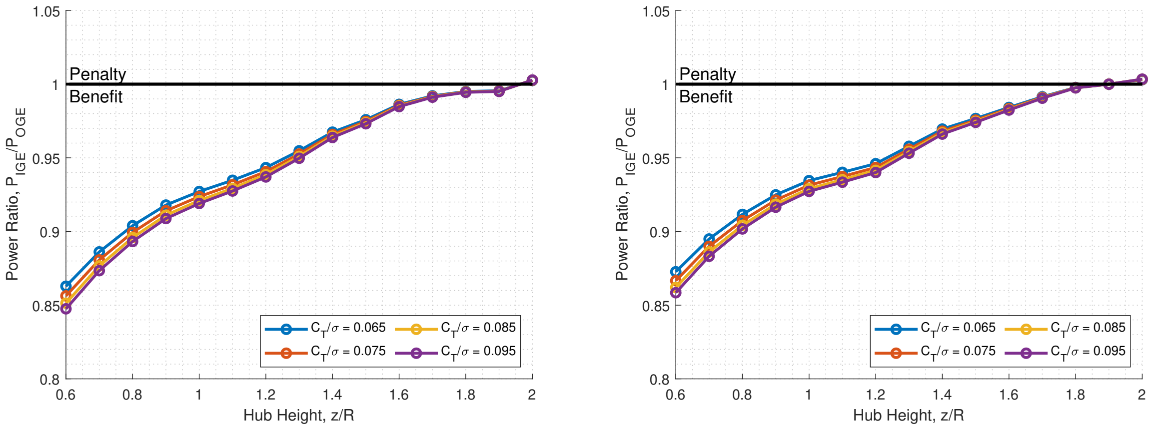

(e) $\theta_{\rm g} = 12$ deg (f) $\theta_{\rm g} = 15$ deg

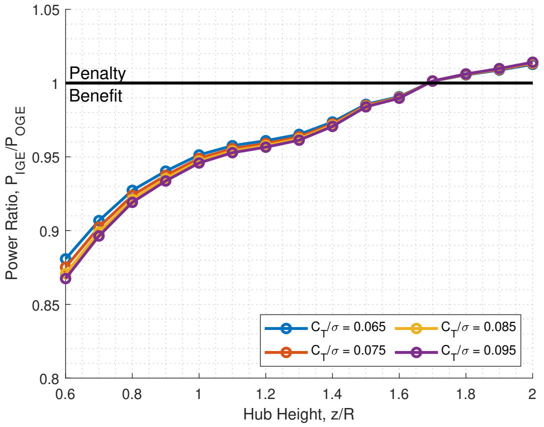

(g) $\theta_{\rm g} = 18$ deg

Figure 3.14: Inclined power ratios of all C_T/σ at various $\theta_{\rm g}$.

3.5 Semi-Empirical Power Ratio Model

A semi-empirical model was developed to generate power ratio predictions at various ground plane angles. As shown in Figure 3.10, a generally monotonic increase in power ratio was seen for all ground plane angles as z/R was increased, regardless of thrust setting. This monotonic increase for both level and sloped terrain showed similarities to the shape of the analytical Cheeseman model. A first effort was made to model the sloped terrain effects on power ratio utilizing the form of the Cheeseman analytical model as given in Equation 1.2 though the coefficients were determined via least-squares fit, i.e.,

$$\left[\frac{P}{P_\infty}\right]_{T=\text{const}} = \frac{1-(\frac{R}{x_2 z})^2}{x_1} \tag{3.10}$$

where x_1 and x_2 represent the coefficients which were determined by the least squares method for each data set of power ratio as a function of hub height. Note that an increase in x_1 corresponds to a reduction in power ratio value (performance benefit) and vice-versa, and an increase in x_2 corresponds to an increase in power ratio (performance penalty) and vice-versa.

Figure 3.15 shows power ratio trends similar to the ones shown in Figure 3.10 overlaid with their respective semi-empirical models, where each sub-figure corresponds to a different C_T/σ. With the exception of the $\theta_\text{g} = 9$ deg trend, we see that a vertical shift in the semi-empirical trend occurs with an increase in ground plane angle, similar to that seen with the underlaid power ratio data. While the model shows moderate agreement with the data, the trends in the x_1 and x_2 coefficients provide unique insight into the effects of ground inclination as a well as the ability to predict the rotor performance under these conditions.

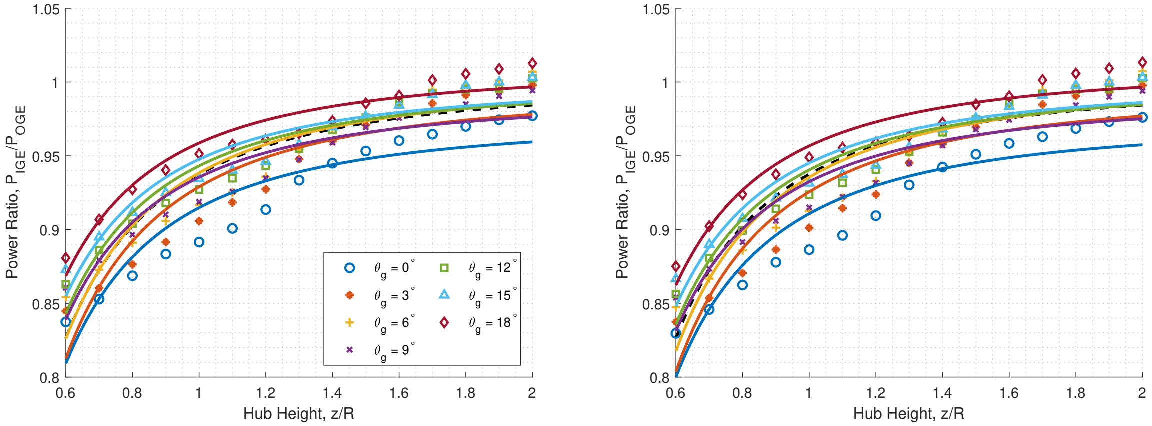

(a) $C_T/\sigma = 0.065$.

(b) $C_T/\sigma = 0.075$.

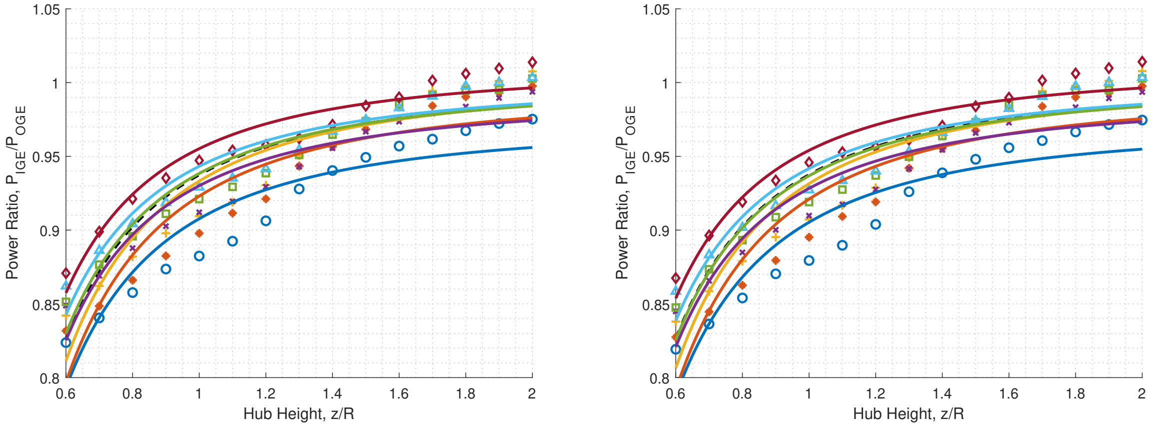

(c) $C_T/\sigma = 0.085$.

(d) $C_T/\sigma = 0.095$.

Figure 3.15: Semi-empirical Cheeseman trendlines and power ratio data for various C_T/σ.

The two coefficients, x_1 and x_2 obtained from the least-squares fit to the classical ground effect equation are shown as a function of θ_g and θ_0 in Figure 3.16, with the vertical axis corresponding to x_1 and the horizontal to x_2. The values predicted analytically by Cheeseman and Bennett of $x_1 = 1$ and $x_2 = 4$ (from Equation 1.2) are plotted and denoted with a black star. Additionally, each C_T/σ is denoted with its own symbol and each θ_g with its own color.

Notice that the value of x_1 decreases as θ_g is increased; the level terrain case exhibits x_1 values from 1.026 to 1.03, and the values of x_1 in general decrease until reaching θ_g of 18 deg with x_1 values around 0.99. As C_T/σ is increased, the values of x_2 decrease for all ground plane angles tested. For example, the level case exhibits an x_2 value of 4.05 for the $C_T/\sigma = 0.065$ case, but then decreases to 3.85 for the $C_T/\sigma = 0.095$ case. In general, a decrease in x_1 and an increase in x_2 are related to an increase in ground plane angle. Likewise, a decrease in x_2 is related to an increase in rotor thrust setting. Future work may be undertaken to develop a model similar to Equation 1.6 which includes θ_g as one of many variables for which the power ratio can be solved for.

3.6 Challenges of the Experiment

Because of the experimental nature of the research, there were unique challenges faced which weren't foreseen during the experiment's planning stage. These included the presence of thrust variation at certain hub heights, the presence of "jumps" in thrust at certain hub heights, the drift of data seen across multiple runs, and the sensitivity of power ratio results to the inclusion or omission of specific data points.

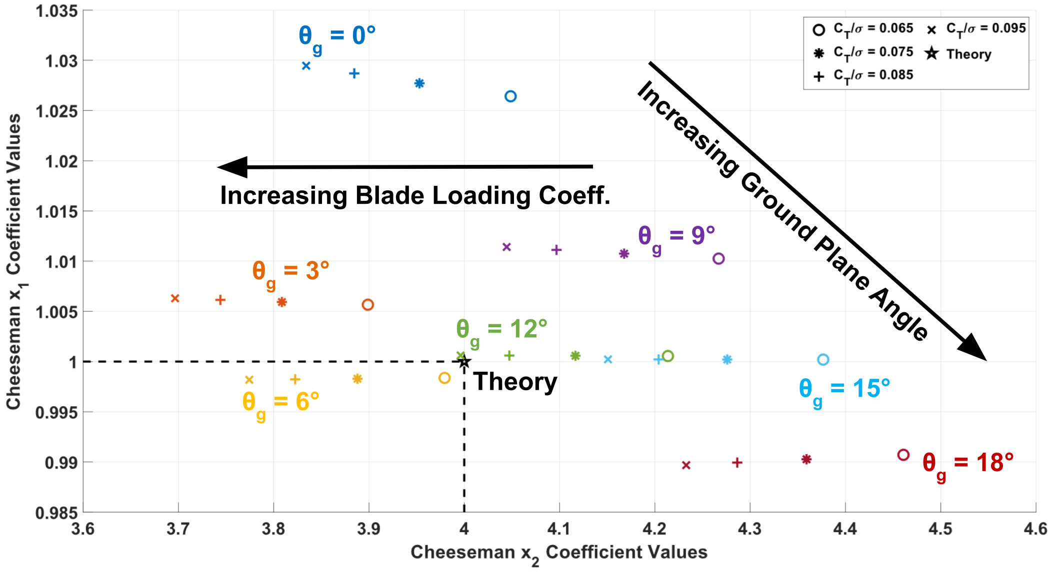

Figure 3.16: Coefficients for all generated semi-empirical trendlines.

3.6.1 Length of Data Collection Time

The 30 second run time was deemed acceptable for most test points in order to obtain a representative average of the force and torque measurements for each run; however, certain points near $z/R = $ 1.2–1.4 showed larger F_Z variation, which had potential to skew the average run values of F_Z and M_Z. Figure 3.17 shows F_Z versus time for a single z/R sweep for $\theta_\text{g} = 0$ deg and $\theta_0 = 7$ deg, where the blue trend corresponds to a filtered time history of F_Z and the orange trends to $F_{Z\text{-mean}}$, or the average value of F_Z across the entire 30 second run. Each run is labeled with its associated z/R; in addition, spaces of 50,000 milliseconds were added between each run and raw F_Z data were filtered for clearer visualization. The F_Z time histories corresponding to z/R of 1.2 and 1.3 can be seen to have a much larger variation in F_Z when compared to other hub heights, and this variation was thought to have an effect on the resulting

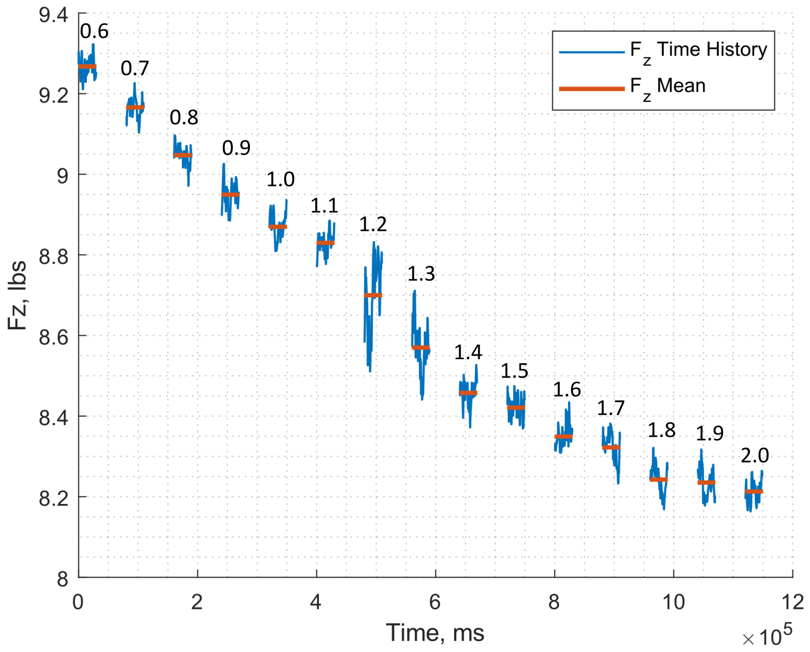

Figure 3.17: Time history of F_Z and $F_{\text{Z-mean}}$ for $\theta_\text{g} = 0$ deg and $\theta_0 = 7$ deg.

$F_{\text{Z-mean}}$. Similar results were seen with other runs around $z/R = 1.2$–1.4.

In order to ensure that the 30 second run time was sufficient, an additional hub height sweep using 90 second runs was conducted and the effect that sample size had on $F_{\text{Z-mean}}$ at these heights was compared. Figure 3.18 shows $F_{\text{Z-mean}}$ as a function of sample size for both the 30 and 90 second runs, where each trend represents a different z/R as labeled on the right side of each plot. $F_{\text{Z-mean}}$ is a function of sample size which represents a forward-sweeping cumulative average of F_Z, where the low end of the sample size is associated with a small F_Z average window, such as from 0 to 1 second, while the high end is associated with a large average window, such as from 0 to 30 seconds. The $F_{\text{Z-mean}}$ corresponding to large sample size windows (right side of each plot) were visually analyzed and both were determined to be converged for both the 30 second and 90 second trials; therefore, the present work was conducted with 30 seconds run times for $F_{\text{Z-mean}}$ calculations.

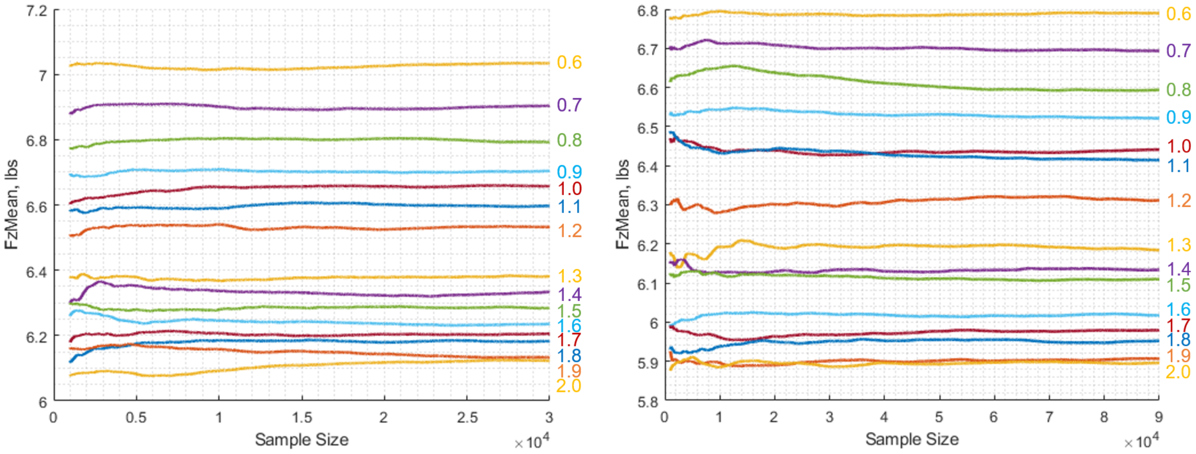

(a) 30 second sample size.

(b) 90 second sample size.

Figure 3.18: Effect of sample size on $F_{\text{Z-mean}}$ for 30 and 90 second runs.

3.6.2 Jumps at Specific Hub Heights

During the data processing, "jumps" were seen for many runs at $z/R = 1.2$–1.4. At first, the jumps were thought to be an artifact of the fit. Both the modified-momentum model and flight test model were compared, and it was found that the jump was slightly worse in the flight test fit, likely because of the difference in curve shape between the IGE and OGE power polars. However, the jump was still present in the modified momentum fit, which prompted the investigation into the raw data trend. Figure 3.19 shows a depiction of the raw data trends for θ_0 of 5 and 6 deg at $\theta_\text{g} = 0$ deg, with the jump region boxed for visualization purposes. Both jumps are seen between z/R of 1.2 and 1.3. On average, the jump magnitude is 0.10 to 0.15 pounds regardless of θ_0; however, the jumps appear more noticeable at lower θ_0 because of the jump magnitude being a higher fraction of the thrust produced.

A concentrated effort was then made to both understand and mitigate these jumps. Three tests were conducted at θ_0 of both 5 and 6 deg:

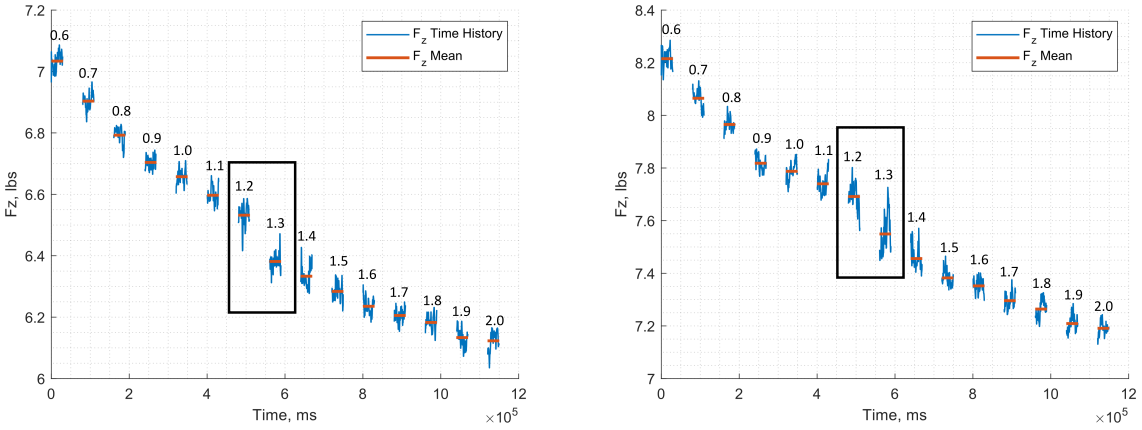

(a) $\theta_0 = 5$ deg

(b) $\theta_0 = 6$ deg

Figure 3.19: Time histories of F_Z and $F_{\text{Z-mean}}$ for θ_0 of 5 and 6 deg at $\theta_\text{g} = 0$ deg.

1. Hub height sweep with flow diverters present to prevent flow recirculation.
2. Hub height sweep with 90 second runs instead of 30 second runs.
3. Hub height sweep with no ground plane attached.

Figure 3.20 shows a comparison of these tests in the form of thrust time histories. Figures 3.20a and 3.20b still clearly show jumps within the z/R of 1.2–1.4 region, while Figure 3.20c shows no clear jump between any of the runs. These findings suggest that recirculation and run time are not related to the jump; rather, something inherent to the setup, such as the ground plane, the proximity of other objects, or the horizontal beam upon which the rotor is mounted, is causing the jump in thrust. Future testing is likely needed to understand the cause of this jump.

3.6.3 Load Cell Taring

Load cell taring was found to be a necessary part of the procedure, lest drift occur in the rotor hub force and moment data. Figure 3.21a shows the drift in measured thrust and power if the load cell was not tared after each hub height sweep. Drift is shown for three θ_0 pitches, with

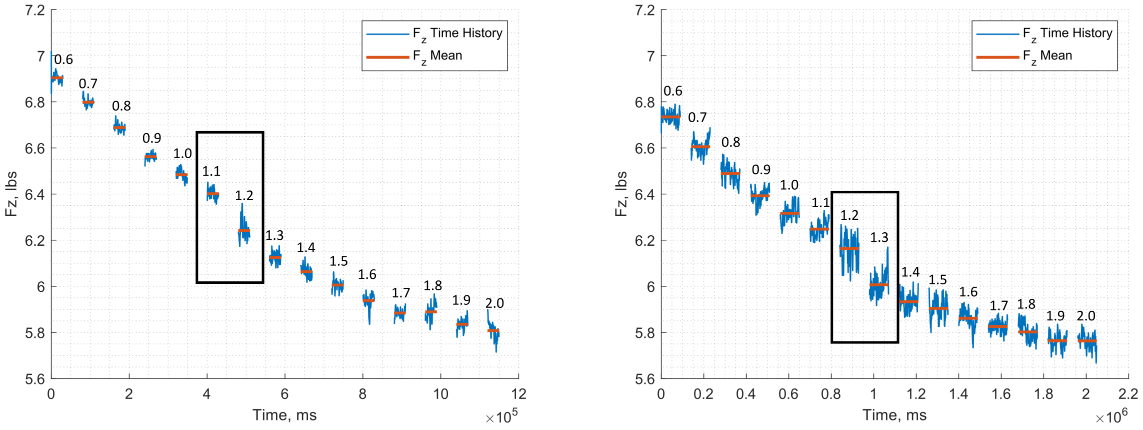

(a) $\theta_0 = 5$ deg and flow diverters.

(b) $\theta_0 = 5$ deg and 90 second runs.

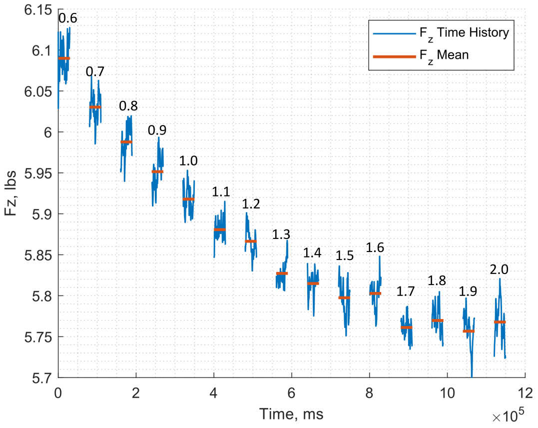

(c) $\theta_0 = 5$ deg and no ground plane.

Figure 3.20: Time histories of F_z and $F_{\text{Z-mean}}$ for θ_0 of 5 deg at $\theta_{\text{g}} = 0$ deg for three different tests.

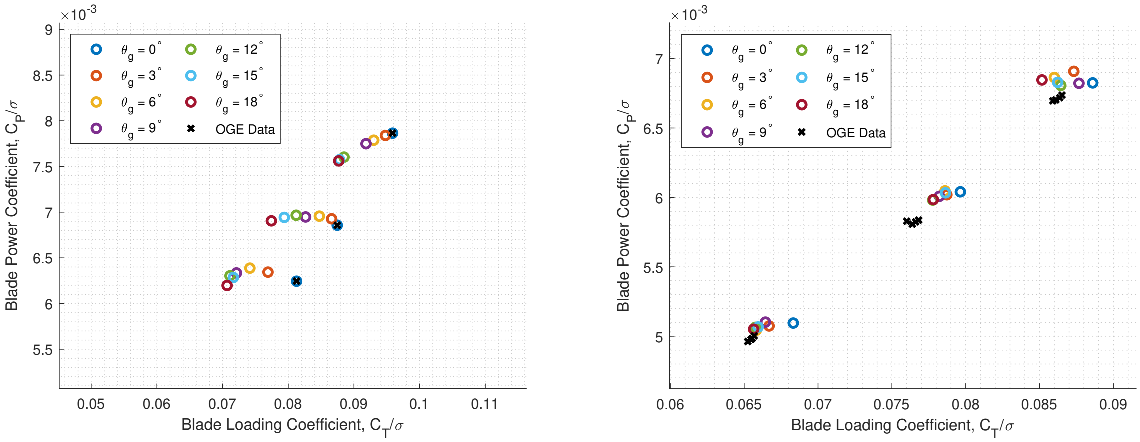

(a) Rotor thrust and power with drift.

(b) Rotor thrust and power without drift.

Figure 3.21: Comparison of rotor thrust and power with and without drift.

each different colored marker corresponding to a different θ_g. As one moves from $\theta_\mathrm{g} = 0$ deg to $\theta_\mathrm{g} = 18$ deg, similar to moving from left to right in the timeline shown in Figure 2.5, thrust and power measurements both reduce in value and all HIGE measurements are located the left of the HOGE data. In contrast, Figure 3.21b shows data which were collected by taring the load cell after each hub height sweep; notice how the HIGE data is primarily located to the right of the HOGE data which is typical behavior and indicates a performance benefit. If this load cell drift had gone unrecognized, the resulting power ratios would have shown greatly exaggerated performance penalties for the sloped terrain cases. Therefore, proper load cell taring was required to obtain accurate performance data.

3.6.4 Power Ratio Sensitivity

Finally, power ratio results were found to be sensitive to the inclusion or omission of certain IGE and OGE data sets. Figure 3.22 shows power ratio as a function of z/R for the case of level ground and $C_T/\sigma = 0.065$, where each trend corresponds to a different data set detailed in the

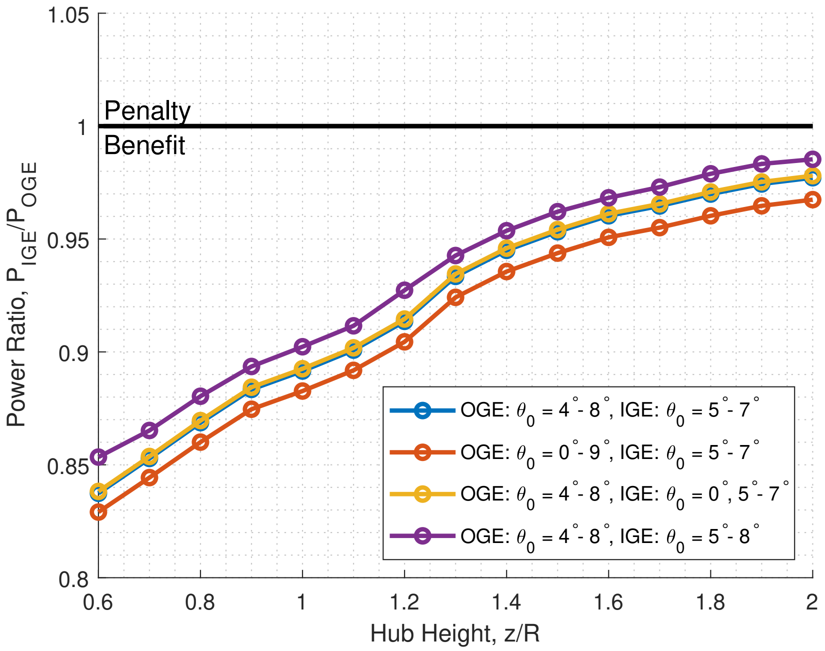

Figure 3.22: Sensitivity of power ratio to changes in power polar data included.

legend of Figure 3.22. The data set used in the present work, shown with the blue trend, was chosen due to the reduction in FM to the $\theta_0 = 8$ deg data and the insensitivity of the modified-momentum theory model to the $\theta_0 = 0$ deg data as discussed in Section 3.2.2, Power Polar Generation. Including $\theta_0 = 8$ deg as shown in the purple trend or including all OGE data points of 9 deg and below as shown in the orange trend was found to result in a power ratio difference of ± 0.01 around the blue trend. The yellow trend, corresponding to the inclusion of $\theta_0 = 0$ deg for the IGE case was found to yield similar results to the blue trend, which omits $\theta_0 = 0$ deg. While the inclusion or omission of certain data points had an effect on the power ratio value, no major difference is seen in the shape of the power ratio curve. Further testing is likely needed to understand best practices for which data points need to be included and which can be omitted for both IGE and OGE data sets.

Chapter 4: Conclusion

4.1 Summary

The present study involved performance testing of an isolated rotor operating over an inclined ground plane at numerous rotor hub heights and collective blade pitch angles. Fifteen different values of z/R from 0.6 to 2.0 (in 0.1 increments), five different collective blade pitches of 0, 5, 6, 7, and 8 deg, and seven different ground plane angles from 0 to 18 deg (in 3 deg increments) were tested during in-ground effect hover operations, as well as 13 different collective blade pitches from 0–12 deg during out-of-ground-effect hover operations. The motivation of the work was to better understand the combined effects that ground plane angle and blade loading coefficient have on isolated rotor hover performance at various rotor hub heights, as compared to level ground and to hover out-of-ground-effect.

Prior laboratory studies of hover within confined areas and flight test studies of hover over sloped terrain have shown performance degradation beyond HOGE, and the present work sought to investigate if similar performance penalties would be seen in more extensive laboratory testing over sloped ground planes. In particular, the present work aimed to expand the work done by Tritschler et al. and Milluzzo et al. [12, 27] for a wider variety of conditions to better understand the effects that sloped terrain has for various hover regimes, and to understand if non-monotonic behavior of power ratio with respect to hub height was present at certain hub heights.

4.2 Conclusions

The following conclusions have been drawn from the present work:

1. An increase in ground plane angle resulted in an increase in total power ratio for the same z/R value. Similarly, an increase in ground plane angle resulted in an increase in total power ratio for the same blade loading coefficient. Therefore, when power ratio was viewed as a function of z/R and blade loading coefficient as shown in the surface plots in Figures 3.9a–3.9g, an increase in ground plane angle was found to result in a performance degradation across the entire range of values tested.

2. The creation of a semi-empirical model was found to account for the effects of both ground plane angle and blade loading coefficient. The coefficients of the model were plotted against each other and differences between ground plane angle were easily distinguishable. Future work may be done to refine the model and provide a closed-form power ratio solution which includes effects of both ground plane angle and blade loading coefficient.

3. Performance penalties of 7% were seen for sloped terrain as compared to level terrain. For larger ground plane angles, these penalties were highest at lower hub heights. In contrast, for smaller ground plane angles, these performance penalties were highest at higher hub heights.

4. Performance penalties of 2% above hover out-of-ground-effect were seen when hovering over sloped terrain. These performance penalties were seen for ground plane angles of 6, 12, 15, and 18 deg and were seen at hub heights above $z/R = 1.7$. Blade loading coefficient

did not appear to have a significant impact on the regions which experienced performance penalties above hover out-of-ground-effect.

5. Rotor performance was found to be sensitive to changes in ground plane angle at lower hub heights. Hub heights from $z/R = 0.6$–1.0 could see anywhere from a 1% to 7% performance penalty when hovering over sloped terrain as compared to level terrain, while $z/R = 1.4$–2.0 would only see performance penalties from 2% to 4% when sloped terrain performance was compared to level.
6. Profile power was found to be sensitive to the value of ground plane angle. When operating at $z/R = 2.0$, hover over ground plane angles of 12–18 deg was found to require 2% less power at a collective blade pitch of 0 deg than for hover over lower ground plane angles.
7. When examining plots of power ratio versus z/R, non-standard performance effects were seen at a $z/R = 1.2$–1.4. This behavior has not been noted in previous papers using the same rotor rig setup, so further investigation must be done to determine the cause of this finding.

4.3 Suggestions for Future Work

This investigation into hover performance over sloped terrain has provided new insight into the combined effects of ground plane angle and blade loading coefficient on in-ground-effect hover performance. However, there are still several areas for further investigation in order to obtain a better understanding on how sloped terrain affects hover performance.

Performance penalties as compared to HOGE were noted up at higher hub heights from

z/R of 1.7–2.0. The use of a larger hub height sweep range from $z/R = 0.6$ to OGE would allow for analysis on how the ground effect benefit changes at higher hub heights, as it is currently not known at what hub height ground plane angle ceases to have an effect on hover performance.

The present study used an isolated rotor with the same rotor blade geometry as the blades used on the OH-58C. While similarities will hopefully be seen between the current laboratory and future flight testing results, laboratory testing could answer scalability questions between lab and flight testing by fitting a scaled OH-58C fuselage under the isolated rotor system. Such a change would hopefully provide similar flow field and performance results between the laboratory and flight testing. Additionally, the results with the fuselage would be compared to the results from the isolated rotor to see if any non-monotonic or unintuitive behavior appears with the additions of the fuselage.

A single rotor blade geometry with rectangular, untwisted blades was used for the experiment. This simplified blade design is seldom used for modern helicopters, which often include multiple airfoil sections and complex planform geometry. Further testing would investigate the effects that solidity, taper, twist, and blade number have on hover performance over sloped terrain, similar to the work done by Gilad [38]. Certain rotor blade geometry may be more or less sensitive to changes in θ_{g}, and this work would help to better understand how modern helicopter performance would be influenced by sloped terrain.

Finally, future work could investigate the fundamental physical mechanisms which influenced the present hover performance results. Research on rotor inflow distribution and wake contraction for various ground plane angles may shed light on the performance penalties observed when hovering over sloped terrain. Previous research by Milluzzo et al. [27] observed a greater expansion of the wake on the downhill side of the inclined ground plane as compared to the uphill side, suggesting a reduction in performance due to the increased inflow and reduced angle of attack on the downhill side. They also observed formation of two wall-jet features on the uphill side, which resulted in changes in recirculation regions near the hub. Because these results were for a single hub height and a single plane that was aligned in the direction of the incline, they could not provide insight into the three-dimensionality and sensitivities of the problem. Future flow field measurements may yield insight into how these flow mechanisms are affected by ground inclination and how they affect rotor performance, and they may also help explain the performance effects seen at $z/R =$ 1.2–1.4.

Chapter A: Appendix A

A.1 Power Polars

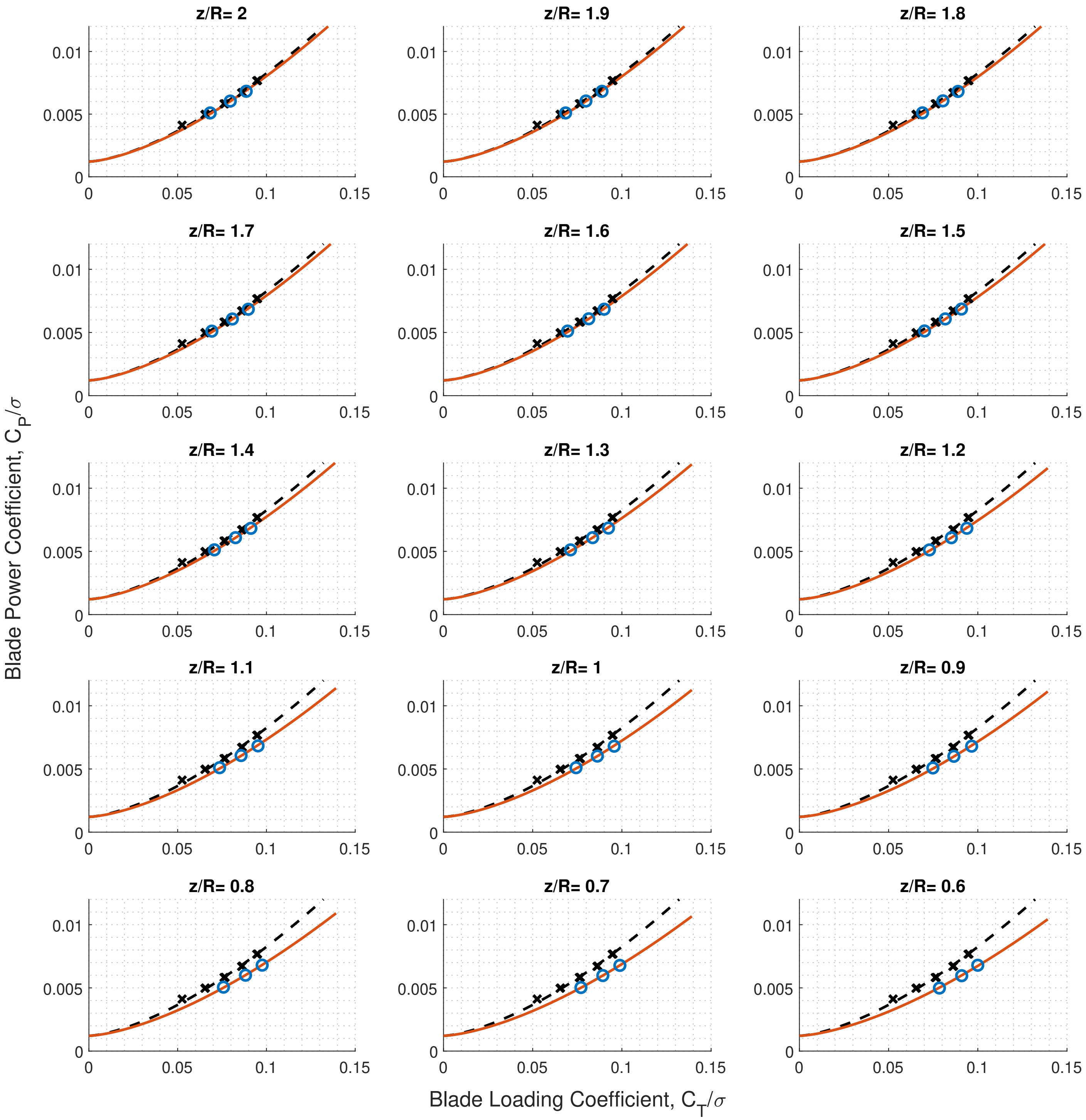

Figure A.1: Power polars for $z/R = 0.6 - -2.0$ and $\theta_g = 0°$.

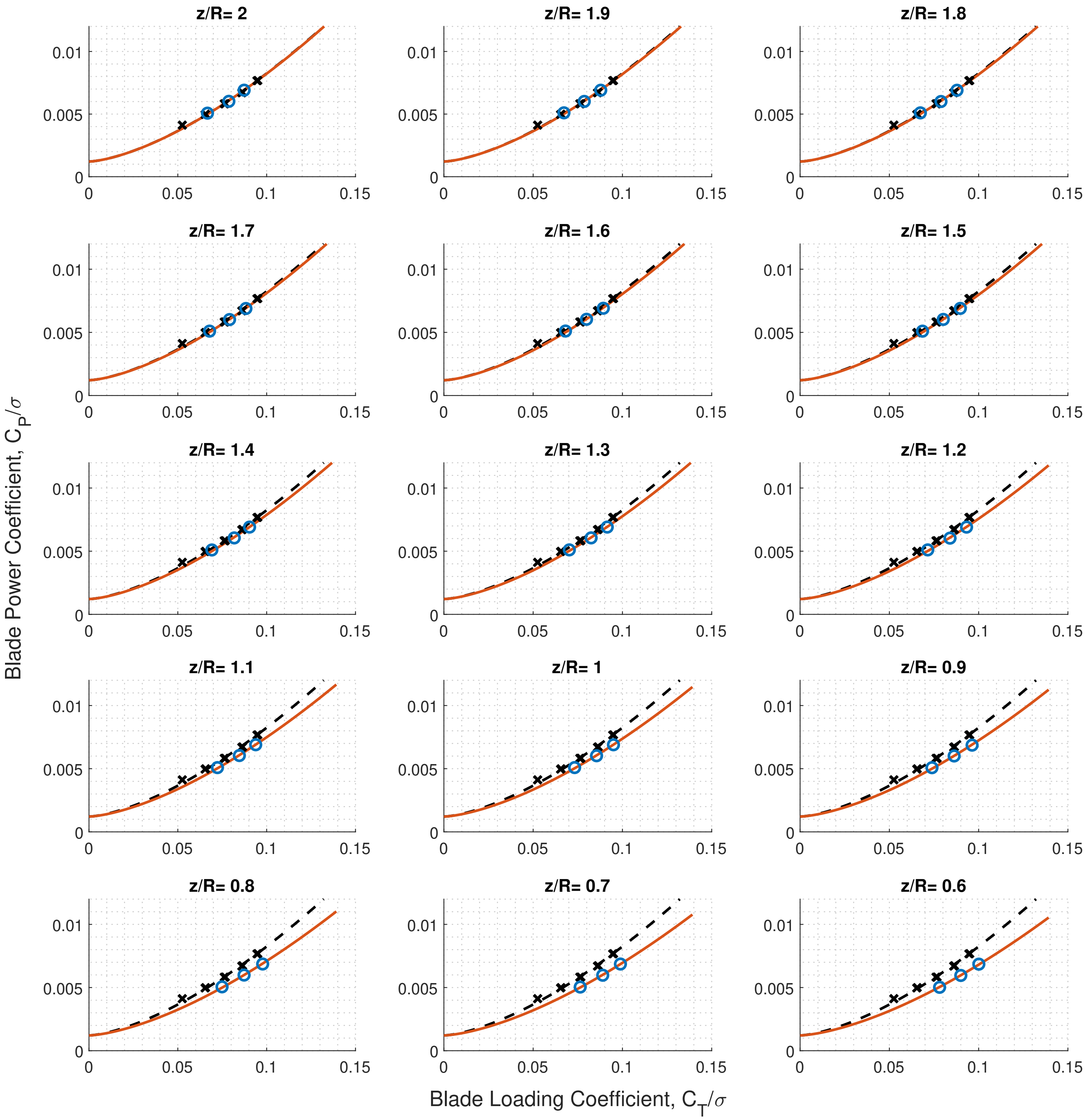

Figure A.2: Power polars for $z/R = 0.6 - -2.0$ and $\theta_g = 3^\circ$.

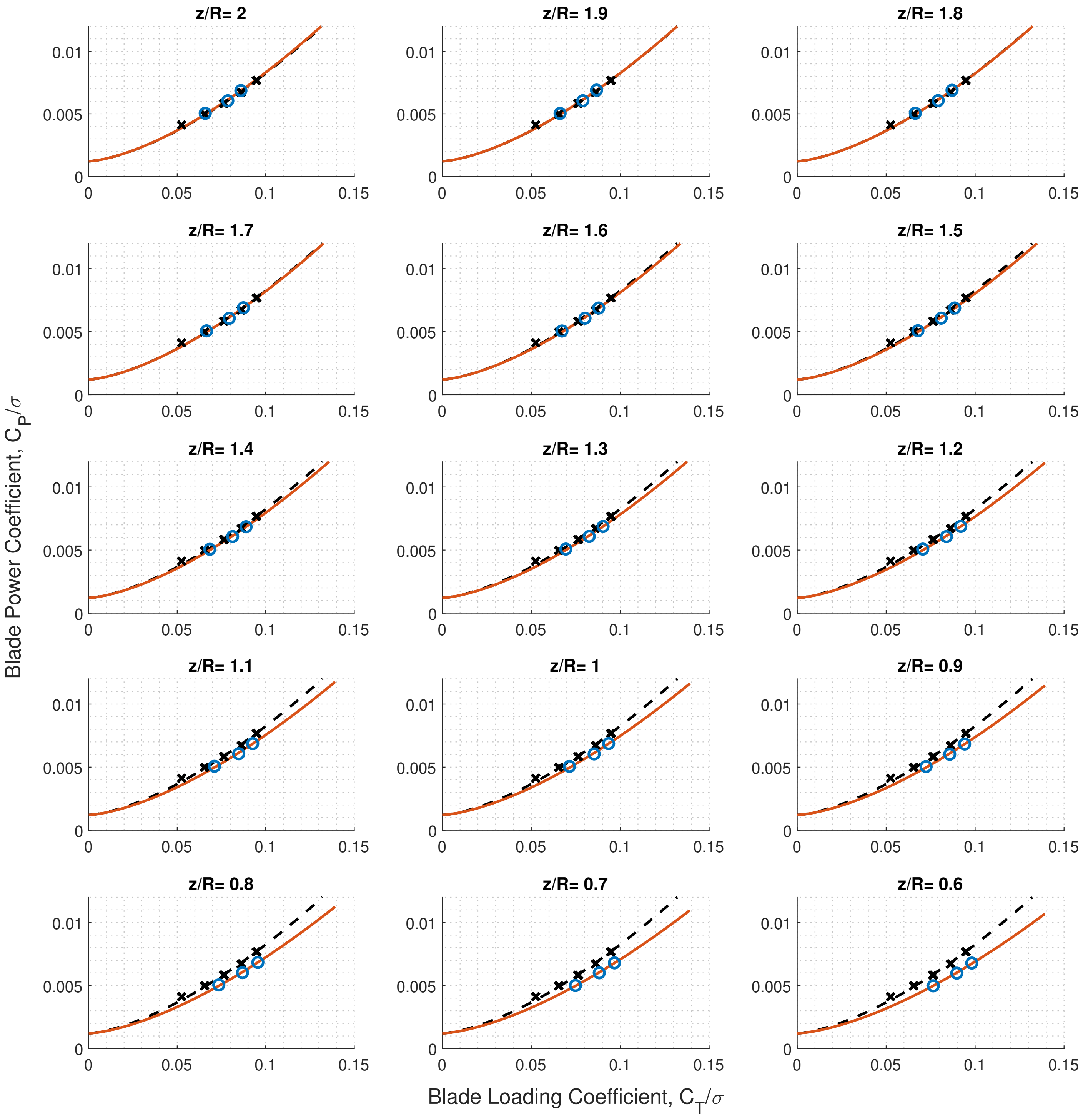

Figure A.3: Power polars for $z/R = 0.6 - -2.0$ and $\theta_g = 6°$.

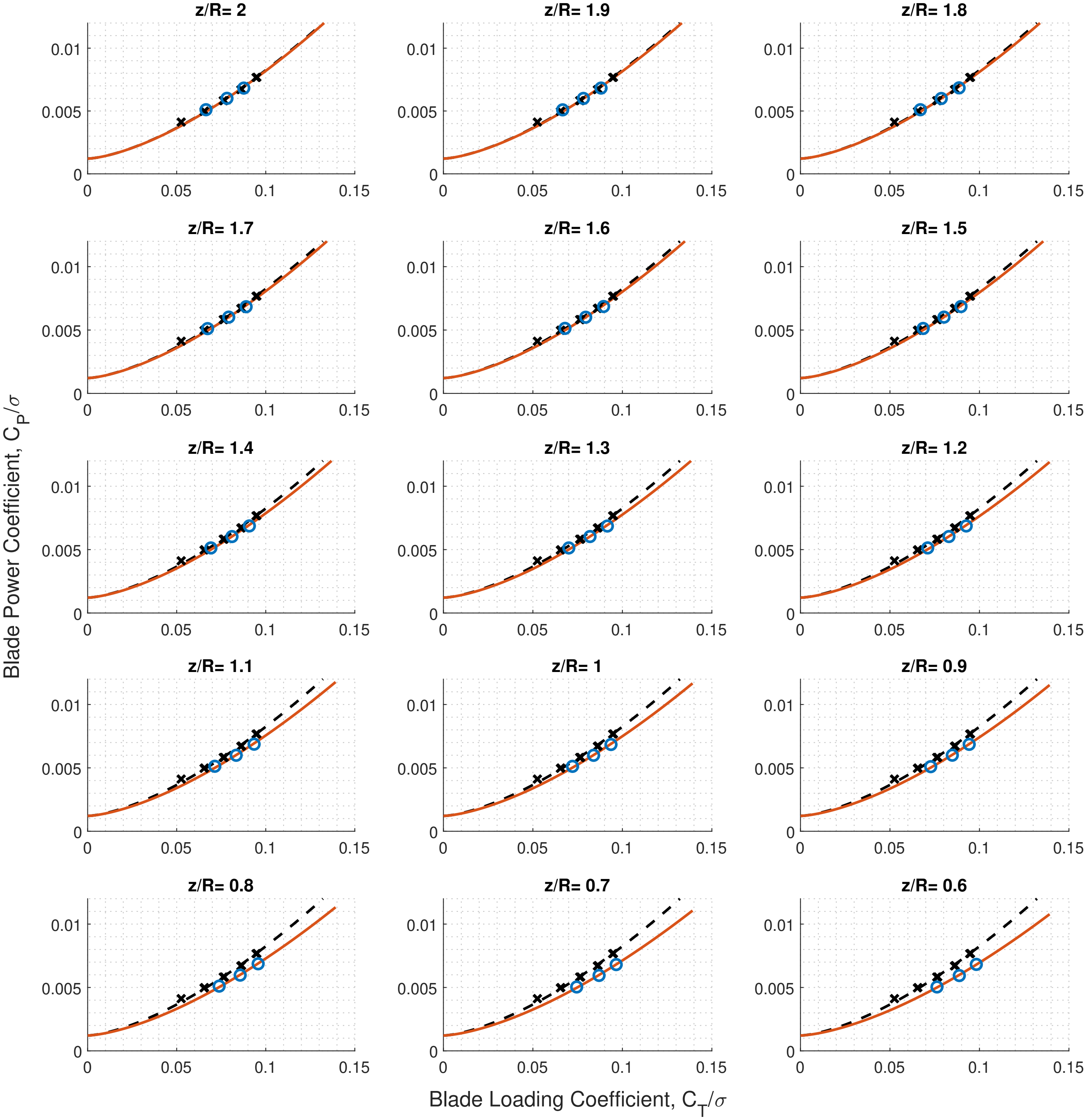

Figure A.4: Power polars for $z/R = 0.6 - -2.0$ and $\theta_g = 9^\circ$.

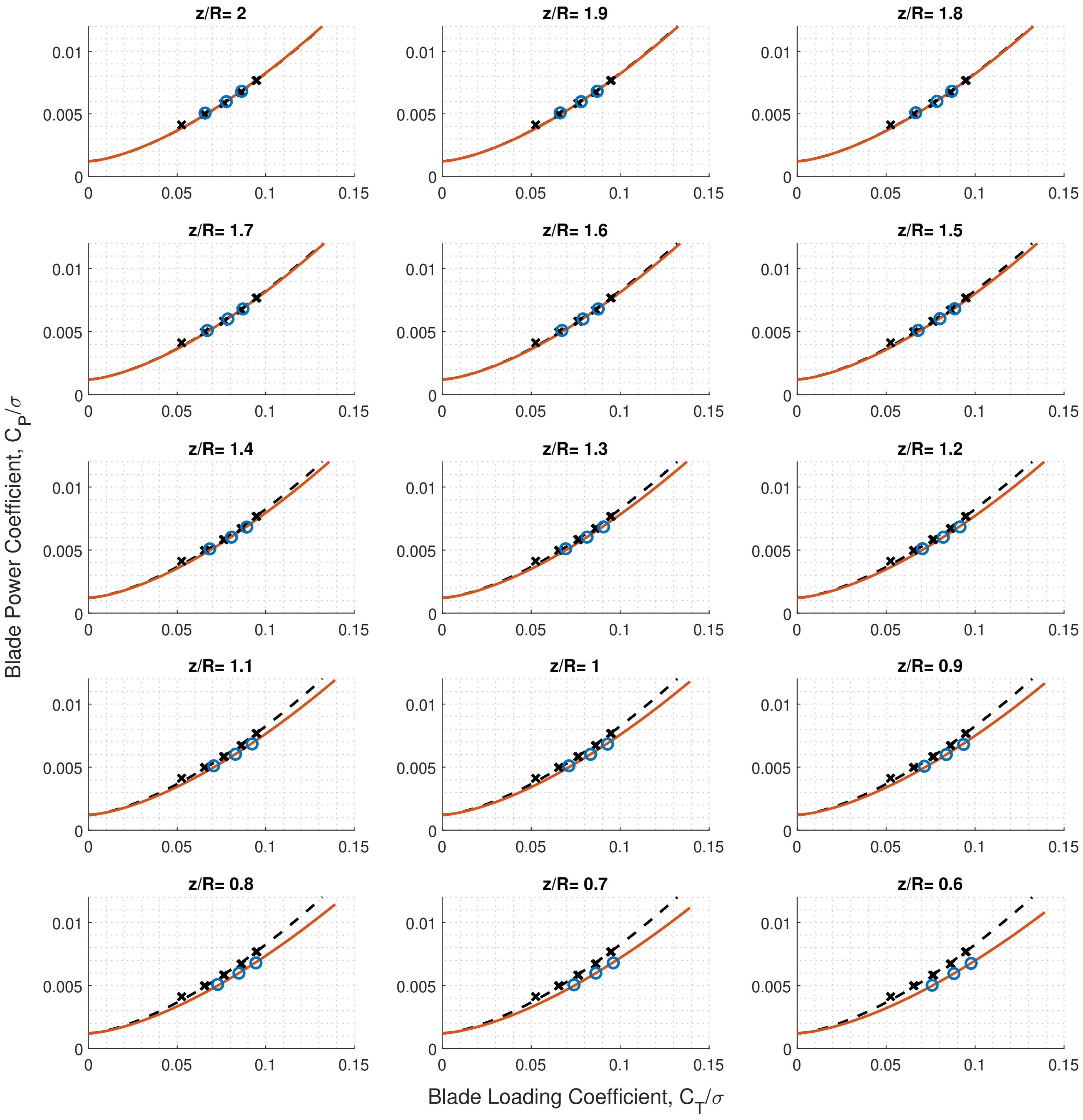

Figure A.5: Power polars for $z/R = 0.6 - -2.0$ and $\theta_g = 12°$.

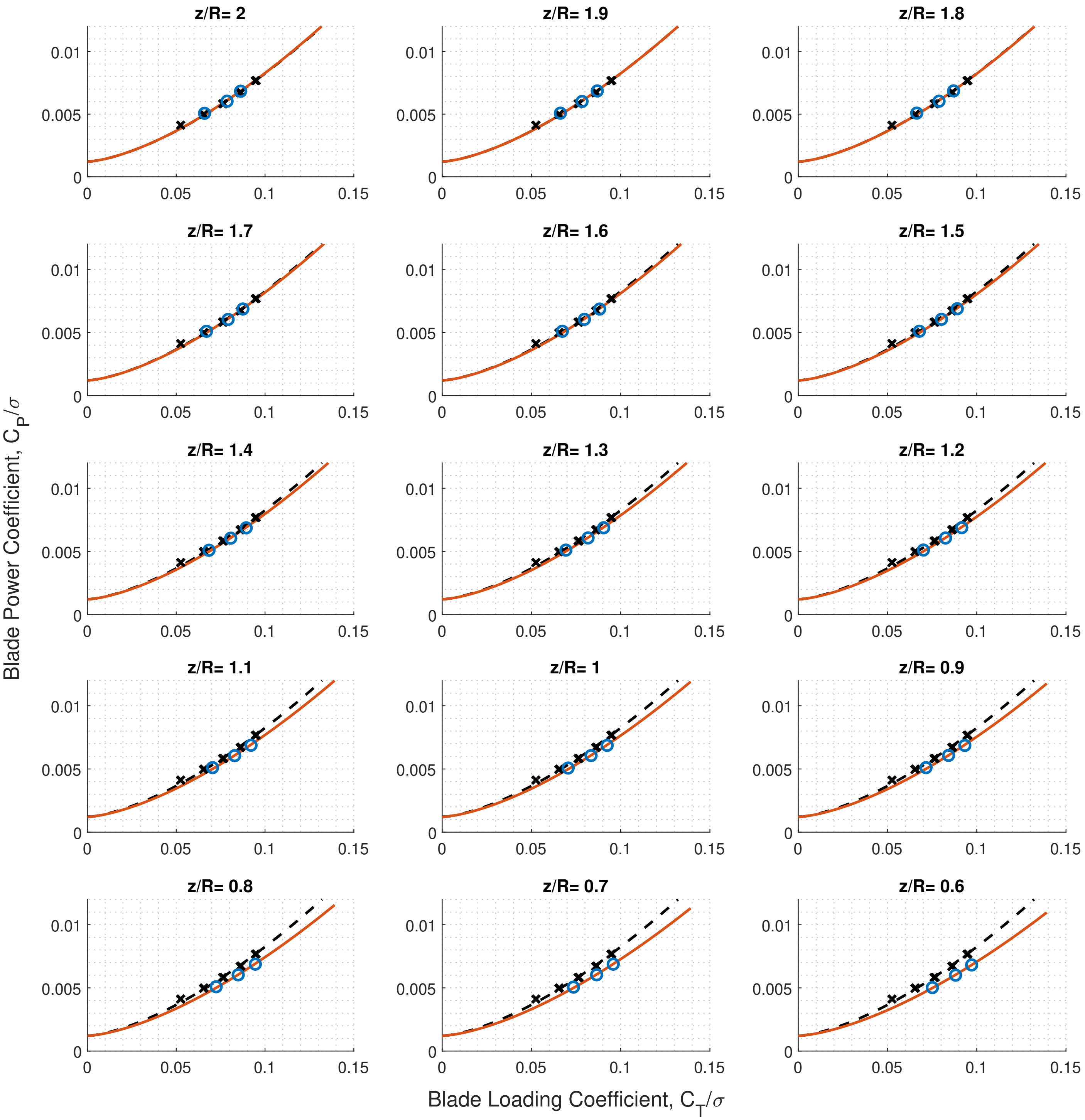

Figure A.6: Power polars for $z/R = 0.6 - -2.0$ and $\theta_g = 15°$.

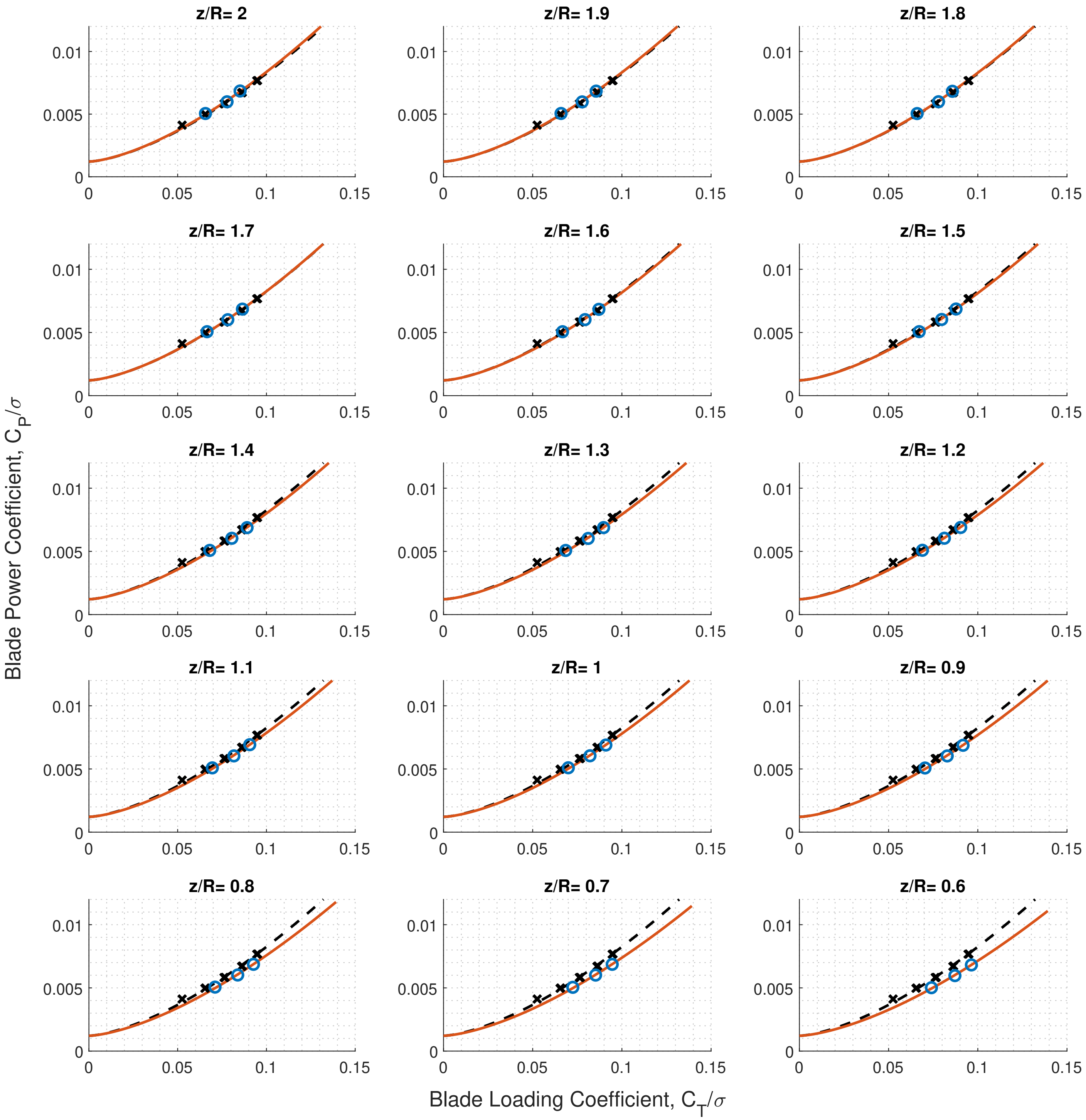

Figure A.7: Power polars for $z/R = 0.6 - -2.0$ and $\theta_g = 18°$.

Bibliography

[1] J. G. Leishman. *Principles of Helicopter Aerodynamics*. Cambridge University Press, New York, NY, 2 $^{\text{nd}}$ edition, 2006.

[2] I. C. Cheeseman and W. E. Bennett. The effect of the ground on a helicopter rotor in forward flight. *Aeronautical Research Council R&M No. 3021*, 1955.

[3] J. S. Hayden. The Effect of the Ground on Helicopter Hovering Power Required. In American Helicopter Society International 32nd Annual Forum Proceedings, Washington, DC, May, 1976.

[4] J. Zbrozek. Ground effect on the lifting rotor. *Aeronautical Research Council R&M No. 2347*, 1947.

[5] A. Betz. The ground effect on lifting propellers. Technical report, National Advisory Committee for Aeronautics, 1937.

[6] E. A. Fradenburgh. The helicopter and the ground effect machine. *Journal of the American Helicopter Society*, 5(4):24–33, October 1960.

[7] H. G. Küssner. Helicopter problems. Technical report, National Advisory Committee for Aeronautics, 1937.

[8] M. Knight and R. A. Hefner. Analysis of Ground Effect on the Lifting Airscrew. Technical Note TN 835, NASA, 1941.

[9] Federal Aviation Administration. *Helicopter Flying Handbook*. United States Department of Transportation, faa-h-8083-21b edition, 2019.

[10] R. W. Prouty. Ground Effect and the Helicopter: A Summary. In AIAA/AHS/ASEE Aircraft Design Systems and Operations Meeting, Colorado Springs, CO, October 14–16, 1985. AIAA 85-4034.

[11] Robinson Helicopter. R44 Pilot's Operating Handbook. Manual, Robinson Helicopter, 1992.

[12] J. K. Tritschler, J. I. Milluzzo, and J. M. Holder. Performance Effects of Hover In-Ground-Effect over Sloped Terrain. In American Helicopter Society International 75th Annual Forum Proceedings, Philadelphia, PA, May 13–16, 2019.

[13] M. Knight and R.A. Hefner. Static thrust analysis of the lifting airscrew. Technical report, National Advisory Committee for Aeronautics, 1937.

[14] R. B. Lewis. Army helicopter performance trends. *Journal of the American Helicopter Society*, 17(2):15–23, April 1972.

[15] H. Y. Law. Two Methods of Prediction of Hovering Performance. Technical Report TR 72-4, USAAVSCOM, 1972.

[16] D. Zagaglia, M. Giuni, and R. B. Green. Rotor-Obstacle Aerodynamic Interaction in Hovering Flight: An Experimental Survey. In American Helicopter Society International 72nd Annual Forum Proceedings, West Palm Beach, FL, May 17–19, 2016.

[17] D. Zagaglia, G. Gibertini, M. Giuni, and R. B. Green. Experiments on the Helicopter-Obstacle Aerodynamic Interference in Absence of External Wind. In 42nd European Rotorcraft Forum Proceedings, Lille, France, September 6–8, 2016.

[18] G. Gibertini, C. Clavel, D. Grassi, C. Parolini, D. Zagaglia, and A. Zanotti. An Experimental Set Up for the Study of Helicopter and Building Aerodynamic Interaction. In 40th European Rotorcraft Forum Proceedings, Southampton, UK, September 2–5, 2014.

[19] G. Gibertini, D. Grassi, C. Parolini, D. Zagaglia, and A. Zanotti. Experimental investigation on the aerodynamic interaction between a helicopter and ground obstacles. *Proceedings of the Institution of Mechanical Engineers, Part G: Journal of Aerospace Engineering*, 229(8):1395–1406, 2015.

[20] G. Gibertini, G. Droandi, D. Zagaglia, P. Antoniazza, and A. O. Catelan. CFD Assessment of the Helicopter and Ground Obstacles Aerodynamic Interference. In 42nd European Rotorcraft Forum Proceedings, Lille, France, September 6–8, 2016.

[21] D. J. Pickles, R. B. Green, and M Giuni. Rotor wake interactions with an obstacle on the ground. *The Aeronautical Journal*, 122(1251):798–820, 2018.

[22] R. Boisard. Aerodynamic investigation of a helicopter rotor hovering in the vicinity of a building. In American Helicopter Society International 74th Annual Forum Proceedings, Phoenix, AZ, May 14–17, 2018.

[23] N. Iboshi, N. Itoga, J. V. R. Prasad, and L. N. Sankar. Ground effect of a rotor hovering above a confined area. *Frontiers in Aerospace Engineering*, 3(1):7–16, 2014.

[24] M. F. Konuş and Ö. Savaş. Rotor vortex wake in close proximity of walls in hover. *Journal of the American Helicopter Society*, 61(4):1–12, October 2016.

[25] A. Garofano-Soldado, G. Heredia, and A. Ollero. Aerodynamic interference in confined environments with tilted propellers: Wall effect and corner effect. In *2021 Aerial Robotic Systems Physically Interacting with the Environment (AIRPHARO)*, pages 1–8. IEEE, 2021.

[26] A. Garofano-Soldado, P. J. Sanchez-Cuevas, G. Heredia, and A. Ollero. Numerical-experimental evaluation and modelling of aerodynamic ground effect for small-scale tilted propellers at low reynolds numbers. *Aerospace Science and Technology*, 126:107625, 2022.

[27] Milluzzo, J., Martinez, A., Drayton, S., and Davids, S. Experimental Investigation of Rotors Hovering above Inclined Surfaces. *Journal of the American Helicopter Society*, 66(2):1–11, April 2021.

[28] G. Koçak. Flow characterization of full, partial, and inclined ground effect. Master's thesis, Middle East Technical University, 2016.

[29] J. M. Holder and J. K. Tritschler. Design and Conduct of a Flight Test to Investigate Hover In-Ground-Effect Performance over Sloped Terrain. In Vertical Flight Society International 75th Annual Forum Proceedings, Philadelphia, PA, May 13–16, 2019.

[30] W. S. Courtney. Landing a helicopter on a ship in rough seas is insanely difficult, 2016.

[31] Newsweek Staff. Raiding osama's compound, 2011.

[32] T. Demerly. Watch a ch-47 rescue a climber and 6 rescuers with impressive steep-slope pinnacle landing, 2018.

[33] D. Black, C. Schenk, J. Tritschler, J. Holder, and J. Milluzzo. Hover performance of an oh-58c in confined areas. In Vertical Flight Society International 79th Annual Forum Proceedings, West Palm Beach, FL, May 16–18, 2023.

[34] N. Itoga, T. Nagashima, Y. Yoshizawa, and J. V. R. Prasad. Numerical method for predicting i.g.e. hover performance of a lifting rotor. *Transactions of the Japan Society for Aeronautical and Space Sciences*, 43(141):122–129, 2000.

[35] J. Prewitt, J. Milluzzo, and J. Tritschler. Effects of sloped terrain on in-ground-effect hover performance for an isolated rotor. In Vertical Flight Society International 79th Annual Forum Proceedings, West Palm Beach, FL, May 16–18, 2023.

[36] E. Buckingham. On physically similar systems; illustrations of the use of dimensional equations. *Physical Review*, 4(4):345–376, 1914.

[37] I. H. Abbott and A. E. von Doenhoff. *Theory of Wing Sections*. Dover, New York, NY, 1959.

[38] M. Gilad. *Evaluation of Flexible Rotor Hover Performance in Extreme Ground Effect*. University of Maryland, College Park, 2011.